Development of a Fast X-ray Line Detector System for Two-Phase Flow Measurement

Kyle Song

Thesis submitted to the faculty of the Virginia Polytechnic Institute and State University
in partial fulfillment of the requirements for the degree of

Master of Science
In
Nuclear Engineering

Yang Liu
Mark Pierson
Heng Xiao

December 8th, 2016
Blacksburg, VA

Keywords: Attenuation Coefficient, Beam-hardening, Polychromatic Energy, Two-Phase Flow, Void Fraction, X-ray

Development of a Fast X-ray Line Detector System for Two-Phase Flow Measurement

Kyle Song

ACADEMIC ABSTRACT

Measuring void fraction distribution in two-phase flow has been a challenging task for many decades because of its complex and fast-changing interfacial structure. In this study, a non-intrusive X-ray measurement system is developed and calibrated to mitigate this challenge. This approach has several advantages over the conventional methods such as the multi-sensor conductivity probe, wire-mesh sensor, impedance void meter, or direct optical imaging. The X-ray densitometry technique is non-intrusive, insensitive to flow regime changes, capable of measuring high temperature or high-pressure flows, and has reasonable penetration depth. With the advancement of detector technology, the system developed in this work can further achieve high spatial resolution (100 micron per pixel) and high temporal resolution (1000 frames per second). This work mainly focuses on the following aspects of the system development: establishing a geometrical model for the line detector system, conducting spectral analysis for X-ray attenuation in two-phase flow, and performing calibration tests. The geometrical model has considered the measurement plane, geometry of the test-section wall and flow channel, relative position of the X-ray source and detector pixels. By assuming axisymmetry, an algorithm has been developed to convert void fraction distribution along the detector pixels to the radial void profile in a circular pipe. The X-ray spectral analysis yielded a novel prediction model for non-chromatic X-rays and non-uniform structure materials such as the internal two-phase flow which contains gas, liquid and solid wall materials. A calibration experiment has been carried out to optimize the detector conversion factor for each detector pixels. Finally, the data measured by the developed X-ray system are compared with the double-sensor conductivity probe and gas flow meter for sample bubbly flow and slug flow conditions. The results show reasonable agreement between these different measuring techniques.

Development of a Fast X-ray Line Detector System for Two-Phase Flow Measurement

Kyle Song

GENERAL ADUIENCE ABSTRACT

Two-phase flow is a widely observed phenomenon in a nuclear reactor operation and thermal hydraulic applications during thermal energy transfer process. Hence, precise understanding of two-phase flow model is essential to a thermal hydraulic design and safe operation of nuclear reactor operation systems. However, two-phase flow analysis, via measuring void fraction distribution of a two-phase flow, has been a challenging task for many decades because of its complex and dynamical interfacial characteristics. In this study, a non-intrusive X-ray measuring technique is developed to mitigate some of the conventional challenges of void fraction measurement of a two-phase flow. The void fraction imagery via X-ray densitometry technique is insensitive to flow regime changes at high temperature or high pressure flows conditions with reasonable penetration depth capabilities. Together, with the advanced detector technology and spectral analysis of the X-ray attenuation in two-phase flow, this study delivers both qualitative and quantitative geometrical model for the line detector system to provide a radial void profile of a circular pipe. Moreover, the X-ray spectral analysis yielded a novel prediction model of a non-chromatic X-rays and non-uniform structure materials such as the internal two-phase flow which contains gas, liquid, and solid pipe materials. A calibration experiment has been carried out to optimize the detector conversion factor for each detector pixels. Finally, the data measured by the developed X-ray system are compared with the double-sensor conductivity probe and gas flow meter for sample bubbly flow and slug flow conditions. The results show reasonable agreement between these different measuring techniques.

TABLE OF CONTENTS

LIST OF FIGURES

LIST OF TABLES

NOMENCLATURE

Symbol	Description
I_o	Unaltered original incident intensity of X-ray photon,
I_x	Intensity of the radiation which transmitted through the absorber,
x	Overall penetrated depth of absorber material,
$I_{2ø}$	X-ray beam intensity transmitted through two-phase mixture,
$l_{2ø}$	Overall transmitted depth of two-phase mixture,
m	Mass fraction of given phase compound k,
E_{pixel}	Total number of electron,
V_{pixel}	Voltage output displayed by each pixel [V],
A_{pixel}	Effective area of detector pixel [mm^2],
mA	Operating current [mA],
I	Number of X-ray photons per energy level [#photons/keV·mm^2 ·mA·sec],
f_{conv}	Detector conversion factor [# electrons/X-ray photon],
e	Primary photon energy [keV],
C_f	Charge amplifier capacitance [F],
Q_{pixel}	Measured in coulomb unit,
$V_{pixel\text{-}2ø}$	Voltage output for two-phase mixture,
$V_{pixel\text{-}fo}$	Voltage output for the test section with full of fluid (water) that is measured at void fraction of α=0,
$V_{pixel\text{-}go}$	Voltage output for the test section with full of gas (air) that is measured at void fraction of α=1,
a	Major semi-principal axes of an ellipse,

b	Minor semi-principal axes of an ellipse,
h	x-coordinates of the center of an ellipse,
k	y-coordinates of the center of an ellipse,
x_o	X-ray source location in x,
y_o	X-ray source location in y,
$\theta_{beam\ max}$	Maximum X-ray beam angle,
x_{domain}	Possible ranges for the pipe center location,
y_{domain}	Possible ranges for the pipe center location,
r_{pipe}	Outer radius of pipe,
$A_{nth\ pixel}$	Flow area measured by X-ray line beam at each n_{th} detector pixel,
$A_{secotor}$	Area of partitioned sector (area between ring #n and ring # n+1 in the $A_{nth\ pixel}$),
R	Radius of the n_{th} partitioned ring,
A_{sector}	Area of partitioned sector,
$A_{nth\ pixel}$	Area measured by X-ray line beam at n_{th} pixel,
$x(\tau)$	Upstream signal (center detector arrangement-6'' detector),
$y(t-\tau)$	Downstream signal (top detector arrangement-4'' detector) with time delay τ,
T	Integration time,
n	Peak position of the signal,
N_s	Total number of sample,
f	Sampling frequency,
A_{coeff}	2^{nd} degree coefficient term,
B_{coeff}	1^{st} degree coefficient term,
C_{coeff}	Constant term,
C_{max}	Primary peak height,

C_2	Height of the secondary peak,
μ	Attenuation coefficient,
$\mu_{2\emptyset}$	Attenuation coefficient of two-phase mixture,
μ_p	Attenuation coefficient of test section,
δ_{wall}	Test section thickness,
α	Volume fraction of gas,
Δt	Exposure time (sampling time in second) [sec],
Δx	Distance form source to detector center location in x-direction,
Δy_{nth}	Location of n_{th} detector pixel in y-direction from detector center location,
α_{Radial}	Radial void fraction (at n_{th} partitioned ring),
$\alpha_{nth\ pixel}$	Measured time and line averaged void fraction information at n_{th} pixel,
τ	Time delay,
Δz	Distance between two detector arrangement [m],
τ^*	Transit time [sec],

Acronyms:

1D	One dimensional,
2D	Two dimensional,
3D	Three dimensional,
CMOS	Complementary metal-oxide semiconductor,
CT	Computed tomography,
GOS	Gadolinium oxysulfide,
GUI	Graphical user interface,
LOCA	Loss-of-coolant accident,

SOD	Source to object distance,
ODD	Object to detector distance,
SPD	Source to detector pixel distance,
PPR	Primary peak ratio,
XRF	X-ray fluorescence,

1. INTRODUCTION

1.1 Purpose and Motivation of Research

Nuclear reactors typically use water as a coolant to transfer thermal energy released by a nuclear fission process to maintain safe operating temperature. In the nuclear coolant system, boiling may occur inside the reactor core during normal operation or accident transients when a heated fuel surface exceeds the saturation temperature of the surrounding coolant. As a result, heat transfer and phase change take places, that is, bubbles are formed on the heated fuel surface and transported by the bulk fluid – a two-phase flow phenomenon exists [1]. Two-phase flow can also exist in other parts of a reactor system such as pressurizer, steam generators, and various piping elements. Since the two-phase flow is widely encountered in nuclear reactor operation and thermal hydraulic applications [2,3], precise measurement of void fraction is of great importance in developing a robust two-phase flow model that is essential to the thermal hydraulic design and safe analysis of nuclear reactors.

1.1.1 Two-Phase Flow Fundamentals

A gas-liquid two-phase flow is characterized by void fraction, flow orientation, and flow component and phase properties. In particular, the void fraction, which is the ratio of the gas-phase volume to the entire flow volume, has a direct impact on the two-phase flow structure [2]. The two-phase flow phase can be categorized into five flow regimes: bubbly, cap-bubbly, slug, churn-turbulent, and annular flow based on different levels void fractions. Different flow regimes of air-water two-phase flows in a vertical rectangular channel are shown in Figure 1-1.

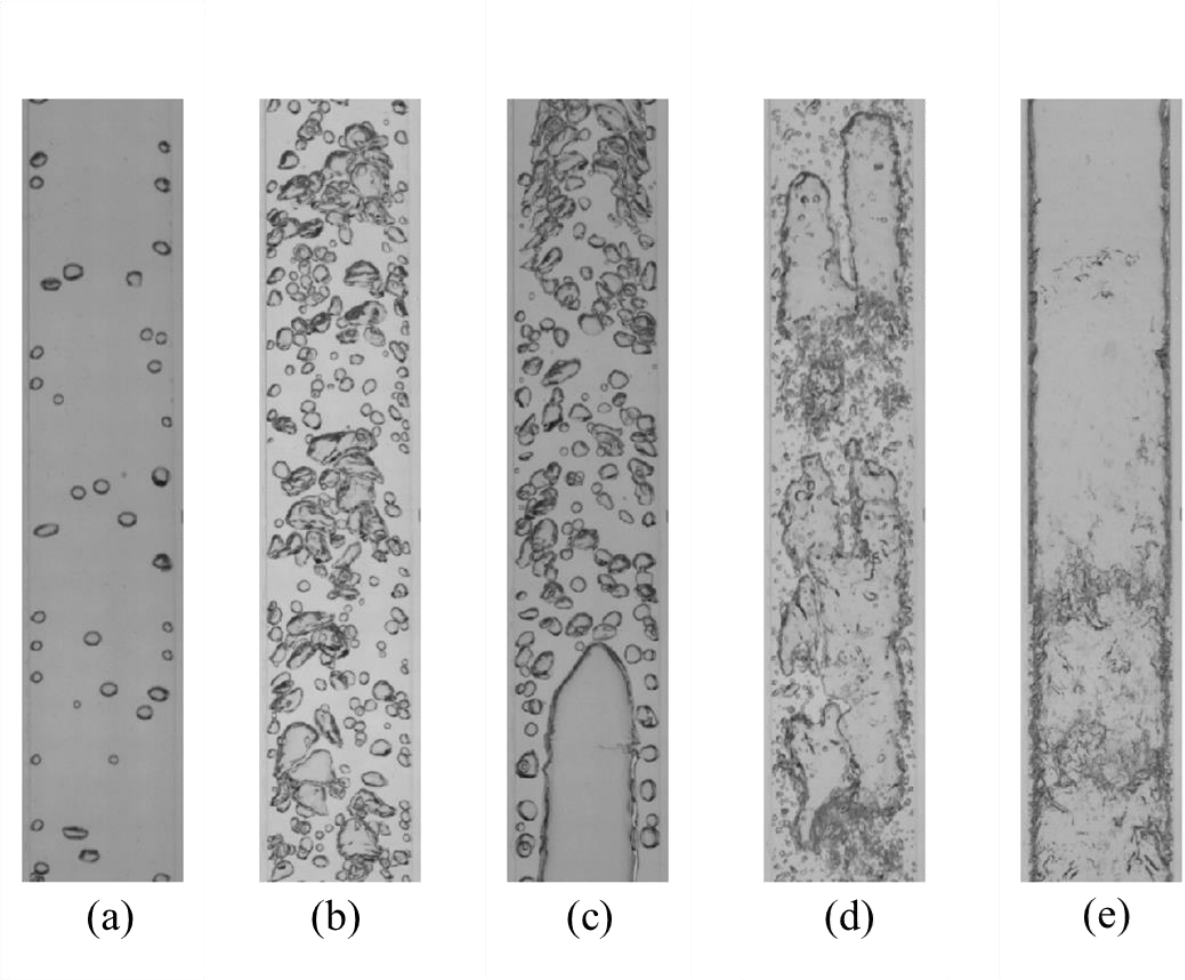

Figure 1-1: Different flow regimes in a vertical rectangular channel. Bubbly flow (a), cap-bubbly flow (b), slug flow (c), churn-turbulent flow (d), and annual flow (d).

In the bubbly flow regime (refer to Figure 1-1(a)), the bubbles are well-dispersed and the shape and size of the bubbles are relatively uniform with a typical void fraction of less than 15%. As the void fraction increases (more bubbles are introduced into the flow field), the probability of bubble coalescence (bubble collision and aggregation) drastically increases to form larger bubbles in various shapes and sizes (near the cap region) that leads to complex bubble-bubble and bubble-liquid interactions in the flow field. Therefore, the flow characteristics will change dramatically according to the flow structure change. As the void fraction continues to increase (30% or above), bubble coalescences will occur more frequently and give rise to an elongated bullet shape bubble, which has a cross-sectional area close to that of the flow channel, called slug flow. As the void

fraction keeps increasing, the flow structure keeps evolving. These elongated slug bubbles may break up into churn bubbles due to the bubble surface instabilities and therefore, the flow regime transitions to churn-turbulent flow. Finally, the flow structure develops to annular flow, which has a gas core and wavy liquid film near the wall region.

1.1.2 Void Fraction Measurement Techniques

Measuring void fraction distribution in the two-phase flow has been a challenging task for many decades because of its complex and fast-changing interfacial structure. The liquid-air two-phase fluid dynamics are extremely complex, and to larger extent, they are still difficult to be characterize by modern-day fluid dynamic models. Then, it is not surprising that measurement of such an unpredictable flow stream is a challenging task even with all available mesurement techniques. Sone conventional method for the two-phase flow measurements are multi-sensor conductivity probe, wire-mesh sensor, impedance void meter, or direct optical imaging. Although conventional measurement systems are developed for analyzing the complexity of the two-phase flow, however, all conventional flow measurement techniques have their own limitations.

In this study, a non-intrusive X-ray measurement system is developed and calibrated to mitigate the void fraction measurement challenge. The radiation measurement approach has several advantages over the conventional methods. Some of the X-ray measurement benefits are: the measurement technique is non-intrusive, X-ray is insensitive to flow regime changes, capable of measuring high temperature or high-pressure flows, and radiation has a strong penetration depth.

Various radiation sources, wire-mesh sensor, probes, high-speed imaging techniques have been used by various researchers for analyzing the void fraction in two-phase flows and Table 1 gives a survey of researchers and the two-phase flow measurement sources. The primary objective of this study is utilize X-ray detection system to measure the void fraction distribution in the two-phase flow and compare the relative statistical error both analytically and experimentally between the X-ray detection system and conventional detection methods.

Table 1: Survey of the two-phase flow researchers and their measurement techniques

Two-Phase Flow Investigators	Type of Measurement	Energy of Radiation	X-ray beam	X-ray Image	Scan Rage
Manera (2009) [4]	Wire-Mesh Sensor, Probe	-	-	-	-
Barthel (2015) [3]	X-ray	150 keV	Cone-beam	2D Image reconstruction	1000-5000 Hz
Prasser (2005) [5]	X-ray, Wire-Mesh Sensor	160 keV	Cone-beam	Filter back-projection	Line detector 263 Hz
Kendoush (1996) [6]	X-ray, Non-intrusive Auto-Transformer	100 keV	Cone-beam	2D Image reconstruction	300 Hz
Mäkiharju (2013) [7]	X-ray, Probe, High-Speed Imaging	150 keV	Cone-beam	2D Image reconstruction	High-speed camera, image intensifier at 1000 Hz
Kendoush (1992) [8]	Gamma, Beta, Neutron, X-ray	3 MeV	Line-beam	Line Averaged	10^6 pulses/cm^2
Heindel (2011) [9]	X-ray	450 keV	Cone-beam	2D Image reconstruction	High-speed camera, image intensifier at 50 Hz
Stutz (2003) [10]	X-ray, Probe	160 keV	Cone-beam	2D Image reconstruction	Line Detector 5000 Hz
Hubers (2004) [11]	X-ray, Cellulose Fiber System	200 keV	CT-two cone beams	2D Image reconstruction	Camera, image intensifier at 10-60 Hz

1.2 X-ray Densitometry

For many years, X-ray imaging and computed tomography (CT) have been used in both medicine and industrial applications for two-phase flow measurements and also have shown a very good visualization of the internal structure of the flow field [7]. X-ray densitometry measurement technique has the advantage of being a non-intrusive measurement technique because an X-ray beam is not reliant on the phase distribution within the flow domain. For this reason, an X-ray has been employed by many scientists to analyze two-phase flow phenomena [8]. A recent study by Heindel (2011) provides a comprehensive review of the use of X-ray measurement system in two-phase flow [9], thus, improved technique development is expected by many research groups.

An X-ray attenuation technique has been widely used in two-phase flow measurement analysis [8,11,12], and presented here is a brief summary of the X-ray line detector system for the analysis of two-phase flow measurement. Generally, an X-ray line detector system measures the difference between the incident X-ray beam and fraction of an X-ray beam that is penetrating through two-phase which depends on the void fraction and the energy-dependent attenuation coefficient of each phase in the two-phase flow. From the X-ray intensity difference, the attenuated X-ray beam and known attenuation coefficients of each phase, one can then obtain a line averaged void fraction information. Lastly, current work also needs to address some important source of uncertainty and uncertainty effects related to employing an X-ray line detector system.

In the X-ray attenuation measurement of two-phase vertical flow experiment, X-ray source projected an incident beam at a circular test section that is 3 m in height, 3.81 cm in outer diameter, and 2.54 cm inner diameter to give overall projection area of 3.77 cm^2. The time-resolved measurements were on the order of 1000 frames per second with a total sampling time of 60 seconds. Note that in the experimental apparatus setup, each line average is detected by each pixel in the detector array. These individual readings of each detector pixel are combined to provide void fraction profile in the test section. This combined void fraction profile is then used to generate 2-D flow image. Furthermore, combined line averaged void fraction and velocity of two-phase mixtures are derived from system validation experiments to convert the pixel information to a radial void fraction and a radial velocity profile. Lastly, current study's

experimental setup also allowed to simulates different flow regimes such as bubbly, slug, and annular flow patterns.

1.3 Spectral Analysis

An X-ray beam is emitted when an anode metal is bombarded by high-speed electrons that are accelerated through high voltage potential difference. Just before the collision, an electron is decelerated near the target atoms due to the Coulombic force effect and the net loss of kinetic energy is emitted as an X-ray photon of equal energy [13]. If a bombarding electron has sufficient energy, it can eject an electron out of the inner shell of a target atom. In this case, an electron of a target atom from higher energy states will drop down to fill the lower energy orbital vacancy and emit an X-ray photon with characteristic energies determined by the net difference in the electron principle energy levels. Hence, an X-ray photon generated by an X-ray tube exhibits polychromatic characteristics, *i.e.*, X-rays have a wide range of energy levels [10-12].

When polychromatic X-ray beam penetrates through two-phase flow, X-ray photon energy undergoes absorption and scattering within the two-phase flow structure. During absorption or scattering process, lower-level photon energies are attenuated or scattered away, resulting in an altered photon energy of the X-ray emission spectrum. Such phenomenon is also referred to as beam hardening, a consequence of energy dependence of the two-phase flow structure attenuation coefficient and filtering lower level of the energy spectrum in order to increase the average photon energy level of polychromatic X-ray beam [13,16,17].

In this study, the non-energy-resolving (separable) detector was used – that is, the detector system is incapable of separating different energy levels of the polychromatic X-ray beam, and therefore, relies on the indirect measurement of total energy deposited by the polychromatic X-ray energy of detectable range [18]. Hence, a cautious observation must be made of the X-ray photon energy interaction within two-phase flow structure with energy-dependent attenuation coefficient properties of each phase at the effective photon energy level.

1.4 Detector System

In modern day complementary metal-oxide semiconductor (CMOS) detectors, scintillators are widely used in X-ray scanning application. For X-ray photon detection, a scintillator is attached to the surface of the CMOS detector array to convert X-ray photons into the visible light for detection by the photodiode array. The CMOS provides high–speed, high-bandwidth capabilities of X-ray signal acquisition. With technology improvement detector system developed in this study is capable of providing a high-spatial resolution (as little as 0.1mm in width per pixel) and high-temporal resolution at 1000 frames per second.

In typical non-energy-resolving X-ray detector, an X-ray photon beam is converted into voltage signal undergoing a three-stage transformation: conversion, transfer, and luminescence [19–21]. Gadolinium oxysulfide (GOS) is a scintillator material used in the conversion process that is known to have an overall efficiency around 15% [22]. However, the energy-dependent efficiency data is not available for the scintillator or the complementary metal–oxide–semiconductor (CMOS) detector that is used in this study. Therefore, a calibration experiment was performed to quantify the overall conversion involved in all three conversion processes and their dependence on photon energy. Furthermore, an X-ray photon to electron conversion factor (a novel detector-conversion method) was also proposed and developed in order to evaluate total energy detected.

One of the largest contributions from the X-ray spectral analysis is to investigate a void fraction differences between the true void fraction from the experiment data and quantitative measurement method that is used by many researchers in the two-phase flow research groups. Based on the calibrated data the spectral model is developed: the calibration/prediction model describing the void fraction in function of voltage response. Comparison between the quantitative void fraction model and the spectral model displayed a significant difference in the void fraction estimates. Many researchers have used polychromatic X-ray sources for two-phase flow measurement but studies lack comparison of the void fraction that is based on the X-ray energy spectrum versus quantitative method. Hence, the spectral model is used in order to obtain accuracy of time and line averaged void fraction measurement results.

2. ANALYTICAL MODELING

In this chapter, the current study discusses most significant and important fundamental characteristics of X-ray as a comprehensive basis for current study. In section 2.1, physical interaction between X-ray beam and the two-phase flow are discussed as this interaction characterizes the key mechanism that establishes the fundamental principle of attenuation of polychromatic X-ray energy beam due to its energy dependence of attenuation coefficient property of the two-phase of each phase. In this section, an overview of (i) general attenuation law, (ii) X-ray production, (iii) attenuation coefficient of known compound, (iv) X-ray emission spectrum, and (v) beam-hardening (filtration) are discussed. Also, the spectral model is developed based on polychromatic X-ray energy spectrum: voltage output represents the void fraction of the two-phase flow.

In section 2.2, geometric models for both X-ray line beam and circular test section are presented with a further discussion of implications involved in modeling a distorted cross-section of the circular test section and the X-ray line-beam in the measurement plane.

Finally, in section 2.3, development of conversion algorithm from pixel distribution to radial distribution is presented. Combined void fraction information from detector pixels does not represent radial void fraction profile data. Because pixel information only indicates the non-parallel forward projection of two-phase mixture, thus, a radial profile must be extracted from the combined pixel information.

2.1 Physical Principles of X-Radiation

X-radiation is a form of an electromagnetic radiation where X-ray above 5 kilo-electron-volt (keV) is considered to be a hard X-ray and frequently used in imaging applications [23]. Due

to its strong penetrating capability, X-ray applications are widely used to inspect internal structure of test object in both medicine (*i.e.* X-ray imaging, medical computed tomography or mammography) and industrial application (*i.e.* airport security system or electronics inspection for void and solder analysis) [24].

Despite its superb penetrating capabilities, the X-ray intensity nevertheless gets attenuated during the illuminating process. In fact, an X-ray intensity exponentially decreases as an X-ray photon beam is penetrating through a test object. As an X-ray penetrates through a test object, some portion of the X-ray photons are absorbed or scattered due to nature of test object's material composition – general law of attenuation effect, *i.e.,* the Beer-Lambert law. Also, X-ray quality and quantity factors that control photon interaction with atoms within test object will be discussed.

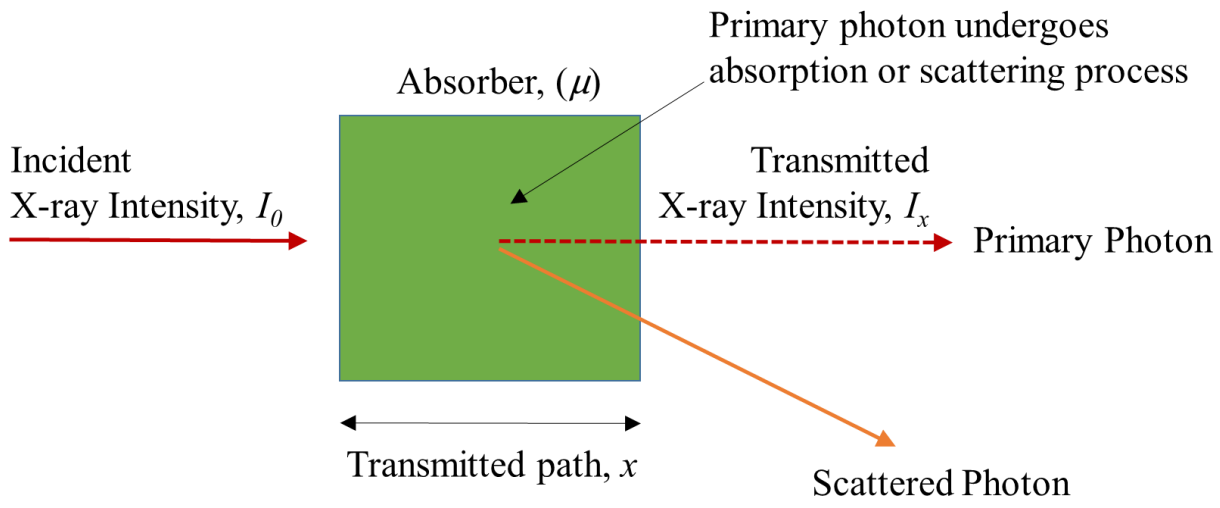

Figure 2-1: Schematic illustration of general attenuation process of X-ray intensity which strikes the absorber as the incident intensity, I_0, and the intensity of the radiation which gets through the absorber material with the attenuation coefficient, μ, as the transmitted intensity, I_x. Photon interaction mechanisms such as absorption and scattering process attenuate the state of incident photons. Photons that are transmitted are unaltered and denoted as primary radiation. Scattered radiation has a different direction of propagation and/or different energy.

2.1.1 X-ray Attenuation and Beer-Lambert Law

Suppose that incident X-ray has a single narrow and monochromatic line beam where the line beam is penetrating through a homogenous absorber material as shown in Figure 2-1. While the incident X-ray beam is penetrating through the absorber material, each individual primary photon has a certain of probabilty of colliding with absorber material's atoms [25]. When photons are undergoing interaction process within absorber material, one describes this photon as primary photons, this is not same as incident photon energy from the source. As each primary photons interacts with absorber material atom(s), such interaction process fundamentally changes the photon's energy state: magnitude of its energy, direction due to scattering, momentum, or degrade the photon entirely [13,26]. The interaction and eventual loss of primary photons result in attenuation of the X-ray beam. Now, the attenuation of the intensity of a single narrow monochromatic X-ray beam can be described by a general exponential attenuation model called Beer-Lambert law:

$$I_x = I_o \cdot e^{-\mu(Z,E_{x-ray})\cdot x} \tag{2.1}$$

where,

I_o is the unaltered original incident intensity of X-ray photon,

I_x is the intensity of the radiation which transmitted through the absorber,

$\mu(Z, E_{X\text{-}ray})$ is material and energy-dependent attenuation coefficient,

x is the overall penetrated depth of absorber material.

Therefore, one can expect to find that the transmitted intensity will be less than the incident intensity, that is,

$$I < I_o .$$

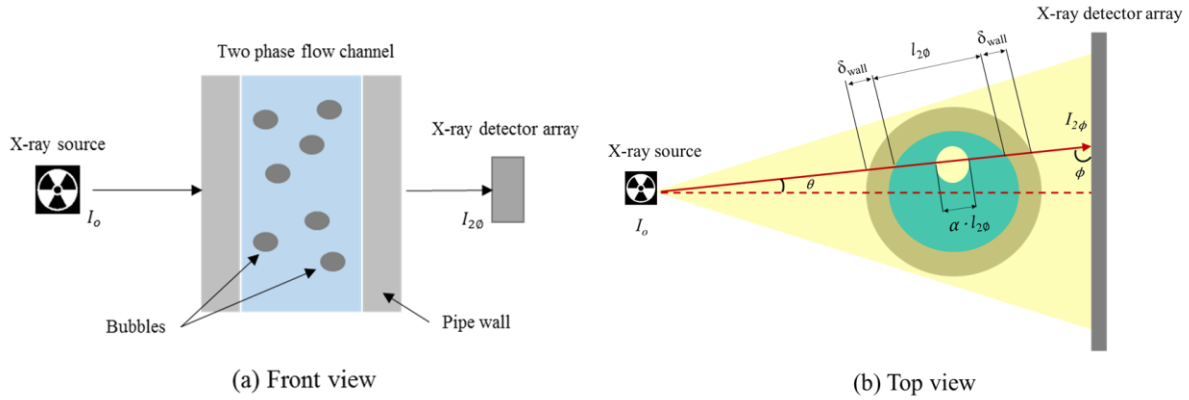

Figure 2-2: Front and crossional view of void fraction measurement arrangement using typical X-ray system. X-ray which strikes the two-phase mixture as the incident intensity, I_0, and the attenuated X-ray beam which gets through the flow structure as the transmitted intensity, $I_{2\phi}$.

Using Beer-Lambert law, one can estimate attenuated X-ray beam intensity after incident X-ray penetrates through a cross-section of a circular test section (refer to Figure 2-2). Figure 2.2 illustrates a typical experimental arrangement of the X-ray line detector system to measure a void fraction of the two-phase flow. The cone-shaped beam generated from the X-ray source penetrates through a circular cross-section of the circular pipeline. The attenuated X-ray photons are then detected by the detector array placed on the opposite side of the test section. From the Beer-lambert law, one can calculate the intensity of the X-ray beam after passing through the pipe wall and two-phase mixture of path distance, denoted as $l_{2\phi}$:

$$I_{2\phi} = I_o \cdot e^{-[l_{2\phi} \cdot \mu_{2\phi} + 2 \cdot \delta_{wall} \cdot \mu_p]} \tag{2.2}$$

where

I_o is the incident intensity of the X-ray beam source,

$I_{2\phi}$ is the X-ray beam intensity transmitted through two-phase mixture,

$\mu_{2\phi}$ is the attenuation coefficient of two-phase mixture,

μ_p is the attenuation coefficient of the test section,

$l_{2\phi}$ is the overall transmitted depth of two-phase mixture.

δ_{wall} is the test section thickness.

The attenuation coefficient of liquid is known, but the attenuation coefficient of the two-phase mixture is unknown. Thus, the attenuation coefficient of the two-phase must be written in terms of the void fraction and known attenuation coefficients for elementary compounds. For the two-phase mixture of *k*-phase components, the attenuation coefficient can be written as:

$$\frac{\mu_{2\phi}}{\rho_{2\phi}} = \sum_{k=1}^{K} m_k \frac{\mu_k}{\rho_k} \tag{2.3}$$

where,
m is the mass fraction of given phase compound k.

The density of the two-phase mixture is given by:

$$\rho_{2\phi} = \alpha \cdot \rho_g + (1-\alpha) \cdot \rho_f \tag{2.4}$$

where α is volume fraction of gas.

Therefore, relating the mass fraction at phase-k, m_k, one can obtain the following void fraction expression:

$$m_g = \frac{\alpha \cdot \rho_g}{\alpha \cdot \rho_g + (1-\alpha) \cdot \rho_f} \tag{2.5}$$

for the liquid-phase; and

$$m_f = \frac{\alpha \cdot \rho_f}{\alpha \cdot \rho_g + (1-\alpha) \cdot \rho_f} \tag{2.6}$$

for a two-phase of gas- and liquid-only phases.

Now, Eq. (2.3) becomes:

$$\frac{\mu_{2\phi}}{\rho_{2\phi}} = \frac{\alpha \cdot \rho_g}{\alpha \cdot \rho_g + (1-\alpha) \cdot \rho_f} \cdot \frac{\mu_g}{\rho_g} + \frac{\alpha \cdot \rho_f}{\alpha \cdot \rho_g + (1-\alpha) \cdot \rho_f} \cdot \frac{\mu_f}{\rho_f} \tag{2.7}$$

which is equivalent to:

$$\mu_{2\phi} = \alpha \cdot \mu_g + (1-\alpha) \cdot \mu_f \,. \tag{2.8}$$

Now, combining, Eq. (2.8) with equation Eq. (2.2), one can express $I_{2\phi}$ as following:

$$I_{2\phi} = I_o \cdot e^{-[\alpha \cdot l_{2\phi} \cdot \mu_g + (1-\alpha) \cdot l_{2\phi} \cdot \mu_f + 2 \cdot \delta_{wall} \cdot \mu_p]} \tag{2.9}$$

where,

I_o is the incident intensity of X-ray photon beam,

$I_{2\phi}$ is the X-ray intensity transmitted through overall two-phase mixture flow structure,

μ_f is the attenuation coefficient of liquid,

μ_g is the attenuation coefficient of gas,

δ_{wall} is the test section wall thickness,

$l_{2\phi}$ is the overall penetration depth of the two-phase flow.

2.1.2 Void Fraction of a Two-Phase Mixture

First, determine X-ray intensity of liquid-phase only in the flow channel. Hence, the fraction of X-ray photons that are not attenuated after passing through test section with liquid-phase only is given by:

$$I_f = I_o \cdot e^{-[l \cdot \mu_f + 2 \cdot \delta_{wall} \cdot \mu_p]} \tag{2.10}$$

where,

I_f is the X-ray intensity transmitted through overall liquid-phase only flow structure

l is the overall penetrate depth.

Recall from Eq. (2.9) void fraction of the two-phase mixture is given by:

$$I_{2\phi} = I_o \cdot e^{-[\alpha \cdot l_{2\phi} \cdot \mu_g + (1-\alpha) \cdot l_{2\phi} \cdot \mu_f + 2 \cdot \delta_{wall} \cdot \mu_p]} . \tag{2.11}$$

Now, dividing equation, Eq. (2.10) by Eq. (2.11) yields:

$$\frac{I_f}{I_{2\phi}} = \frac{I_o \cdot e^{-[l \cdot \mu_f + 2 \cdot \delta_{wall} \cdot \mu_p]}}{I_o \cdot e^{-[\alpha \cdot l_{2\phi} \cdot \mu_g + (1-\alpha) \cdot l_{2\phi} \cdot \mu_f + 2 \cdot \delta_{wall} \cdot \mu_p]}} \tag{2.12}$$

The X-ray beam intensity at the origin, I_o, and acrylic wall attenuation effect is indifferent to both two-phase and liquid-phase only. Hence, these two terms are canceled out and yields:

$$\frac{I_f}{I_{2\phi}} = \frac{e^{-[l \cdot \mu_f + 2 \cdot \delta_{wall} \cdot \mu_p]}}{e^{-[\alpha \cdot l_{2\phi} \cdot \mu_g + (1-\alpha) \cdot l_{2\phi} \cdot \mu_f + 2 \cdot \delta_{wall} \cdot \mu_p]}} = e^{-[l \cdot \mu_f] + [\alpha \cdot l_{2\phi} \cdot \mu_g + (1-\alpha) \cdot l_{2\phi} \cdot \mu_f]} . \tag{2.13}$$

For the ease of identification, switch to using the initial only in the subscripts to identify the material phase. As the path length (domain thickness), l, remained unchanged. Simply write the ratio of beam intensities, attenuated by the liquid and two-phase. Hence, Eq. (2.13) to yield the following:

$$\frac{I_f}{I_{2\phi}} = e^{-l \cdot [\mu_f - \alpha \cdot \mu_g - (1-\alpha) \cdot \mu_f]} \tag{2.14}$$

Note, Eq. (2.14) can be transformed into:

$$\ln\left(\frac{I_{2\phi}}{I_f}\right) = l\cdot[\mu_f - \alpha\cdot\mu_g - (1-\alpha)\cdot\mu_f] = -l\cdot[\alpha(\mu_g - \mu_f)] \tag{2.15}$$

Similarly, repeat the same process from the equation, Eq. (2.10) with all gas-phase only in the flow channel, instead of liquid-phase-only. In doing so, one arrive at the following expression:

$$\ln\left(\frac{I_{2\phi}}{I_g}\right) = l\cdot[\mu_g - \alpha\cdot\mu_g - (1-\alpha)\cdot\mu_f] = -l\cdot[\alpha(\mu_g - \mu_f) - (\mu_g - \mu_f)]. \tag{2.16}$$

Note from Eq. (2.15), void fraction constructed can now be expressed as:

$$\alpha = -\frac{\ln(I_{2\phi}/I_f)}{l\cdot(\mu_g - \mu_f)} \tag{2.17}$$

and void fraction based on the equation, Eq. (2.16) is given by:

$$\alpha = -\frac{[\ln(I_{2\phi}/I_g) + l(\mu_g - \mu_f)]}{l(\mu_g - \mu_f)} = -\frac{\ln(I_{2\phi}/I_g)}{l\cdot(\mu_g - \mu_f)} + 1. \tag{2.18}$$

Now, equating equation Eq. (2.17) and Eq. (2.18), one can further eliminate attenuation coefficients and thus one can express void fraction as:

$$-\frac{\ln(I_{2\phi}/I_f)}{l\cdot(\mu_g - \mu_f)} = -\frac{\ln(I_{2\phi}/I_g)}{l\cdot(\mu_g - \mu_f)} + 1. \tag{2.19}$$

Multiplying both sides of Eq. (2.19) by $l\cdot(\mu_g - \mu_f)$ and rearrange the resulting expression yields attenuation coefficients expression as a function of intensity. That is:

$$-l(\mu_g - \mu_f) = \ln\left(\frac{I_{2\phi}}{I_f}\right) - \ln\left(\frac{I_{2\phi}}{I_g}\right) = \ln\left(\frac{I_g}{I_f}\right) \tag{2.20}$$

Now, substituting equation Eq. (2.20) in equation Eq. (2.17), yields a quantitative measure of void fraction given by:

$$\alpha = \frac{\ln(I_{2\phi}/I_f)}{\ln(I_g/I_f)}. \tag{2.21}$$

Note, one assumed a line-averaged void fraction along a single X-ray line beam with constant energy and/or constant attenuation coefficient.

Finally, equation, Eq. (2.21) provides void fraction measurement along any given X-ray beam as a function of the intensity of photon fluxes after passing through test section filled with the two-phase mixture, liquid-phase only, and gas-phase only. Note that X-ray source generated from X-ray tubes exhibit polychromatic characteristics (refer to Figure 2-3). Thus, a fraction of the X-ray photons which penetrates through the flow domain is a function of X-ray energy, where X-ray energy is defined by X-ray tube operating voltage.

The detector arrangement used in this research does not resolve the polychromatic energy spectrum. Instead, detector system only measures the total energy deposited in the detector pixels during the exposure period. Due to the polychromatic characteristics and non-energy-resolving detector system, Eq. (2.9) provides an estimation of the void fraction from the assumption that "monochromatic beam" must be substantiated under effective X-ray photon energy spectrum.

2.1.3 X-ray Production and Emission Spectrum

In general, X-ray photons are produced by bombarding an anode target metal with high-speed electrons accelerated by high voltage cathode [13]. When incident electrons are decelerated near the target atoms (Bremsstrahlung interaction), the loss of kinetic energy is emitted as photons of equal energy. In addition, the high-speed incident electrons with sufficient energy can eject an electron out of the innermost shell of a target atom [27,28]. As a consequence,

electrons from higher energy states drop down to fill the lower-energy vacancy and X-ray photons with characteristic energies determined by the electron energy levels [27,28]. This photoelectric effect of X-ray photons generation by an X-ray tube exhibit polychromatic characteristics, *i.e.*, the X-rays have a wide range of energies [10-12]. Refer to the Figure 2-3 for polychromatic X-ray emission spectrum with tungsten anode target with effective photon energy at 50keV. Note that in Figure 2.3, a peak energy occurred around 10keV. This peak characteristic photon emission is a result of K-shell ionization drop to L-shell. Refer to Table 2 for characteristic photon emissions from tungsten target material of K-shell and L-shell characteristic photons.

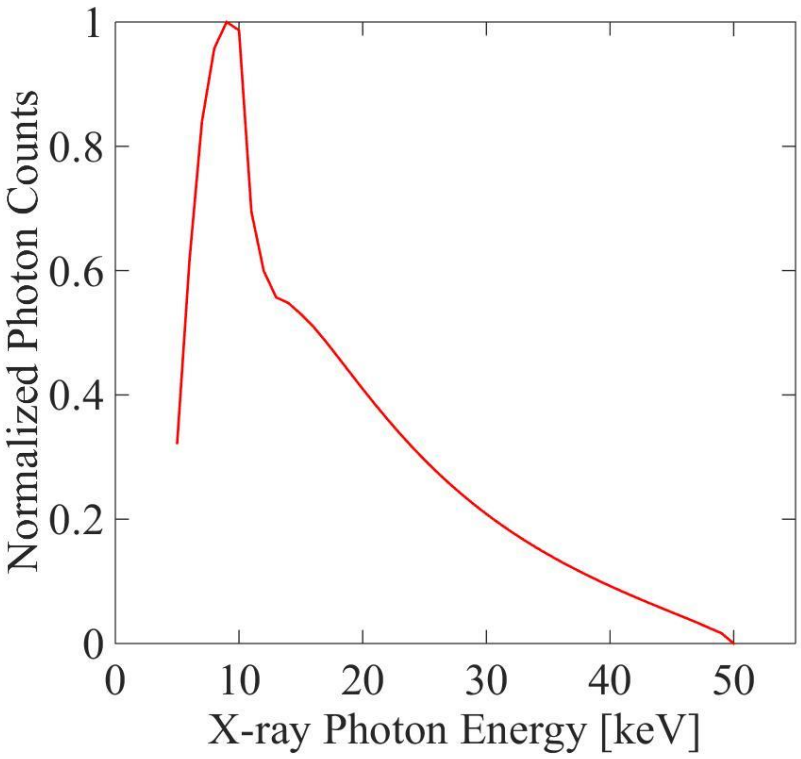

Figure 2-3**:** Polychromatic X-ray emission spectrum with tungsten anode target with effective photon energy at 50 *keV*. The graph illustrates the result of an exposure made with 127μm barium window shielding at a constant potential, producing 0.25 *mR/hr* at 5cm. X-ray spectrum generated using SpecCalc, a software developed by Poludniowski [29–31].

One needs to express X-ray beam in terms of both quantitative and qualitative factors. The X-ray quantitative refers to the number of X-ray photons in the projected beam that in turn determines the beam intensity [32]. The X-ray qualitative factors refer to the strength of X-ray beam penetrating ability; thus, higher the energy of X-ray's photon, higher its penetrating capacity through the transmitted target domain (i.e. two-phase mixture) [13,33]. Note that X-ray photon produced in the X-ray tube is controlled by four principal controlling factors: (i) operating current, (ii) operating voltage, (iii) filtration, and (iv) distance from the X-ray source to detector [13,34].

Two key factors that directly affect X-ray beam measurements are: operating current (*mAs)* and operating voltage (*kVp).* Note, here *mA* is a measurement unit of X-ray tube operating current and is defined as the amount of an electric charge flow per second where 1 coulomb is equivalent to $6.24 \cdot 10^{18}$ electron charges. Therefore, one can denote milliamperage-second (*mAs*) as a quantitative measurement to describe a number of electron production and exposure time, and hence a primary measurement of X-ray quantity. For example, if an X-ray operating panel is calibrated at 1*mA* and 1 second, this setting would be denoted as 1 *mAs*.

Operating voltage, kilovoltage (*kVp*), is a measurement unit that controls both quantitative and qualitative characteristics of the X-ray beam energy. The operating voltage, as measured in *kVp*, in turn, determines the kinetic energy of the electrons accelerated inside the X-ray tube and the peak energy of the X-ray emission spectrum that is proportional to the peak operating voltage [32]. As the kinetic energy of an electron in the X-ray tube increases the higher the likelihood of these electrons penetrating through the target domain (i.e. two-phase mixture) to reach the detector image pixel that is ultimately detected by the detector pixels (compared to lower energy beams that may be attenuated and/or scattered in two-phase flow. However, a note of caution here as some scattered X-ray radiation may also be detected at the detector pixel level, and it is shown that the higher the *kVp* of the beam, the greater the scatter X-ray will be produced [35,36]. Scatter X-ray is unwanted secondary radiation, and for reason, operating voltage, *kVp,* should be carefully controlled and monitored. Moreover, operation voltage should not be used as primary means to control the X-ray energy as increased photon density resulting from increased operating voltage (*kVp)* significantly beyond what is needed to penetrate two-phase mixture will inevitably increase the likelihood of adding unwanted energy response to detector pixel [13,35].

That being said, increasing the operating current (*mAs*) triggers more X-ray photons of the particular operating voltage (*kVp*), and in turn, produce photons of particular kinetic energy. This control mechanism is useful in working with two-phase mixture flow domain with deep penetration depth as a higher amount of photons that are sufficiently needed to actually reach the detector pixel are needed to provide more relevant information to further analysis.

Table 2: Principal Characteristic X-ray Energies for Tungsten

	Transition	Energy (keV)
K Series	N to K Shell	69.23
	M to K Shell	67.23
	L to K Shell	59.31
L Series	N to L Shell	11.28
	M to L Shell	9.62

Data from US Department of Health, Education, and Welfare. Radiological health handbook. Rev. ed. Washington, DC: US Government Printing Office, 1970 [37].

2.1.4 Attenuation Coefficient

In the equation, Eq. (2.1), I_o represents incident X-ray intensity at given energy level; and I is the intensity of the X-ray beam after penetrating through a homogeneous mixture with thickness x and μ, where μ is the energy and material density dependent attenuation coefficient. Since an attenuation coefficient is dependent on the density of a material and energy, the mass attenuation coefficient is often reported for convenience [38]. For example, attenuation for water vapor (gas) is much lower than its liquid or ice (solid) states because the gas molecules are more spread out in space than its liquid counterpart. Therefore, a probability of a photon interaction with a water particle vapor state is significantly less than water molecule in a liquid state. Here, one can normalize μ by dividing it by ρ, the density of the element or compound, to produce a value that will remain constant for a particular element or compound [39]. The resulting quotient, μ/ρ, is known as the mass attenuation coefficient and has units of cm^2/g. To convert a mass

attenuation coefficient, μ/ρ, to an attenuation coefficient, μ, simply multiply it by the density, ρ, of the material.

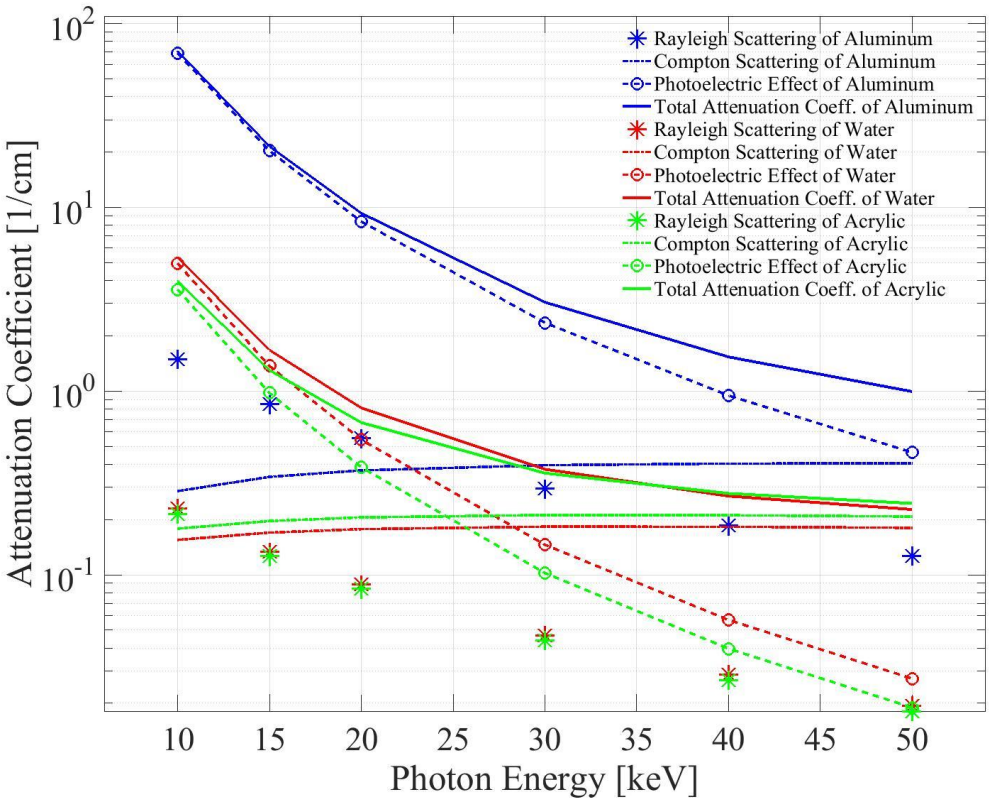

Figure 2-4**:** Total attenuation coefficients (solid lines) for aluminum, water, and acrylic. The contributions of principal photon-matter interactions are displayed as dashed curves for the Photoelectric effect (absorption) as dotted curves for the Compton (incoherent) scattering, and solid dotted point for the Rayleigh (coherent) scattering. Data from National Institute of Standards and Technology (NIST) [38,40].

One use of attenuation coefficient properties of known elements is to select the optimal X-ray spectra range of photon energy level that will provide the most desirable response with detector pixel's image element [20,41]. As an X-ray tube voltage increases, the total number of photons that are transmitted without any meaningful interaction within the two-phase mixture also

increases. Refer to the Figure 2-4. This graphical illustration explains the reduced probability of Photoelectric Effect and Compton Scattering with increased effective photon energy (keV). Note here, the percentage of photoelectric interactions decreases with increased photon energy, but the percentage of Compton interactions increases with increased kVp. As a result, as photon energy increases, there is an increased percentage of scatter and decreased the percentage of absorption of the attenuated X-ray beam [42]. For instance, it is important to detect the most probable primary X-ray photons when the X-ray beam is penetrating two-phase mixture including acrylic test section with a wall thickness of 1.27cm and overall water thickness of 2.54cm. With the data from Figure 2-4, one can determine most effective photon energy level for both water and acrylic (test section material), and thus, select an optimal X-ray tube operating voltage.

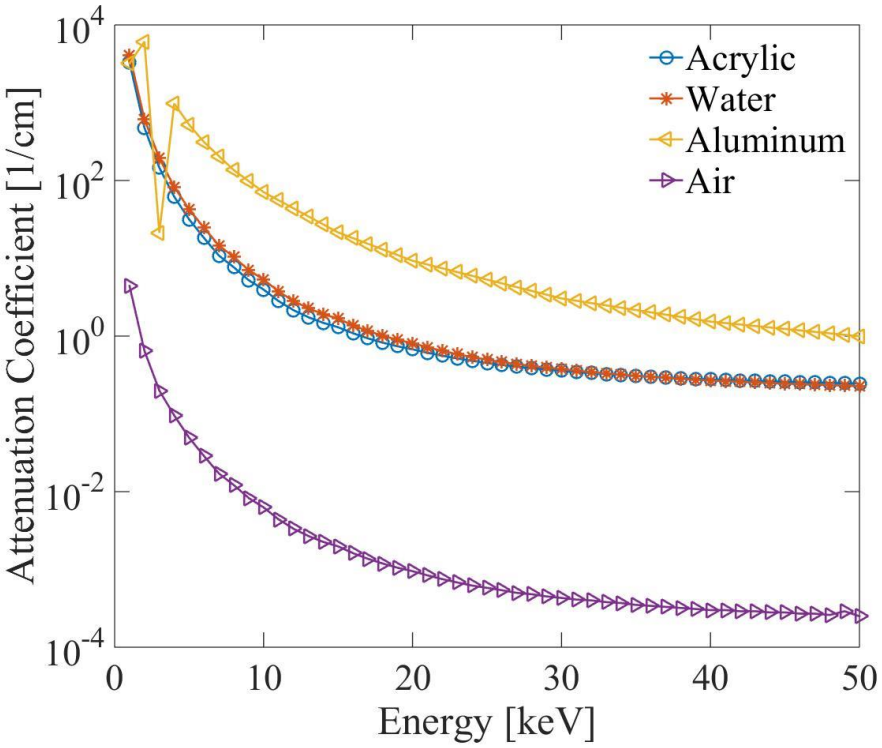

Figure 2-5: Attenuation coefficients for air, water, acrylic, and aluminum. Data from National Institute of Standards and Technology (NIST) [38,40]

Attenuation coefficients can also be used appropriately select an X-ray photon energy level that will generate most contrast between different material composition in a radiographic display [38,42]. For instance, the current study needs to detect and distinguish air, water, and acrylic test section inclusions in beam filtering element (i.e. pure aluminum plate). Note that these two compounds, namely water and air, have different attenuation coefficient as a function of photon energy. Figure 2-5 also illustrates that the maximum separation between air, water, and acrylic curve occurs between 10-50 keV. At this photon energy level range (10-50 keV), the difference in attenuation between three target mediums are at their highest, and hence the radiographic contrast will be maximized.

In Figure 2-5, aluminum coefficient curve exhibit a V-shape profile with sharp discontinuities, which are known as absorption edges and which appear whenever the incident photon energy corresponds to the binding energy of one of the electron shells.

2.1.5 Beam Hardening (Filtration)

Beam hardening is filtration process of the lower-level photon energy, and as a result provides higher averaged photon energy level in the typical polychromatic X-ray emission spectrum [17,43]. Two primary factors for this beam hardening phenomenon are attenuation coefficient and penetration depth of the absorber material. In this experiment, the attenuation coefficient of water and acrylic data is illustrated in Figure 2.5 as a function of photon energy plotted on a log scale. In typical X-ray imaging and computed tomography (CT), photon energy interaction is affected by attenuation coefficient and density variation [16]. To account for the beam hardening effects of low energy photons, calibration development is a must using identical test object material with various thickness with its corresponding attenuation properties. In addition, one can also mitigate the effects of beam hardening by pre-filtering (pre-hardening) the polychromatic X-ray source [17,44]. Note that, pre-filtering is a technique that reshapes the polychromatic energy spectrum profile before the beam is emitted onto the test object to be surveyed [43,45]. Typically, the filtering medium is composed of the homogeneous mixture (i.e. pure aluminum plate) or compound mixture (i.e. acrylic or stainless steel plate) of known attenuation properties.

Figure 2-6 illustrates the simulated normalized photon energy spectra before and after beam hardening effects on various thickness of the aluminum plate. The figure clearly displays the beam hardening effects of the aluminum plate as it filters lower-level energy as it penetrates through a domain. As a result, most of the lower-level energy photons in the spectrum are attenuated within filtering medium as filtering thickness increases when compared to the higher-level energy photons. Such beam-hardening modifies the magnitude of energy spectrum profile and increases in the peak energy level of the X-ray spectra.

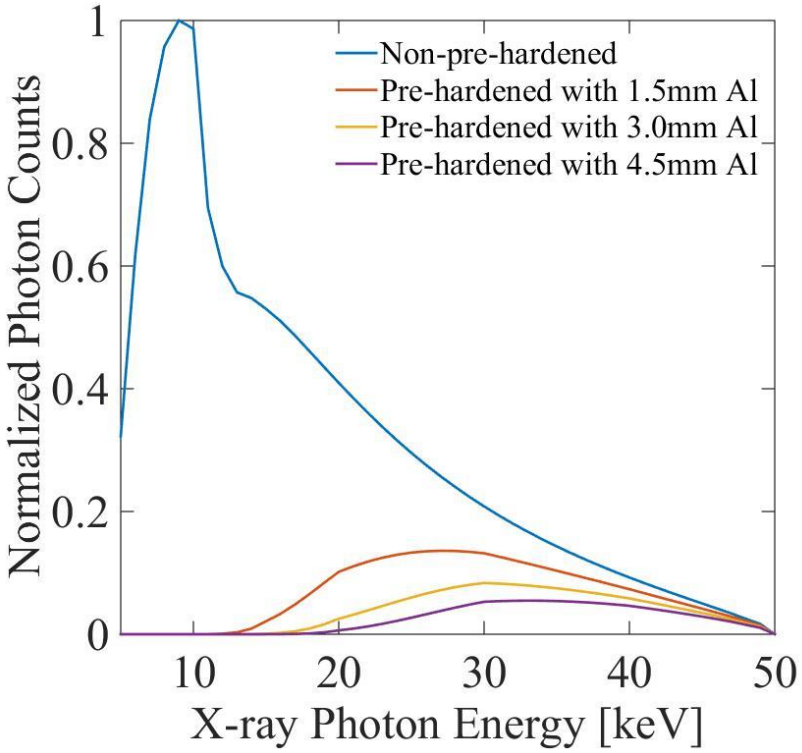

Figure 2-6: X-ray spectra before filtration (plotted in blue line) and after filtering with various thickness with a pure aluminum plate at an effective photon energy of 50keV. As aluminum plate thickness increases, one observes greater attenuation at lower photon energy level. The X-ray spectrum generated using SpecCalc, a software developed by Poludniowski [29–31]

The void fraction expression, Eq. (2.21), has been used by many scientists in related studies [46,47]. Note that a typical non-energy-resolving detector arrangements (like the one that was used in this study) does not measure the intensity value, instead, the detector system converts X-ray photons into visible light for detection by the photodiode array in the pixels' image element.

Thus, one can relate intensity, *I,* to the total number of photons at effective photon energy as one can derive an expression corresponding to actual energy measured by the detector system as [47]:

$$E_{pixel} = A_{pixel} \cdot \Delta t \cdot mA \int_0^{e_{\max}} I(e) \cdot f_{conv}(e)\, dV \tag{2.22}$$

where,

E_{pixel} = total number of electron

A_{pixel} = effective area of detector pixel [mm^2]

Δt = exposure time (sampling time in second) [sec]

mA = operating current [mA]

I = number of X-ray photons per energy level [#photons/keV·mm^2 ·mA·s]

f_{conv} = detector conversion factor [# electrons/X-ray photon]

e = primary photon energy [keV].

The detector conversion factor, f_{conv}, is derived by using unique calibration method. This method utilizes identical test object material with various thickness with identical attenuation properties for which X-ray photons are converted into electrons in the pixel's image element. The current study will provide further detailed calibration experimental method procedure in Chapter 3.1 for the detector conversion factor, f_{conv}.

2.1.6 Spectral Model: Non-Energy Resolver Detector Response

When X-ray photon beam is detected by silicon-based semiconductor detector, a signal charge pulse, *Q,* is produced at each detector pixels with an amplitude that corresponds to certain photon energy level of an X-ray beam [10,18]. From this fact, one can estimate a signal charge pulse of the pixel based on the total number of electrons that were produced from the X-ray photons as shown in Eq. (2.22). Now, a charge Q_{pixel} can be expressed as:

$$Q_{pixel} = \frac{E_{pixel}}{6.242 \times 10^{18} e} \tag{2.23}$$

where,

Q_{pixel} is measured in coulomb unit.

Note, the signal pulse generated by the semiconductor detector increases the input-end potential and output-end potential (with reverse polarity) of the charge amplifier. At the same time, the charge amplifier's open-loop gain is sufficiently large so that the out-put end potential works through a feedback loop mechanism to instantaneously make the input-end potential zero [10,48]. As a consequence, the signal pulse is pooled to the feedback capacitance, C_f, and then as voltage pulse output that can be expressed by:

$$V_{pixel} = \frac{Q_{pixel}}{C_f} \tag{2.24}$$

The substituting equation, Eq. (2.23) into Eq. (2.24) yields:

$$V_{pixel} = \frac{E_{pixel}}{6.242 \times 10^{18} C_f} = \frac{A_{pixel} \cdot \Delta t \cdot mA}{6.242 \times 10^{18} C_f} \int_0^{e_{\max}} I(e) \cdot f_{conv}(e)\, de \tag{2.25}$$

where,

C_f = charge amplifier capacitance [F].

For a specific polychromatic X-ray beam, one can modify Eq. (2.21) to obtain following void fraction:

$$\alpha_{pixel} = \ln\left(\frac{V_{pixel-2\phi} / V_{pixel-fo}}{V_{pixel-g} / V_{pixel-fo}} \right) \tag{2.26}$$

where,

$V_{pixel\text{-}2\emptyset}$ = voltage output for two-phase mixture,

$V_{pixel\text{-}fo}$ = voltage output for the test section with full of fluid (water) that is measured at void fraction of α=0,

$V_{pixel\text{-}go}$ = voltage output for the test section with full of gas (air) that is measured at void fraction of α=1

Eq. (2.26) provides a numerical estimation of the void fraction value along any given X-ray photon beam that penetrates through the two-phase flow structure and detected by the detector pixel's image element where photon energy is converted to electron to generate the output voltage.

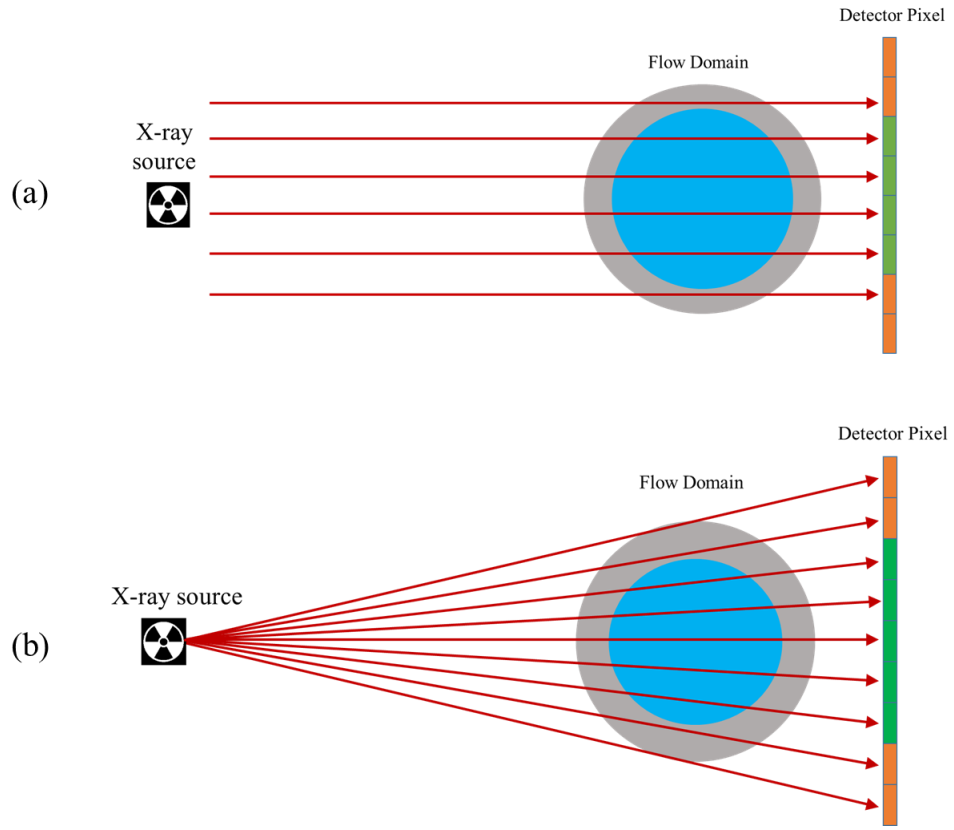

Figure 2-7: Top figure (a) illustrates the case for the line-averaged void fraction along a single parallel line beam can be measured by one pixel in the detector array. Combining the information of all pixels in the detector array, the distribution of the line-averaged void fraction can be achieved in both radial and pixel distribution. The bottom figure (b) illustrates the actual X-ray cone beam condition. Parallel line-beams provides a radial profile, but non-parallel X-ray line beams with direction angle creates a non-radial extended projection of the void fraction distribution in the circular pipe. Therefore, X-ray cone beam does not represent the radial distribution profile as is indicated by the pixel distribution.

2.2 X-Ray Cone Beam Correction

Non-radial void fraction distribution of an X-ray cone beam (composed of line beams with direction angle) is illustrated in Figure 2-7. Here, the flow domain has a perfect averaged one-dimensional projection of void fraction information ranging from zero to one at each detector pixel. However, one cannot reflect the X-ray cone beam to correct the line beam angles for a polychromatic X-ray source as was the case in this study.

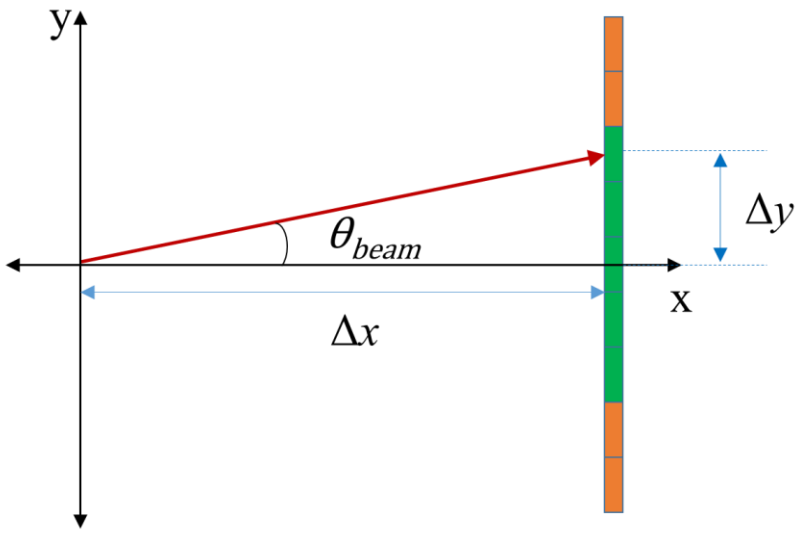

Figure 2-8: Line beam vector with beam angle

Here, each line-beam is a function of beam angle from the source to the detector's normal surface. One can express beam angle at n_{th} pixel as follows:

$$\theta_{beam\ @\ \text{nth}\ pixel} = \tan^{-1}\left(\frac{\Delta y_{nth}}{\Delta x}\right) \tag{2.27}$$

where,

Δx is distance from source to detector center location in x-direction

Δy_{nth} is the location of n_{th} detector pixel in the y-direction from detector center location.

Equating beam angle equation, one can specify the source to detector pixel distance (SPD) factor as follows:

$$SPD = \frac{\Delta x}{\cos(\theta_{beam\ @\ \text{nth}\ pixel})}. \tag{2.28}$$

2.2.1 Mathematical Description of Circular Test Section and X-ray Line Beam

Cross-section of the circular test section is better modeled as an ellipse because this conic shape accounts for the distorted cross-section of circular test section better than a perfect circle. Also, the cross-section of circular test section aspect ratio and line beam angle which may be critical to the X-ray measurement are better described by an elliptical (cross-section area of circular test section) model. First, several coordinate systems need to be defined in order to define the mathematical description of this elliptical object.

In the X-ray measurement plane, a source of the X-ray beam is considered to be a point because of the focal spot on the anode target is very small. In the mathematical description of the X-ray beam assume that the source creates narrow X-ray line beams.

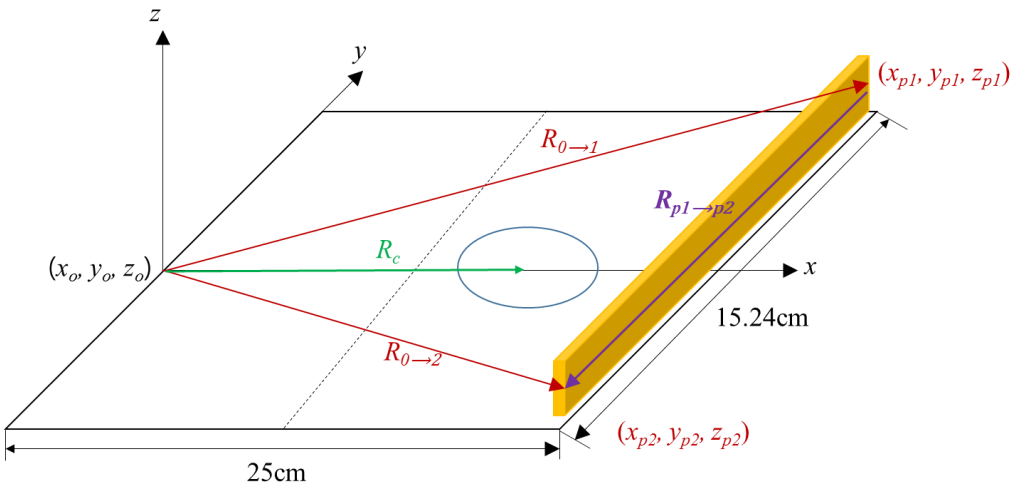

Figure 2-9: A typical global coordinate system *o-xyz* fixed to the origin of the X-ray source in the X-ray measurement system.

Suppose that one has a reference X-ray system in the 3D coordinate system. One then can define a global coordinate system *o-xyz* fixed to the X-ray measurement plane at the origin (i.e. *o-xyz* = 0,0,0) of the coordinate system and axes parallel to the edges of the system boundary as illustrated in Figure 2-9. A cross-section of a circular pipe is defined/located along the plane that contains the vector $\vec{R}_c$, and pixels are located along the vector $\vec{R}_{p1\to p2}$ that is defined between

vectors $\vec{R}_{0\to1}$ (start point of pixel array) and $\vec{R}_{0\to2}$ (end point of the pixel array). Note that vector $\vec{R}_{p1\to p2}$ represents a location of each pixel relative to X-ray beam origin and can be expressed as:

$$\vec{R}_{p1\to p2} = \begin{Bmatrix} x_{p1} + (x_{p2} - x_{p1})t_{pixel} \\ y_{p1} + (y_{p2} - y_{p1})t_{pixel} \\ z_{p1} + (z_{p2} - z_{p1})t_{pixel} \end{Bmatrix}; 0 \le t_{\text{pixel}} \le 1 \tag{2.29}$$

Consequently, arising from above results, one can define X-ray line beam in the global coordinate system as:

$$\vec{R}_{beam} = \begin{Bmatrix} x_{p1} + (x_{p2} - x_{p1})t_{pixel} - x_o \\ y_{p1} + (y_{p2} - y_{p1})t_{pixel} - y_o \\ z_{p1} + (z_{p2} - z_{p1})t_{pixel} - z_o \end{Bmatrix}; 0 \le t_{\text{pixel}} \le 1 \tag{2.30}$$

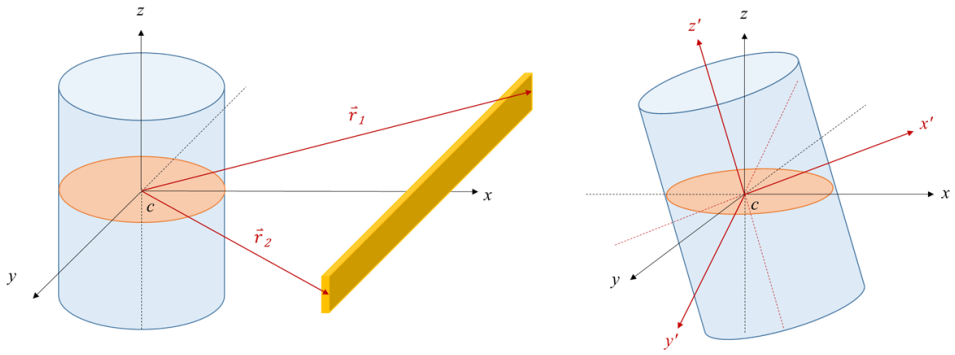

(a) (b)

Figure 2-10: (a) Local coordinate system *c-xyz*; and (b) local coordinate system *c-x'y'z'*

The Figure 2-10 (a) illustrates a local coordinate system *c-xyz* that is similar to the coordinate system as *o-xyz* but now with the origin located in the pipe center, c; and Figure 2.10

(b) displays a local coordinate system *c-x'y'z'* that has the same origin as *c-xyz,* but with its axes, $x'_c y'_c$, and z'_c, parallel to the semi-principal axes of an ellipse (cross-section of circular pipe). In the local coordinate system *c-xyz*, vector $\vec{r}_1$ (start pixel location) and $\vec{r}_2$ (end pixel location) are relative to the pipe center location and can be described as:

$$\begin{aligned} \vec{r}_1 &= \vec{R}_{0\to 1} - \vec{R}_c \\ \vec{r}_2 &= \vec{R}_{0\to 2} - \vec{R}_c \end{aligned} \tag{2.31}$$

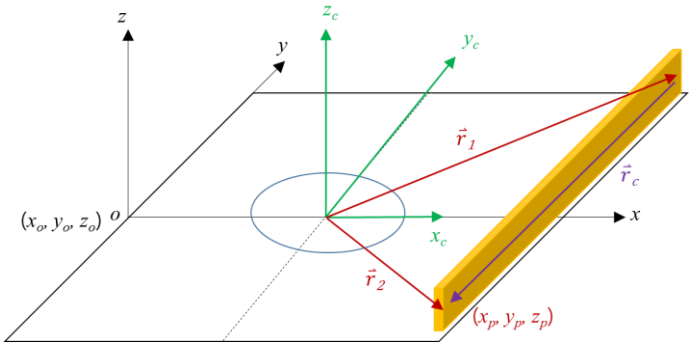

Figure 2-11: Shifted coordinate system where the center of pipe location in local coordinate system *c-xyz*.

Here, one can determine the line beam contact-points by a local coordinate system along with the quantitative local coordinate system description and is given as follows:

$$\vec{r}_c = \begin{Bmatrix} x' = x_o + (x_p - x_o)t_{pixel} - x_c \\ y' = y_o + (y_p - y_o)t_{pixel} - y_c \\ z' = z_o + (z_p - z_o)t_{pixel} - z_c \end{Bmatrix} \tag{2.32}$$

Finally, Eq. (2.32) becomes a new line equation.

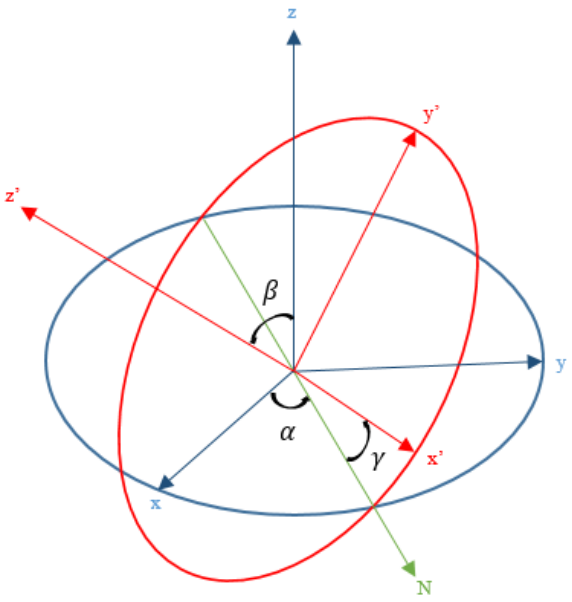

Figure 2-12: Illustration of rotation angles.

The local coordinate system *c-x'y'z'* can be obtained by rotating the coordinate system *c-xyz* in following three steps (refer to the Figure 2-12):

Step 1: Rotate angle γ about z'-axis to make x' parallel to $\vec{N}$, here γ represents a rotation around the z' axis.

Step 2: Rotate β about $\vec{N}$ to make z-axis parallel to z'- axis, here β represents a rotation around the N axis.

Step 3: Rotate α about z- axis to be local coordinate system c-x'y'z', here α represents a rotation around the z axis

Note, if β is zero then there is no rotation about $\vec{N}$. As a consequence, z' coincides with z; α and γ represent rotation about the same z-axis; and the final orientation can be obtained with a single rotation about z, by an angle equal to $\alpha+\gamma$.

Consequently, arising from above results, any point in c-xyz can be converted to c-*x'y'z'* coordinate with the rotation matrix:

$$
\begin{aligned}
M &= R_{z'}(\alpha)R_{N}(\beta)R_{z}(\gamma) \\
&= \begin{pmatrix} \cos\alpha & -\sin\alpha & 0 \\ \sin\alpha & \cos\alpha & 0 \\ 0 & 0 & 1 \end{pmatrix} \cdot \begin{pmatrix} 1 & 0 & 0 \\ 0 & \cos\beta & -\sin\beta \\ 0 & \sin\beta & \cos\beta \end{pmatrix} \cdot \begin{pmatrix} \cos\gamma & \sin\gamma & 0 \\ \sin\gamma & \cos\gamma & 0 \\ 0 & 0 & 1 \end{pmatrix} \\
&= \begin{pmatrix} \cos\alpha\cdot\cos\gamma - \cos\beta\cdot\sin\alpha\cdot\sin\gamma & -\cos\gamma\cdot\cos\alpha\cdot\sin\alpha - \cos\alpha\cdot\sin\gamma & \sin\alpha\cdot\sin\beta \\ \cos\gamma\cdot\sin\alpha + \cos\alpha - \cos\beta\cdot\sin\gamma & \cos\alpha\cdot\cos\beta\cdot\cos\gamma - \sin\alpha\cdot\sin\gamma & -\cos\alpha\cdot\sin\beta \\ \sin\beta\cdot\sin\gamma & \cos\gamma\cdot\sin\beta & \cos\beta \end{pmatrix}
\end{aligned}
\tag{2.33}
$$

Moreover, the pixel contact coordinate system can also be converted to $\vec{r}'$ in the *c-x'y'z'* coordinate system and is defined as:

$$
\begin{aligned}
\vec{r}' &= M \cdot \vec{r}_c \\
&= \begin{pmatrix} (x_o + (x_p - x_o)t_{pixel} - x_c)\cdot M_{11} + (y_o + (y_p - y_o)t_{pixel} - y_c)\cdot M_{12} + (z_o + (z_p - z_o)t_{pixel} - z_c)\cdot M_{13} \\ (x_o + (x_p - x_o)t_{pixel} - x_c)\cdot M_{21} + (y_o + (y_p - y_o)t_{pixel} - y_c)\cdot M_{22} + (z_o + (z_p - z_o)t_{pixel} - z_c)\cdot M_{23} \\ (x_o + (x_p - x_o)t_{pixel} - x_c)\cdot M_{31} + (y_o + (y_p - y_o)t_{pixel} - y_c)\cdot M_{32} + (z_o + (z_p - z_o)t_{pixel} - z_c)\cdot M_{33} \end{pmatrix} \\
&= \begin{pmatrix} (x_o M_{11} + y_o M_{12} + z_o M_{13}) + t_{pixel}[(x_p - x_o)M_{11} + (y_p - y_o)M_{12} + (z_p - z_o)M_{13})] - (x_c M_{11} + y_c M_{12} + z_c M_{13}) \\ (x_o M_{21} + y_o M_{22} + z_o M_{23}) + t_{pixel}[(x_p - x_o)M_{21} + (y_p - y_o)M_{22} + (z_p - z_o)M_{23})] - (x_c M_{21} + y_c M_{22} + z_c M_{23}) \\ (x_o M_{31} + y_o M_{32} + z_o M_{33}) + t_{pixel}[(x_p - x_o)M_{31} + (y_p - y_o)M_{32} + (z_p - z_o)M_{33})] - (x_c M_{31} + y_c M_{32} + z_c M_{33}) \end{pmatrix} \\
&= \begin{pmatrix} Q_1 + (t_{pixel}\cdot Q_2) - Q_3 \\ Q_4 + (t_{pixel}\cdot Q_5) - Q_6 \\ Q_7 + (t_{pixel}\cdot Q_8) - Q_9 \end{pmatrix}
\end{aligned}
\tag{2.34}
$$

where,

$$Q_1 = x_o M_{11} + y_o M_{12} + z_o M_{13}$$
$$Q_2 = (x_p - x_o) M_{11} + (y_p - y_o) M_{12} + (z_p - z_o) M_{13}$$
$$Q_3 = x_c M_{11} + y_c M_{12} + z_c M_{13}$$
$$Q_4 = x_o M_{21} + y_o M_{22} + z_o M_{23}$$
$$Q_5 = (x_p - x_o) M_{21} + (y_p - y_o) M_{22} + (z_p - z_o) M_{23}$$
$$Q_6 = x_c M_{11} + y_c M_{12} + z_c M_{13}$$
$$Q_7 = x_o M_{31} + y_o M_{32} + z_o M_{33}$$
$$Q_8 = (x_p - x_o) M_{31} + (y_p - y_o) M_{32} + (z_p - z_o) M_{33})$$
$$Q_9 = x_c M_{31} + y_c M_{32} + z_c M_{33}$$

Recall that one can describe an ellipse in *c-x'y'z'* coordinate system in a conventional way as:

$$\frac{x'^2}{a^2} + \frac{y'^2}{b^2} = 1 \tag{2.35}$$

Here, coefficients *a* and *b* are the length of semi-principal axes of an ellipse. With the results of Eq. (2.34), the equation of the ellipse in the *c-xyz* coordinate system can also be obtained.

2.2.2 Chord Length and Measured Parameters

Once the circular test section center and X-ray line beams are defined, the circular test section and X-ray line beam contact point (chord length coordinate points) can be solved and is illustrated in the following procedure:

Step1: Determine the contact point, $\overrightarrow{r'}$, by using the X-ray line beam equations, the actual pipe center location, pixel locations, and the Eq. (2.33). Then substitute $\overrightarrow{r'}$ into the ellipse equation, Eq. (2.34), and Eq. (2.35) should yield:

$$\frac{(Q_1 + (t_{pixel} \cdot Q_2) - Q_3)^2}{a^2} + \frac{(Q_4 + (t_{pixel} \cdot Q_5) - Q_6)^2}{b^2} - 1 = 0 \tag{2.36}$$

After some rearranging, Eq. (2.36) yields characteristic polynomial equation with coefficients:

$$\begin{aligned} &Ax^2 + Bx + C = 0 \\ &A = b^2Q_2{}^2 + a^2Q_5{}^2 \\ &B = 2b^2Q_1Q_2 + 2b^2Q_2Q_3 + 2a^2Q_4Q_5 - 2a^2Q_5Q_6 \\ &C = b^2Q_1{}^2 + b^2Q_3{}^2 - 2b^2Q_1Q_3 + a^2Q_4{}^2 + a^2Q_6{}^2 - 2a^2Q_4Q_6 - a^2b^2 \end{aligned} \tag{2.37}$$

Step 2: Calculate the discriminant δ which would determine whether this circular test section is detected by the X-ray line beam:

$$\delta = B^2 - 4AC \begin{cases} > 0 \text{ X-ray line beam penetrates pipe} \\ = 0 \text{ X-ray line beam tangent to the pipe wall} \\ < 0 \text{ X-ray line beam misses pipe} \end{cases} \tag{2.38}$$

Above determinant analysis can be summarized as follows for the circular test section:

$$\begin{aligned} &\delta > 0, \quad \text{Effective test section region} \\ &\delta < 0, \quad \text{Ineffective test secton region} \end{aligned}$$

Step 3: Substitute effective test section region δ value into quadratic formula to obtain two coordinate points of an ellipse (cross-section of circular pipe) or X-ray line beams on the measurement plane:

$$x = \frac{-B \pm \sqrt{B^2 - 4AC}}{2A} = \frac{-B \pm \sqrt{\delta}}{2A} \tag{2.39}$$

Step 4: Now, substitute the result of Eq. (2.39) (input x-coordinates) in the ellipse equation, Eq. (2.35), to obtain the y-coordinates. To find the chord length of the circular test section (distance between two points (x_1, y_1) and (x_2, y_2) of the ellipse), use the typical distance formula to yield:

$$l_{chord} = \sqrt{(x_1 - x_2)^2 + (y_1 - y_2)^2} \tag{2.40}$$

2.3 Void Fraction Conversion Algorithm: Pixel to Radial Profile

Line averaged void fraction information received by the detector pixel (from forward projection beam) does not represent the radial void fraction profile. This is due to X-ray's non-parallel beam and non-radial extended projection of the void fraction distribution in the circular pipe, refer to the Figure 2-7. The primary objective of this section is to develop a conversion algorithm for the radial void fraction profile from detector pixel distribution.

2.3.1 Coverage Area of X-ray Line Beam

Cross-section of the circular pipe (ellipse) and flow profile are assumed to exhibit an axial symmetry. Combining void fraction information of all detector pixels, the line averaged (forward projection of the X-ray beam) void fraction can be obtained. Let's suppose that one need to define flow area measured by X-ray line beam where the beam is detected by the pixel. Now, the void fraction information measured at each pixel represents area-averaged void fraction information. Based on previous assumptions, the flow area measured by X-ray line beam and detector pixel are modeled by the following procedures:

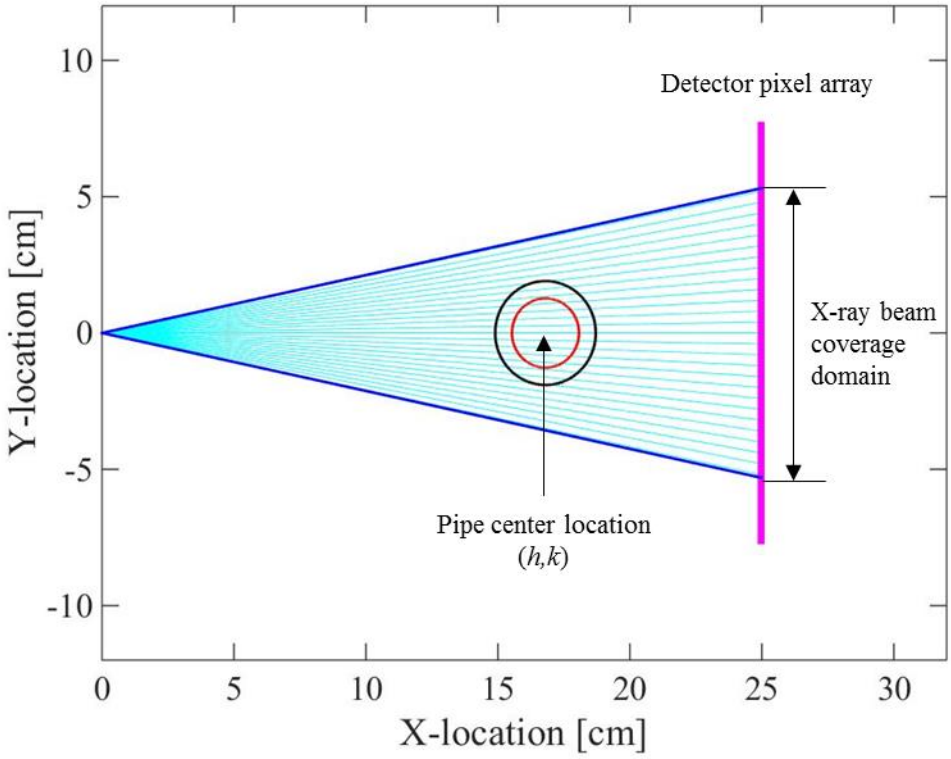

Figure 2-13: Illustration shows X-ray beam coverage domain, location of the detector, and pipe center location in the X-ray measurement plane. X-ray cone beam (composed of line beams plotted in blue lines) indicate the effective line beam region that is from source to detector array (plotted in purple line). Pipe center location (*h, k*) is placed in the line beam effective region under the *x* and *y* domain restrictions; outer pipe structure (plotted with a black circle) and two-phase flow region (plotted in red circle).

Step 1: Define pipe center location within X-ray line beam coverage domain in the X-ray measurement plane:

$$\frac{(x-h)^2}{a^2}+\frac{(y-k)^2}{b^2}=1 \tag{2.41}$$

where,

a and *b* are the length of semi-principal axes of an ellipse (cross-section of circular pipe)

h and *k* are *x- and y*-coordinates of the center of an ellipse (cross-section of circular pipe).

Note: Center of an ellipse (*h,k),* pipe center location, must be located within x- and y-domain ranges of the X-ray line beam coverage domain in order to obtain void fraction information of entire two-phase flow structure (refer to the Figure 2.13).

The x-domain range is defined by the following equation:

$$x_{domain} = \left[x_o + \frac{r_{pipe}}{\tan(\theta_{beam\ \max})} \ \leq\ x \leq\ \Delta x - r_{\text{pipe}} \right] \tag{2.42}$$

From the x_{domain}, one can calculate the maximum potential value of *y, y_{max}*, in the X-ray coverage domain in the circular cross-section of the test section. The maximum potential value of *y, y_{max}*, is defined as follows:

$$y_{\max} = (\Delta x - r_{\text{pipe}}) \cdot \tan(\theta_{beam\ \max}) \tag{2.43}$$

Next step is to determine the y-domain range, y_{domain}. Also note here that the y-domain is function of x-domain and is defined as:

$$y_{domain}(x_{domain}) = \ \pm \left[\frac{(y_{\max} - r_{\text{pipe}}) - y_o}{(\Delta x - r_{\text{pipe}}) - \left(x_o + \dfrac{r_{pipe}}{\tan(\theta_{beam\ \max})} \right)} \right] \cdot x_{domain} \tag{2.44}$$

where,

x_o, and y_o are X-ray source location

Δx is the X-ray source to detector center distance

$\theta_{beam\ max}$ is the maximum X-ray beam angle

x_{domain} is possible ranges for the pipe center location

y_{domain} is the possible ranges for the pipe center location

r_{pipe} is the outer radius of the pipe

Step 2**:** Define an equation of the X-ray line beams in the X-ray beam effective region between *x*- and *y*-domain:

$$y_{line\ beam} = g(x)_{line\ beam} = \frac{\Delta y_{nth} - y_o}{\Delta x - x_o} \cdot x \tag{2.45}$$

where,

x_o, and y_o are X-ray source location

Δx is the X-ray source to detector center distance

Δy_{nth} is y location of the detector pixel in the measurement plane.

Step 3: Repeat the process using equations Eq. (2.35) through Eq. (2.38) to obtain (x_1, y_1) and (x_2, y_2), intersection points of an ellipse (cross-section of circular pipe) and n_{th} X-ray line beams. Once $A(x_1, y_1)$ and $B(x_2, y_2)$ are obtained, one can now calculate the segment area of an ellipse. Repeat the same process to find $C(x_1, y_1)$ and $D(x_2, y_2)$ that corresponds to the intersection of an ellipse with the n_{th+1} pixel. Finally, calculate the segment area between the n_{th+1} and n_{th} pixel to obtain a flow area (*ABDC*) as a function of an n_{th} pixel location (refer to Figure 2-14 for a visual illustration of step 3).

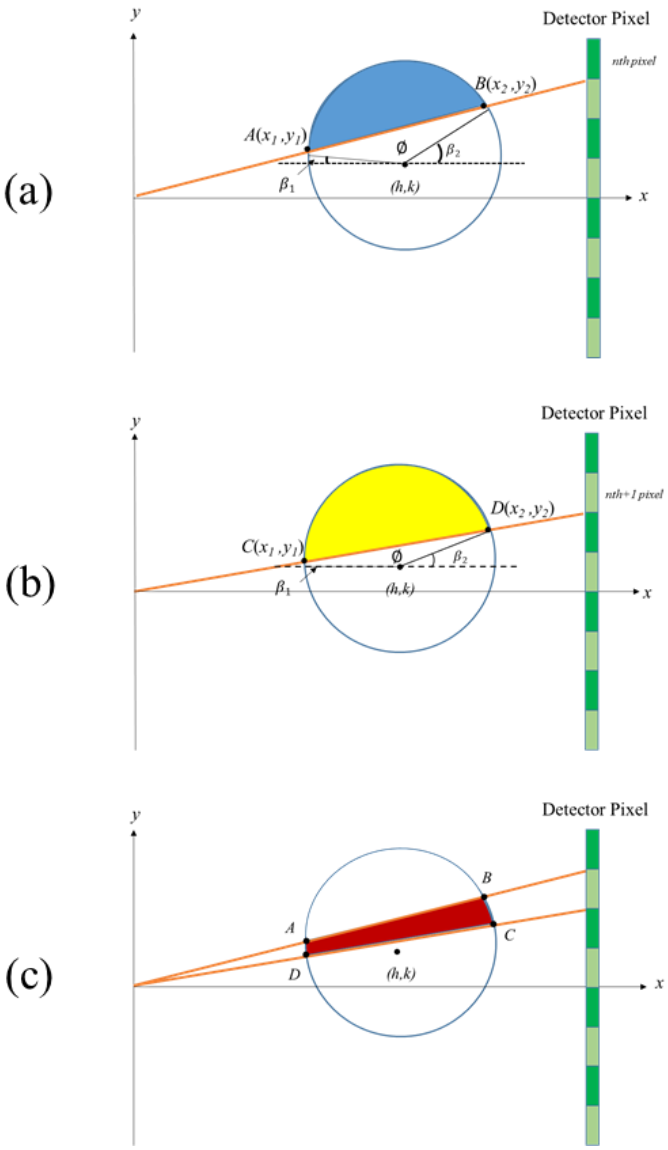

Figure 2-14: (a) segment area AB (in blue) associate at the n_{th} pixel location, (b) segment area CD associated at the following pixel, $n+1_{th}$, and (c) flow area (ABDC) measured by the n_{th} pixel.

An elliptical equation, Eq. (2.40), can be expressed as:

$$y_{ellipse} = f(\mathrm{x})_{ellipse} = \pm\sqrt{\frac{(a^2 \cdot b^2) - [b^2 \cdot (x-h)^2]}{a^2}} + k \qquad (2.46)$$

Intersection points of Eq. (2.44) and Eq. (2.45) are at x_1 and x_2. These points will serve as the upper- and lower-bounds of the integral function to compute the segment area and is defined by the following:

$$A_{segment} = \begin{cases} \int_{x1}^{x2} f(\mathrm{x})_{ellipse} - g(\mathrm{x})_{line\ beam}\ dx, & x_1 \le x \le x_2, \text{ if } f(\mathrm{x})_{ellipse} \text{ is upper function} \\ \int_{x1}^{x2} g(\mathrm{x})_{line\ beam} - f(\mathrm{x})_{ellipse}\ dx, & x_1 \le x \le x_2, \text{ if } f(\mathrm{x})_{ellipse} \text{ is lower function} \end{cases} \quad (2.47)$$

Here, simply find the difference between segment area of the following pixel (n_{th+1}) and preceding pixel (n_{th}) to find the flow area (ABDC) as a function of n_{th} pixel location:

$$A_{nth\ pixel} = A_{segment(nth+1\,pixel)} - A_{segment(nth\ pixel)} \quad (2.48)$$

where,

$A_{nth\ pixel}$ is the flow area measured by X-ray line beam at each n_{th} detector pixel.

Note here that an area measured by X-ray line beam at each n_{th} pixel represents averaged void fraction information in that particular areas segment. Moreover, this information does not represent the radial void fraction profile, hence, one need to divide the area measured by X-ray line beams at each n_{th} pixel (refer to Figure 2.14(c)) into concentric circular-partitioned rings in accordance with the radial profile.

Step 4: To obtain the radial void fraction profile, one need to partitioned the circular cross-section of the test region into concentric circular-partitioned rings with different radii inside of the two-phase region (refer to the Figure 2.15(a)). Note, the maximum number of partitioned rings should be equal to half of the total number of pixels that covers the entire two-phase flow region.

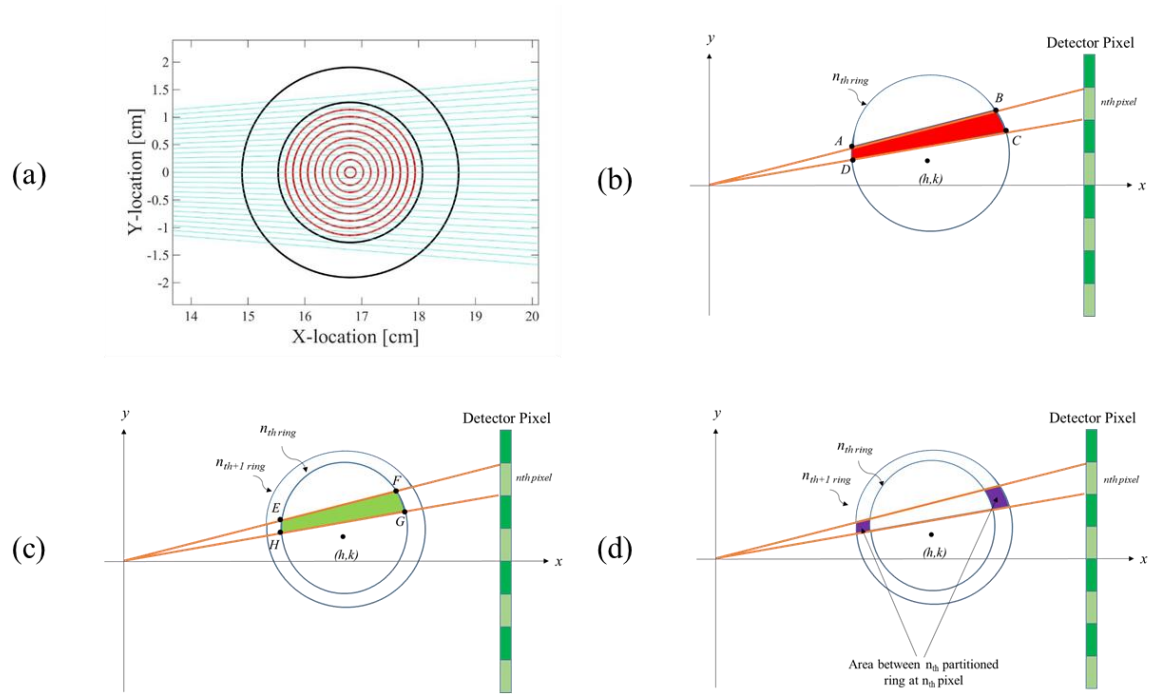

Figure 2-15: (a) Two-phase flow region is divvied into number of partitioned rings; (b) flow area (ABCD) measured by the n_{th} detector pixel at n_{th} partitioned ring; (c) flow area (EFGH) measured by the same (n_{th}) doctor pixel at next successive (n_{th}+1) partitioned ring; and (d) partitioned sector area between n_{th} and n_{t+1} partitioned ring at n_{th} detector pixel location, partitioned sector area is difference between area (ABCD) and area (EFGH).

Repeat step 3 and 4 to obtain an area of all partition-rings as measured by the X-ray line beam at each detector pixel. This area of the partitioned sector is defined as a function of the radius of the each partitioned ring (refer to the Figure 2.15):

$$A_{\text{sector}(R_{\#n})} = A_{nth\ pixel(R_{\#n})} - A_{nth\ pixel(R_{\#n+1})} \tag{2.49}$$

where,

$A_{secotor}$ is the area of partitioned sector (area between ring #n and ring # n+1 in the $A_{nth\ pixel}$),

R is the radius of the n_{th} partitioned ring.

Now, from Eq. (2.49), one can express radial distribution at each partitioned sector as follows:

$$\sum_{i=1}^{N} \alpha_R(R_{\#n}) \cdot \frac{A_{sector(R_{\#n})}}{A_{nth\ pixel}} = \alpha_{nth\ pixel} \tag{2.50}$$

where,

α_R = radial void fraction (at n_{th} partitioned ring),

$\alpha_{nth\ pixel}$ = measured time and line averaged void fraction information at n_{th} pixel,

A_{sector} = area of partitioned sector (area between n_{th} and n_{th+1}partitioned ring),

$A_{nth\ pixel}$ = area measured by X-ray line beam at n_{th} pixel.

Step 5: Cross-section of the circular (elliptical) test-section and flow profiles exhibit axial symmetry. With results of Eq. (2.50) area of each partitioned sector, one can simplify the calculation by modifying the matrix in a tri-diagonal form as shown below:

$$\begin{bmatrix} \frac{A_{ring\#1}}{A_{pixel\#1}} & \frac{A_{ring\#2}}{A_{pixel\#1}} & \frac{A_{ring\#3}}{A_{pixel\#1}} & \cdots & \frac{A_{ring\#n\text{-}1}}{A_{pixel\#1}} & \frac{A_{sector(R_{\#n})}}{A_{pixel\#1}} \\ 0 & \frac{A_{ring\#2}}{A_{pixel\#2}} & \frac{A_{ring\#3}}{A_{pixel\#2}} & \cdots & \frac{A_{ring\#n\text{-}1}}{A_{pixel\#2}} & \frac{A_{sector(R_{\#n})}}{A_{pixel\#2}} \\ 0 & 0 & \frac{A_{ring\#3}}{A_{pixel\#3}} & \cdots & \frac{A_{ring\#n\text{-}1}}{A_{pixel\#3}} & \frac{A_{sector(R_{\#n})}}{A_{pixel\#3}} \\ \vdots & \vdots & \ddots & \cdots & \vdots & \vdots \\ 0 & 0 & 0 & \cdots & \frac{A_{ring\#n\text{-}1}}{A_{pixel\#n\text{-}1}} & \frac{A_{sector(R_{\#n})}}{A_{pixel\#n\text{-}1}} \\ 0 & 0 & 0 & \cdots & 0 & \frac{A_{sector(R_{\#n})}}{A_{pixel\#n}} \end{bmatrix} \times \begin{bmatrix} \alpha_{R(R_{\#1})} \\ \alpha_{R(R_{\#2})} \\ \alpha_{R(R_{\#3})} \\ \vdots \\ \alpha_{R(R_{\#n-1})} \\ \alpha_{R(R_{\#n})} \end{bmatrix} = \begin{bmatrix} \alpha_{pixel\#1} \\ \alpha_{pixel\#2} \\ \alpha_{pixel\#3} \\ \vdots \\ \alpha_{pixel\#n-1} \\ \alpha_{pixel\#n} \end{bmatrix} \tag{2.51}$$

Here, reduce results of Eq. (2.51) matrix equation format, into:

$$A \cdot \alpha_R = \alpha_{pixel} \tag{2.52}$$

where,

A is the area matrix (left) of the Eq. (2.51),
α_R is the radial void fraction matrix of the Eq. (2.51),
α_{pixel} is the pixel void fraction matrix of the Eq. (2.51).

Finally, one can employ Gaussian eliminations with back-substitution to isolate the radial void fraction, α_R, *i.e.,* multiply both sides with inverse area matrix A^{-1}:

$$\alpha_{Radial} = A^{-1} \cdot \alpha_{pixel} \tag{2.53}$$

With the results of Eq. (2.53), now one have radial void fraction profile from the void fraction distribution from the pixel.

2.3.2 Gas Velocity Measurement

A signal processing with cross-correlation technique has been used in the two-phase flow for flow velocity measurement in the past [49,50]. In particular, a cross-correlation function (CCF) was an essential tool for an X-ray signal processing for the gas velocity measurement in this study. A typical cross-correlation function is frequently modeled as a parametric function of time delay estimation with a parabolic fit interpolation as model parameters are determined by fitting sample data near the maximum of the CCF [50,51].

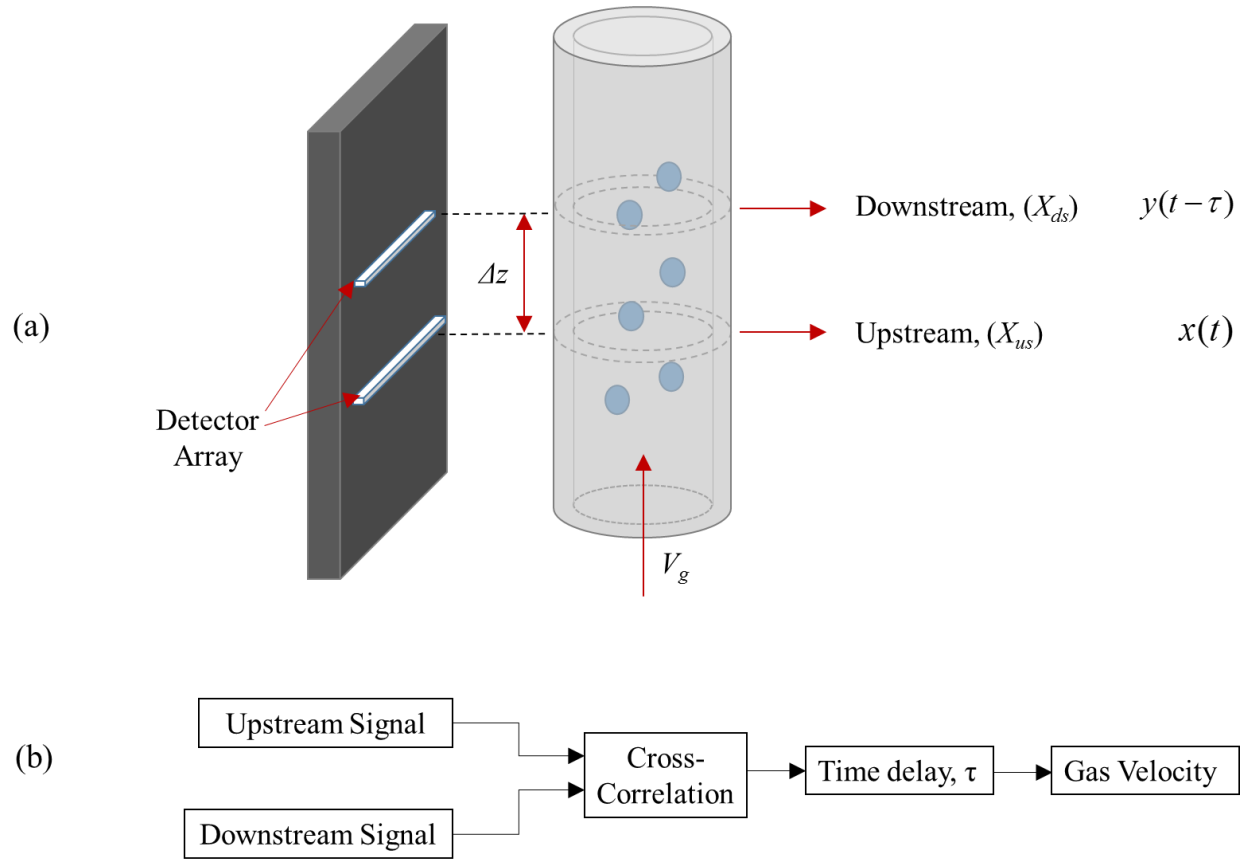

Figure 2-16: (a) Two-measurement plane of X-ray detector arrays. (b) The principle of gas velocity measurement using cross-correlation method using two X-ray signals of upstream signal and downstream signal.

In the X-ray measurement plane, a cross-correlation is a technique that compares the upstream X-ray signal with downstream X-ray signal and then multiplies the corresponding instantaneous values to determine the average of two signal information [49]. Refer to Figure 2.16 for cross-correlation method using two X-ray signals of two-phase flow. A typical CCF delivers graph of the cross-correlation coefficient value against parametric time shift of two X-ray detector signals. Also, CCF graph will measure the similarity of two signal series and the relationship between the two X-ray signals; and the maximum value of the cross-correlation function means that two X-ray signals are more nearly the same for that particular time delay [51]. Note, a CCF measurement is based on measuring the CCF data from two X-ray signals spaced vertically along the two-phase flow stream. The time delay of the maximum CCF value provides

a signal indication of the flow transit time between two different X-ray detector arrays, and from this, the actual flow measurement is obtained [52]. The CCF of two X-ray signal data describes the overall dependence of the values of an upstream set of data on the downstream signals.

(a)

(b)

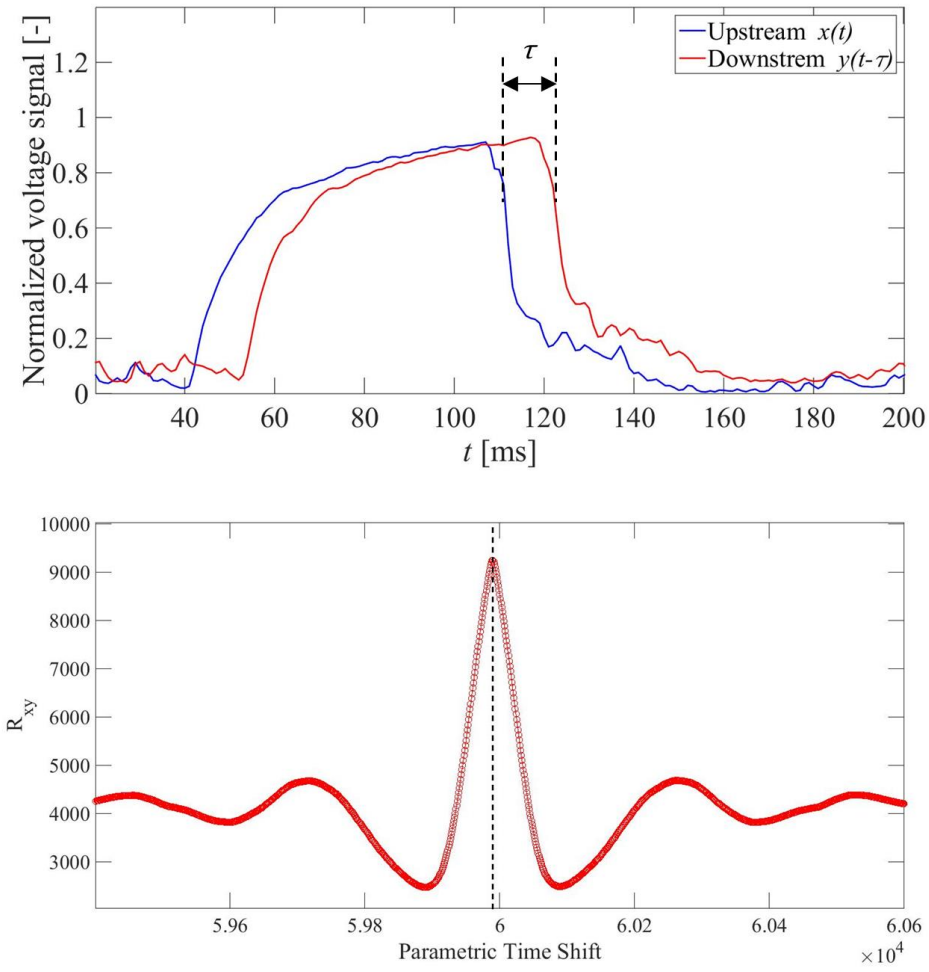

Figure 2-17: (a) Graph shows an upstream and downstream X-ray signals. (b) Cross-correlation function from both X-ray signals

In essence, the X-ray signal patterns in the two-phase flow stream travels without X-ray signal distortion between upstream X-ray, X_{us}, and downstream X-ray, X_{ds}, as shown in the Figure Figure 2-16(a). This no-distortion assumption in the signal pattern enables the basic principles

of cross-correlation flow measurement to be presented in an easily comprehensible theoretical background [50]. The cross-correlation method of two-phase flow measurement is based on the determination of the transit time, τ, of a measurable X-ray signal disturbance moving along the vertical flow pipe over an exactly known distance of two detector arrangement, Δz. Referring to the Figure 2-17, $x(\tau)$ denotes the X-ray signal derived from upstream, X_{us}, similarly, $y(t-\tau)$ is the signal relate to the value of the measured parameter at downstream, X_{ds}, X-ray detector arrangement. Cross-correlation function, $R_{xy}(t)$, of two X-ray detector signals are given by:

$$R_{xy}(t) = \int_{-T}^{T} x(\tau) y(t-\tau)\, d\tau \tag{2.54}$$

where,

$x(\tau)$ = upstream signal (center detector arrangement-6'' detector)

$y(t-\tau)$ = downstream signal (top detector arrangement-4'' detector) with time delay τ

τ = time delay

T = integration time

The maximum value of $R_{xy}(t)$ occurs at $\tau=\tau^*$ when the correlation delay time τ is equal to the transit time τ^* of the measured parameter of two-phase flow between upstream and downstream. Therefore, a gas velocity of the two-phase flow is given by:

$$V_g = \frac{\Delta z}{n \cdot \tau^*} = \frac{\Delta z}{n \cdot \Delta t} = \frac{\Delta z}{n \cdot (N_s / f)} \tag{2.55}$$

where,

Δz = distance between two detector arrangement [m]

n = peak position of signal

N_s = total number of sample

τ^* = transit time [sec]

f = sampling frequency.

3. CALIBRATION AND EXPERIMENT

3.1 Calibration Experiment

Calibration experiment involved three-step process: (1) attenuated X-ray conversion into visible light; (2) visible light transportation; and (3) visible light conversion into voltage signal [21,22]. In the first step, attenuated X-ray beam conversion into visible light, a scintillator (Gd_2O_2S:Tb, Gadolinium Oxysulfide) of known overall conversion efficiency of around 15% (varies with primary photon energy) was utilized [53,54]. However, energy-dependent efficiency data of the scintillator and the complementary metal-oxide-semiconductor (CMOS) were not available in this calibration experiment. Therefore, a calibration experiment was performed to quantify the overall conversion efficiency and its dependence of photon energy. In the calibration experiment, an acrylic container is placed between the x-ray source and the detector array as illustrated in Figure 3.1. Then, filtered water is injected with a syringe to achieve desired depth. Finally, an X-ray system is turned on, and the voltage levels of corresponding water depth are recorded at the detector end. Here, water depth ranging from 8 mm to 50 mm with 1 mm increment was repeated to obtain various voltage reading of different water depths. The voltage output displayed by each pixel is described by:

$$V_{pixel} = \frac{A_{pixel} \cdot \Delta t \cdot mA}{6.242 \times 10^{18} C_f} \int_0^{e_{\max}} I(e) \cdot f_{conv}(e) \; de \tag{3.1}$$

where,

E_{pixel} is total # of electron

V_{pixel} is voltage output displayed by each pixel [V]

A_{pixel} is effective area of detector pixel [mm^2]

Δt is exposure time (sampling time in second) [sec]

mA is operating current [mA]

I is number of X-ray photons per energy level [#photons/keV·mm^2 ·mA·sec]

f_{conv} is detector conversion factor [# electrons/X-ray photon]

e is primary photon energy [keV]

C_f is charge amplifier capacitance [F]

Recall, the total electrical energy detected by each pixel can be calculated based on the charge amplifier feedback capacitance of the detector for a polychromatic X-ray source as described by Eq. (2.22) to Eq. (2.24). In the Eq. (3.1), current study proposes a novel detector conversion factor, (f_{conv}), that converts the X-ray photon to electron quantity to evaluate the total energy measured by the detector system.

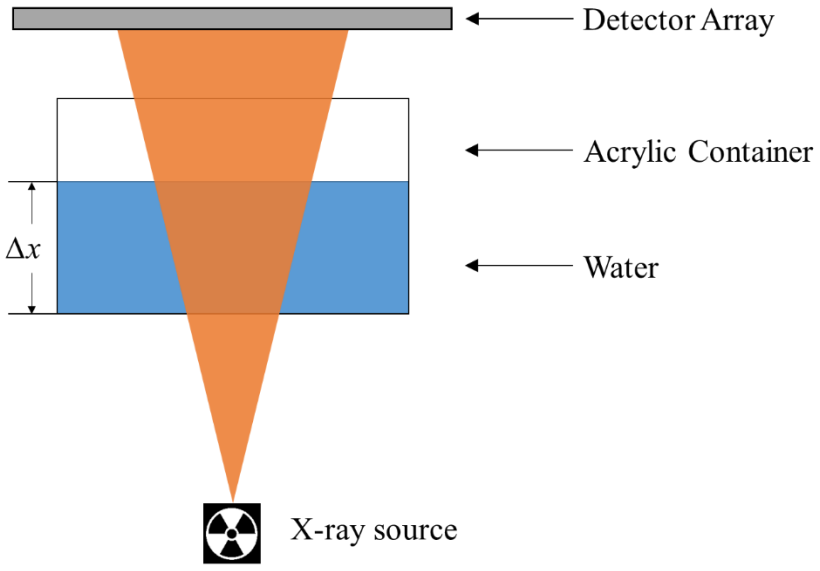

Figure 3-1: Schematic of the calibration test. The acrylic container is placed between the x-ray source and the detector array. Filtered water is injected with a syringe to achieve desired thickness. Then the x-ray system is turned on and the voltage level on the detector are recorded. The procedure is repeated with different water thickness ranging from 8 mm to 50 mm with 1 mm increment.

Recall in Chapter 2, the current study defined an X-ray measurement plane for the circular test section and X-ray line beam. Similarly, current study employed X-ray measurement plane as described in chapter 2 to construct measurement plane schematic for the acrylic container that is placed between the x-ray source and the detector array so that one can define X-ray beam transmission path to each pixel. From this measurement plan arrangement for the acrylic container, one can estimate voltage output displayed by each pixel using the Eq. (3.1). Now, the detector conversion factor can be obtained by the following procedures:

Step 1: The acrylic container is placed between the X-ray source and the detector array. Filtered water is injected with a syringe to achieve desired depth. Then the X-ray system is turned on and the voltage level on the detector is recorded. The procedure is repeated with different water depth ranging from 8 mm to 50 mm with 1 mm increment. Now one has various voltage recordings of different water depths that ranges from 8mm to 50 mm. Here, denotes recorded voltage output, $V_{pixel\text{-}RCRD}$, as a function of water thickness:

$$V_{pixel-RCRD} = V_{pixel-RCRD}(mm) \tag{3.2}$$

Step 2: Equating equations Eq. (3.1) and Eq. (3.2), one can estimate that the predicted voltage output should be approximately equal or isomorphic to the recorded voltage with different water depth ranging from 8 mm to 50 mm:

$$V_{pixel-RCRD} \approx \frac{A_{pixel} \cdot \Delta t \cdot mA}{6.242 \times 10^{18} C_f} \int_0^{e_{\max}} I(e) \cdot f_{conv}(e)\, de \tag{3.3}$$

Step 3: Conduct polynomial regression analysis for the detector conversion factor models of varying degrees (linear, quadratic, and cubic).

Step 4: Calculate absolute voltage and the relative percentage difference between predicted voltage and recorded voltage values of three optimized polynomial regression models. Lastly, select the detector conversion polynomial model that provides the smallest variance between predicted

voltage and recorded voltage readings. From this optimization process, current study attained a second-order polynomial model of best-fit detector conversion factor function that demonstrated outstanding results:

$$f_{conv}(e) = A_{coeff} \cdot e^2 + B_{coeff} \cdot e + C_{coeff} \tag{3.4}$$

where,

e = primary photon energy [keV]

A_{coeff} = 2nd degree coefficient term

B_{coeff} = 1st degree coefficient term

C_{coeff} = constant term

3.1.1 Detector Conversion Factor (f_{con})

Current work attained an optimized second-order polynomial, detector conversion factor function that will be utilized to calibrate predicted and measured voltage to each pixel location in this experiment. A sample result of a pipe center pixel location is provided in Figure 3-2; as one can observe, the predicted voltage demonstrated outstanding agreement from the optimized detector conversion factor for various water depth in the acrylic container ranging from 8 mm to 50 mm with 1 mm increment.

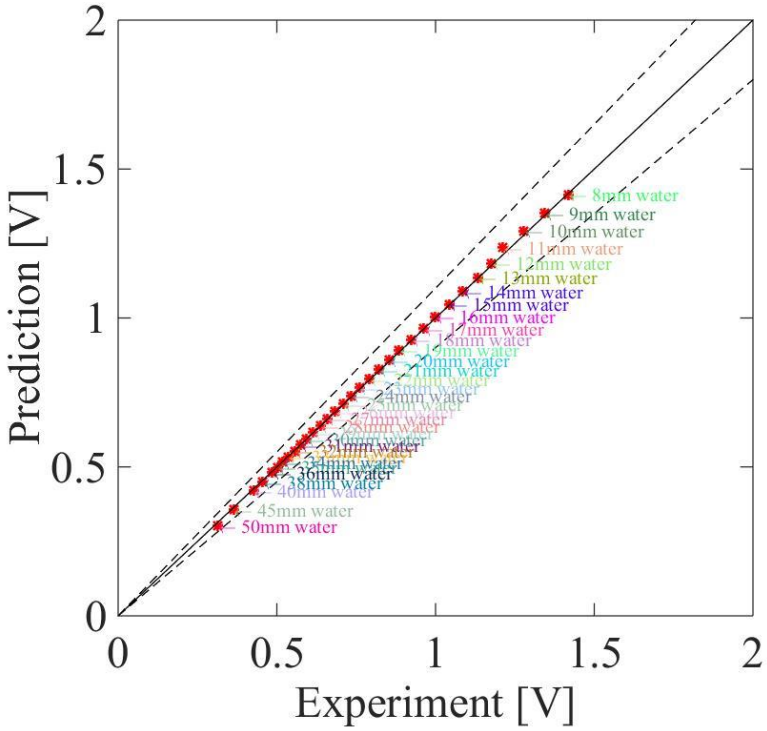

Figure 3-2: Comparison between voltage output based on actual measured value versus the predicted voltage output that was driven by optimized detector conversion factor approximated by the second order polynomial. Comparison data includes various water thickness ranging from 8 mm to 50 mm with 1 mm increment of the center pixel location.

Optimization results of each effective pixel detector conversion factor curves show similar coefficient terms of second-order polynomial function (refer to Figure 3.3). In particular, the detector conversion factor function of a center pixel is given below:

$$f_{conv}(e) = 1.7e^2 + 2e + 50 \tag{3.5}$$

Note, each pixel has its unique detector conversion factor based on optimization process. Therefore, each pixel uses designated optimized calibration data for the predicted voltage calculation to compare predicted and recorded voltage output values. Using optimized detector conversion factor, predicted voltage shows an outstanding agreement with recorded voltage output

from the calibration experiment with a mean absolute percentage error (MAPE) within ±2.5% and mean absolute voltage error (MAVE) within ±0.02V (refer to the Figure 3.3).

Lastly, an acrylic medium calibration experiment was also conducted with an acrylic plate of varying thickness ranging from 8.33mm to 46.33mm with 4.16mm increment using optimized detector conversion factor obtained from the water calibration experiment.

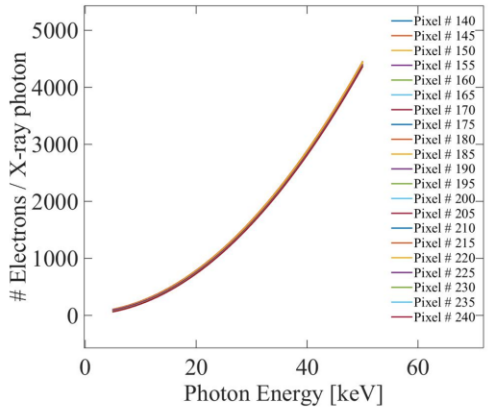

(a) # of electron per x-ray photon conversion for each pixel

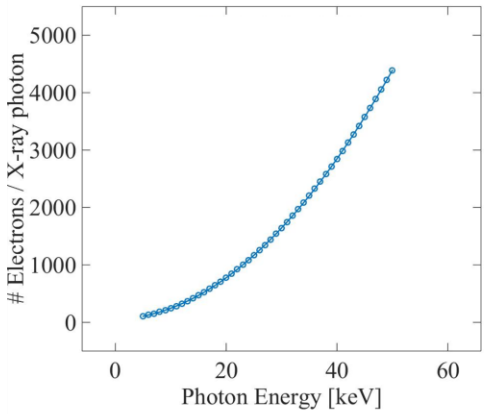

(b) Mean # of electron per x-ray photon conversion

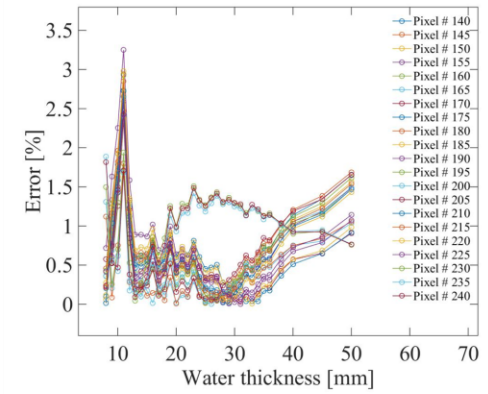

(c) Absolute percent error for all pixels

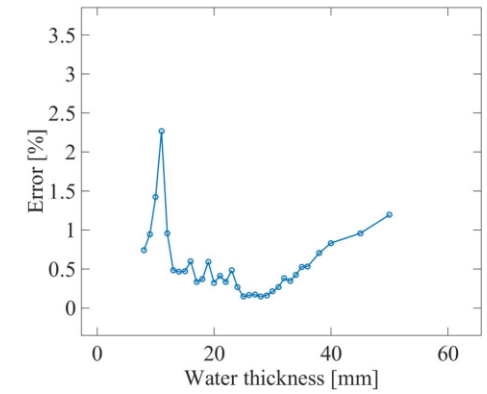

(d) Mean absolute percent error

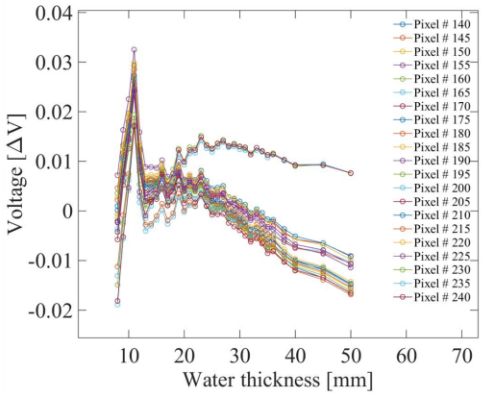

(e) Absolute voltage error for all pixels

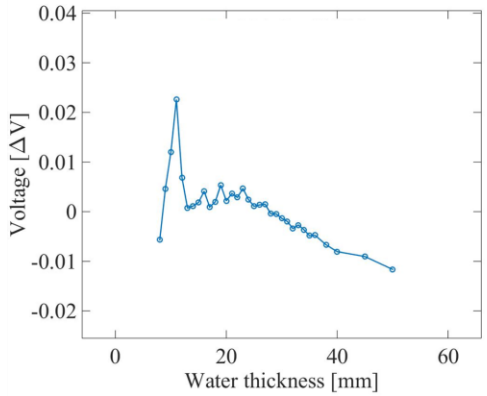

(f) Mean absolute voltage error

Figure 3-3: Detector conversion factor is approximated by a second order polynomial after optimization process. (a) and (b) illustrate a number of electrons generated per X-ray Photon, and MDCF is a provided-average coefficient value from all effective pixels. (c) and (d) are showing absolute percent error and showing MAPE within ±2.5%. (e) and (f) indicate absolute voltage error for all effective pixel range and showing MAVE within ± 0.02V.

3.1.2 Void Fraction Optimization/Correction:

Recall, a quantitative measurement of void fraction estimation (Eq. (2.27) in chapter 2) is utilized by many researchers for two-phase flow analysis. However, such quantitative estimation model must be analyzed further to validate its void fraction estimation capacity. From the calibration experiment (section 3.1), true void fraction value as a function of voltage output is attained at each given parameter measures. Figure 3.4(a) illustrates the comparison between true void fraction and quantitative measure of the void fraction estimation where the log model is quantitative estimation method (plotted in red) and true void fraction (plotted in blue). Also, Figure 3.3 indicates that log-model of quantitative estimation has a tendency to estimate less void fraction than a true void fraction. Because of this under-estimation tendency of quantitative estimation method, void fraction correction must be performed on all flow effective pixels for the two-phase flow measurement.

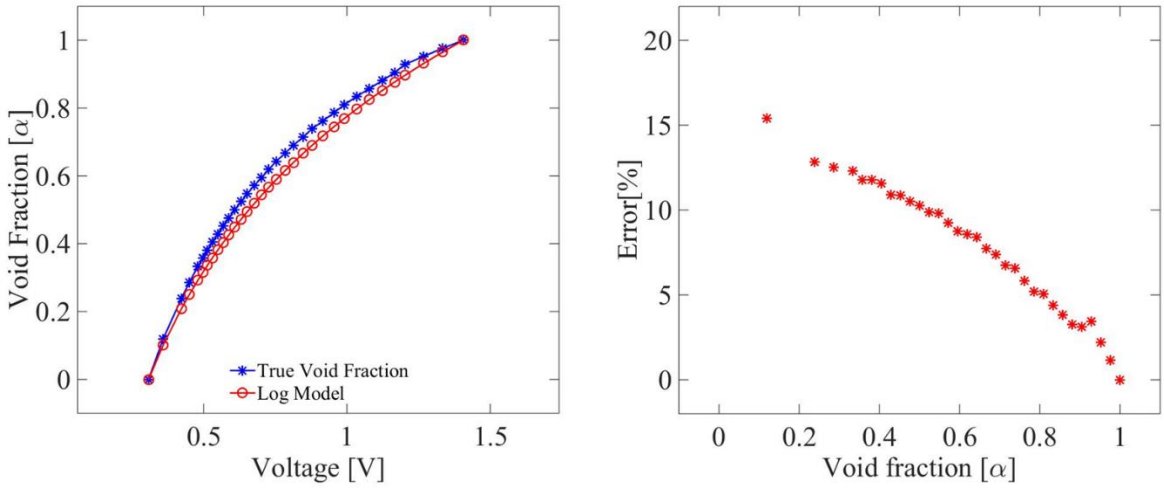

(a) (b)

Figure 3-4: (a) Comparison between true void fraction obtained from calibration experiment and estimated void fraction (log-model) using quantitative estimation method. (b) Overall percent error from log model for void fraction estimation.

Void fraction correction of two-phase flow in the circular test section are achieved in following procedures:

Step1: First, perform prediction voltage output (similar to the calibration experiment) for the circular test section that is filled with single–phase water (void fraction at 0) and single–phase air (void fraction at 1) using optimized detector conversion factor obtained in Section 3.1. In Figure 3-5(a), predicted voltage output shows reasonable agreement with experiment result. From the model prediction, one obtained minimum and maximum voltage information at each pixel location that indicates void fraction at 0 (test section full with water only: min voltage) and a void fraction at 1 (test section full with air only: max voltage).

Step2: Perform additional model prediction at each pixel location to obtain simulated void fraction output as a function of voltage that ranges between single-phase water generates min voltage response (void at 0) and single-phase air generates max voltage response (void at 1) using optimized detector conversion factor. Figure 3-5(b) shows void fraction distribution as a function of the voltage at each pixel location.

Step3: Record the voltage output information at each pixel location in the two-phase flow measurement. Finally, employ spline interpolation method to approximate corresponding void fraction at each pixel location to construct void fraction estimations.

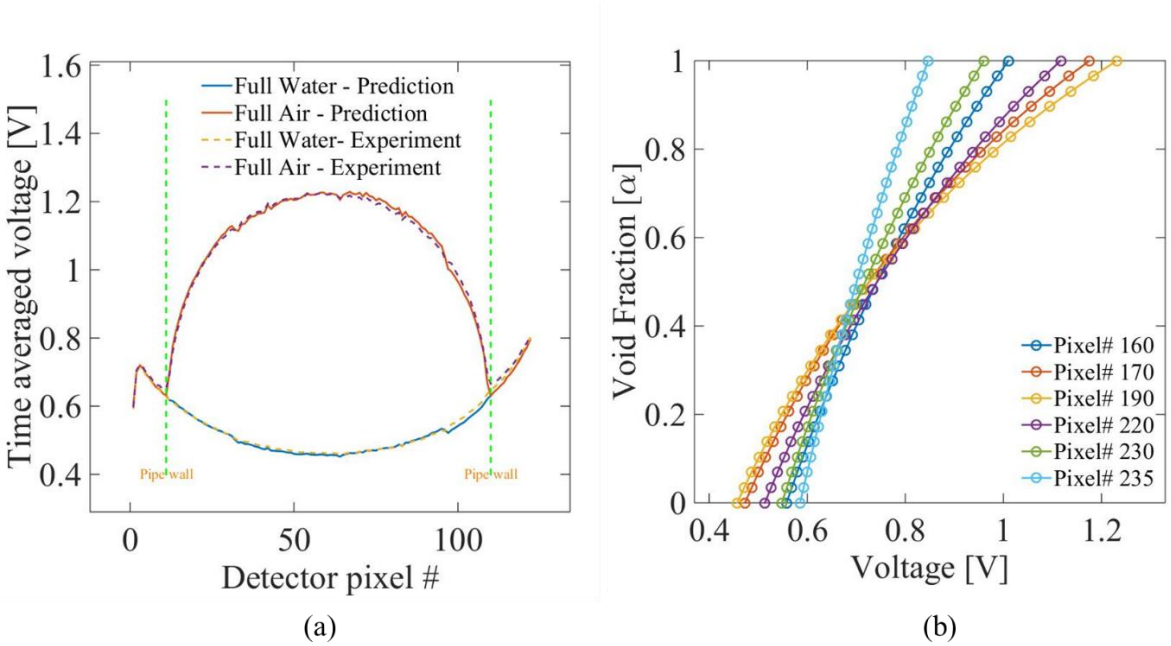

Figure 3-5: (a) Graph shows a comparison between model prediction and experimental result for the circular test section, model prediction for the circular test section that is fill with single–phase water (void fraction at 0) and single–phase air (void fraction at 1) using optimized detector conversion factor. (b) Void fraction distribution in function of voltage for the flow effective pixel locations that were driven from the model prediction using optimized detector conversion factor: 5 sample results are displayed in the figure.

3.2 Spatial Resolution and Scattering Effect

3.2.1 Focal Spot Blur

The focal spot blur, penumbra, is caused by a finite size of the source of the X-ray photons. The effect of the finite focal spot's size is most easily visualized by looking at the image of an edge of a thin object as shown in Figure 3-6. The edge blur is determined by the size of the focal spot, profile of the beam emerging from the focal spot, together with source-to-object and object-to-detector distance. The smaller the focal spot or magnification, SOD/(SOD+ODD), the smaller the blur.

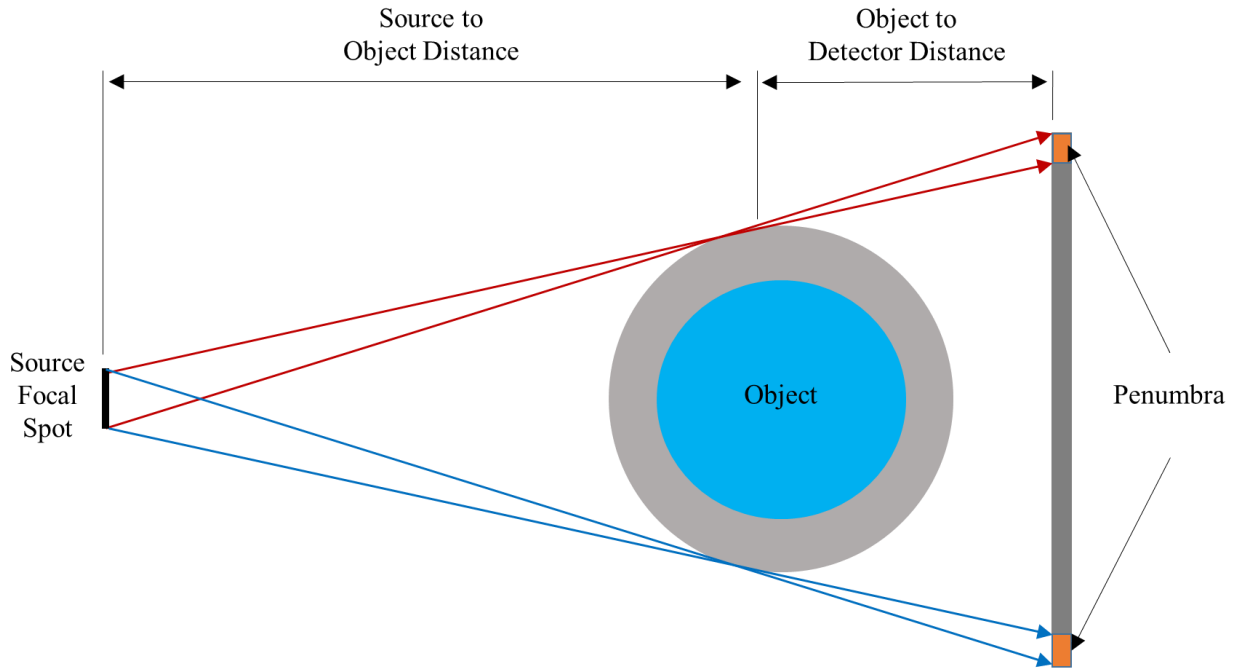

Figure 3-6: Penumbra (focal spot blur) with the source focal spot size

3.2.2 Scattering Effect

Scattering can be due to elastic (coherent) Rayleigh scatter, which is more likely off higher atomic number materials and at lower X-ray energies, or due to inelastic (incoherent) Compton scatter, which is dominant at higher energies. At over 1.02 MeV, there could also be pair production, but X-ray source used in the current study limited the photon energies to below 50 keV, hence this will not affect the result of current study's experiment. In the current study, the scattering effect form the lead enclosure is neglected because of the photoelectric effect is dominant. Scattering effects are typically less dominant in the energy below 50 keV.

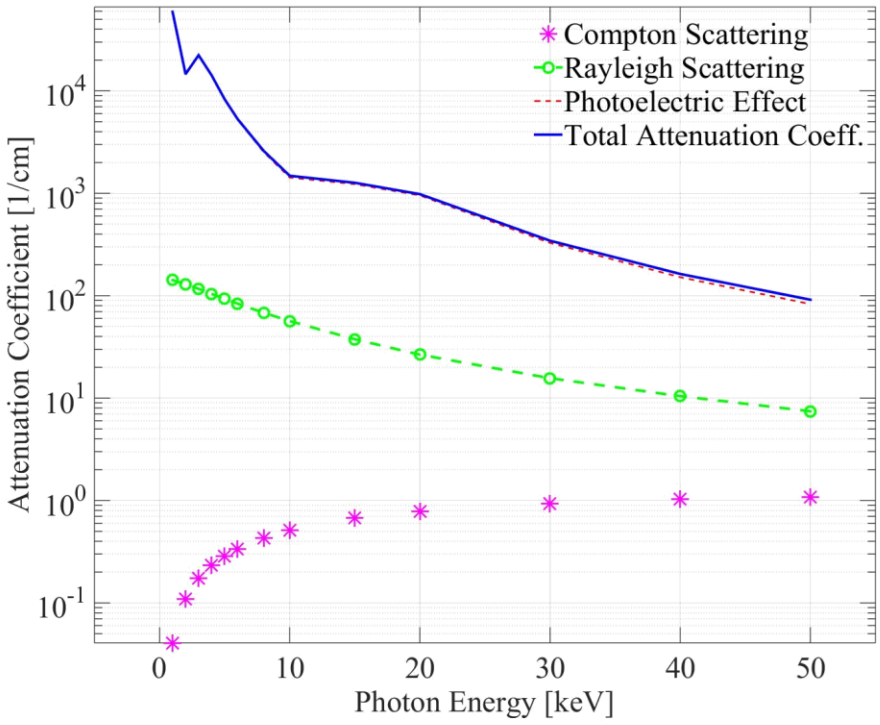

Figure 3-7: Total attenuation coefficient (solid blue line) for the lead. The contributions of principal photon-matter interactions are displayed as dashed curve (plotted in red) for the photoelectric effect and as the dotted plot for the Compton scattering. The Rayleigh scattering effect is displayed as dotted/dashed curve. Data from National Institute of Standards and Technology (NIST) [38,40]

The scattering effect of the lead-enclosure system is performed as shown in Figure 3-8. An incident X-ray beam penetrates through a thin lead ingot that is placed directly on the circular pipe. Then, the voltage level of the detector pixels is recorded and analyzed. The ingot absorbs incoming X-ray beam and at the same time, some portions of incident beam is also scattered. If a scattering effect from the lead-enclosure system is significant, the scattered photons should be detected by the detector pixel during the exposure time. The Figure 3-8(b) shows a voltage reading of the detector pixels. In particular, the voltage reading of the region covered by the ingot is ≈0.01V which is less than 1% of the total photoelectric effect when compared to the unblocked

signal. Hence, we can disregard the scattering effect from the lead-enclosure because photoelectric effect is predominant.

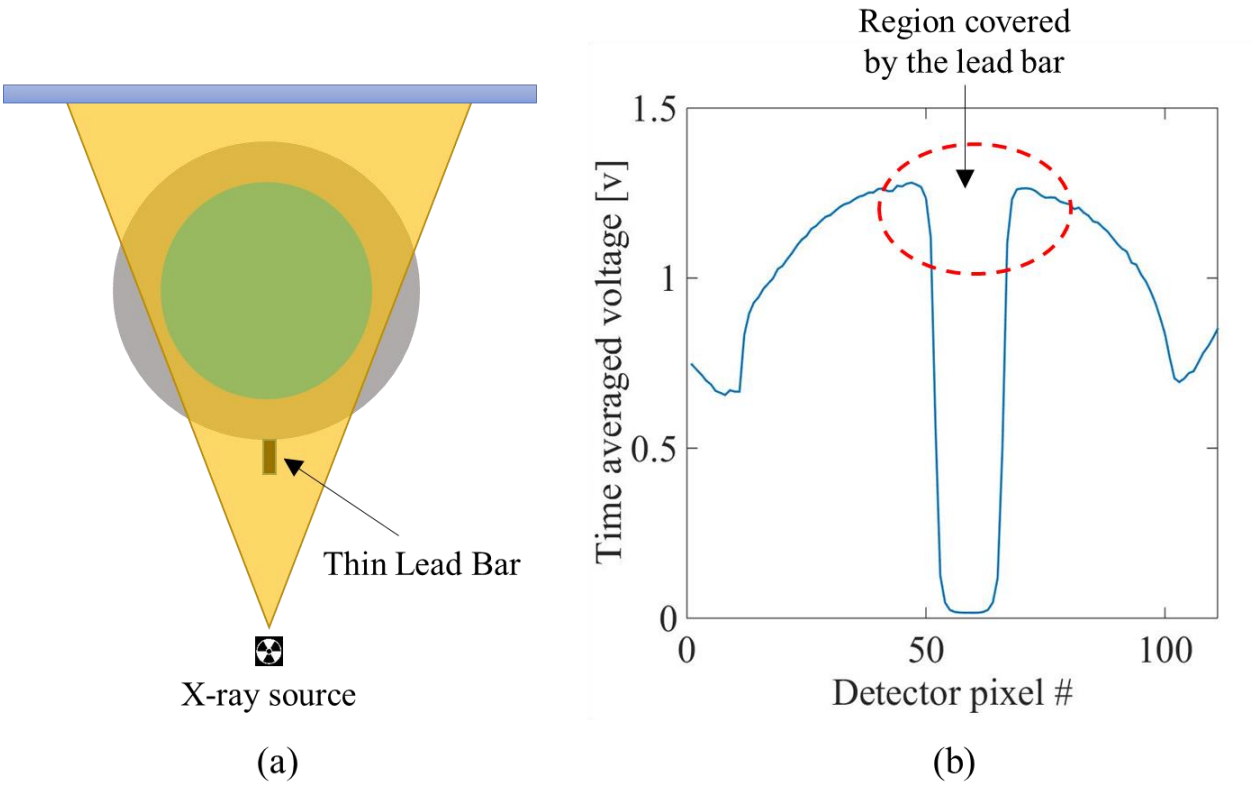

Figure 3-8: Scattering effect from the system lead enclosure.

3.3 Experimental Facility

The two-phase experiment is performed on a 2.54cm inner diameter circular test-section that is designed to run adiabatic air-water two-phase up-flows at room temperature near the atmospheric pressure conditions. The test loop consists of a two-phase mixing unit, circular test section, water storage tank, and air and water distribution systems, refer to figure 3.6 for illustration. The test section is made of poly-methyl methacrylate (PMMA), commonly known as transparent acrylic, with a flow domain dimension of cross-sectional outer diameter of 3.81cm (in x, and y direction), inner diameter of 2.54cm (in x, and y direction), wall thickness of 0.635cm, and the

overall height around 3m (in z direction). The volumetric influx of air flow was measured by three different precision gas-flow meter with an accuracy of ±1.0% of the full scale reading to cover various flow rates of interest.

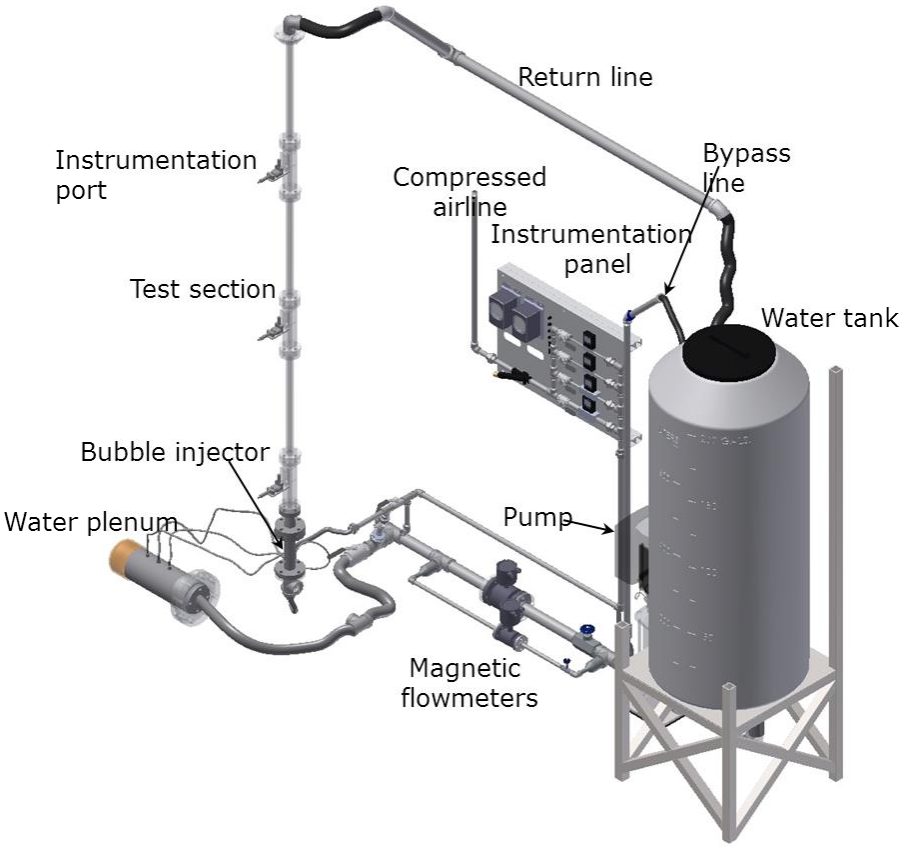

Figure 3-9: Overall schematic of the circular two-phase flow loop. Flow loop consists of a two-phase mixing unit, circular test section, water storage tank, and air and water distribution systems. Circular test section has 2.54cm inner diameter, 3m in height.

3.2.1 Flow Measurement System: X-ray Source and Detector System Arrangement

The SETXvue X-Ray Mass Flowmeter, flow measurement system, is designed and manufactured by the En'Urga Inc. X-Ray Mass Flowmeter is a versatile flow measurement tool that can be used to characterize flow parameters for two-phase flows. This flow measurement system consists of an X-ray tube, linear photodiode arrays, and graphical user interface (GUI) that

enables the user to control the settings of the x-ray tube, the linear detector array, and collect and analyze data to determine two-phase flow parameter.

The Oxford Jupiter 5000-93089, the X-ray source, and detector, was cautiously chosen to provide the necessary photon energy to achieve time-resolved measurement; the X-ray source provides between 10-50kV tungsten anode tube operating up to 1mA for radiography, non-destructive testing, and x-ray fluorescence (XRF). Such X-ray output levels provide sufficiently high photon flux needed both in the number and energy of photons that will pass through the two-phase flow structure. But, at the same time provide low enough that attenuation takes place over 25cm distance to show an adequate contrast to illustrate sufficiently different void fraction. The X-ray source had a focal spot size of 50μm with a maximum operating voltage of 50kV which would provide suitable photon energies for commercial detector system. The XB8801R and XB8804R are two available photodetector arrays, where each system provides different resolution mode (both manufactured by X-Scan Imaging Corporation). Figures 3.7, 3,8, and 3.9 provide an essential system component schematics and illustrates system component in detail.

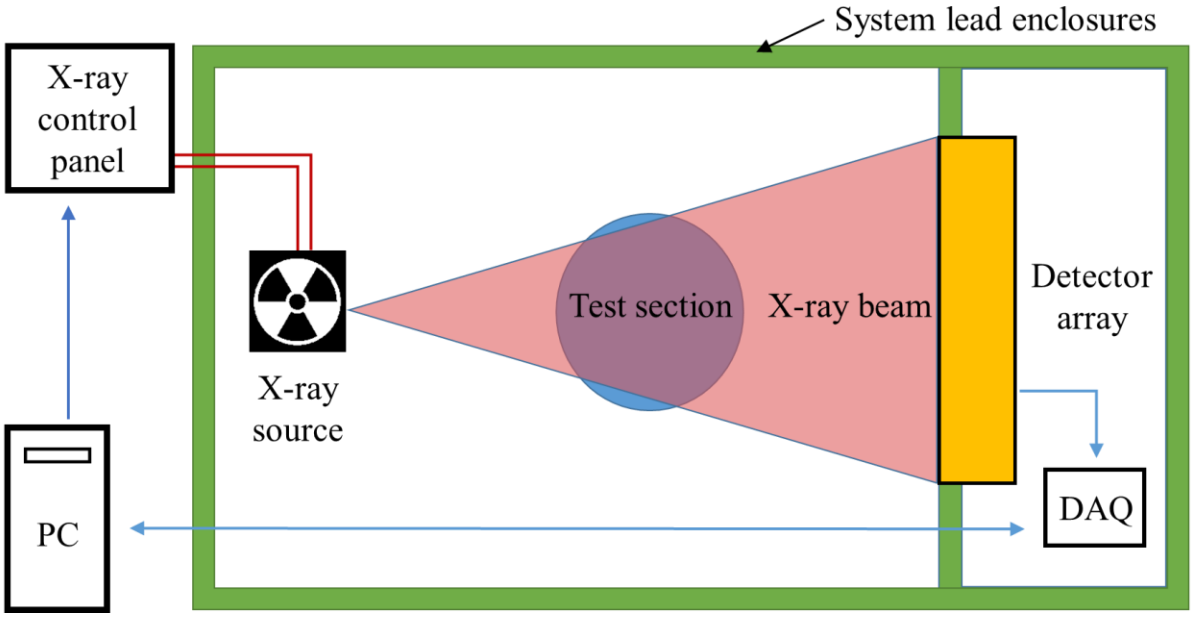

Figure 3-10: Schematic of the flow measurement system's key components. The x-ray control panel is controlled by graphical user interface (GUI) of the computer, set the x-ray tube's current, operating voltage and duration of radiation exposure. The software running on the computer is

used to set detector settings, which includes resolution mode, sensitivity mode, frame rate, exposure time.

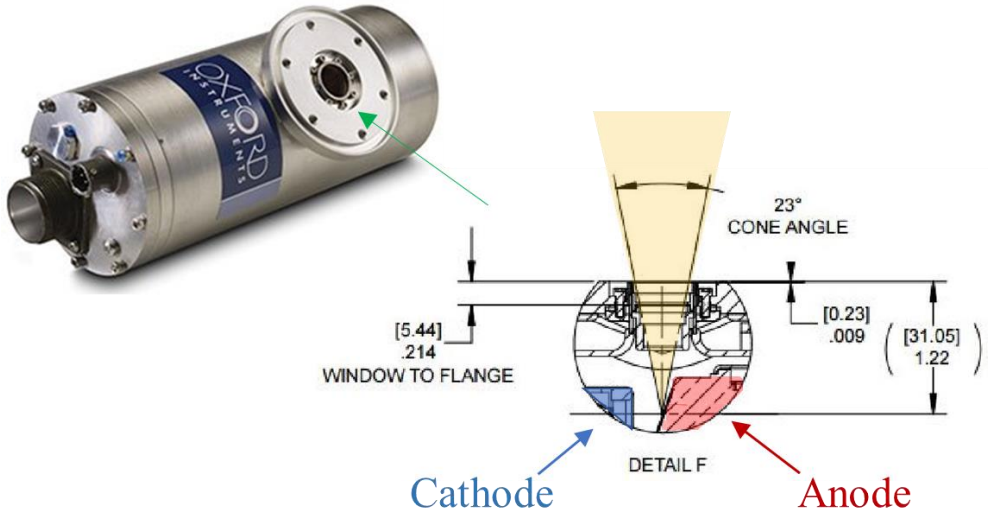

Figure 3-11: Photograph and a diagram of a tungsten anode x-ray tube, Oxford Jupiter 5000-93089. Image from the Jupiter 5000-93089 data specification sheet by Oxford Instrument. The cathode is colored in blue and the anode is colored in red, to make it easier to identify between two. In order to produce x-rays, high-speed electrical potential electrons are fired at the cathode and then accelerated to the focal spot on the tungsten anode, by up to a 50kV.

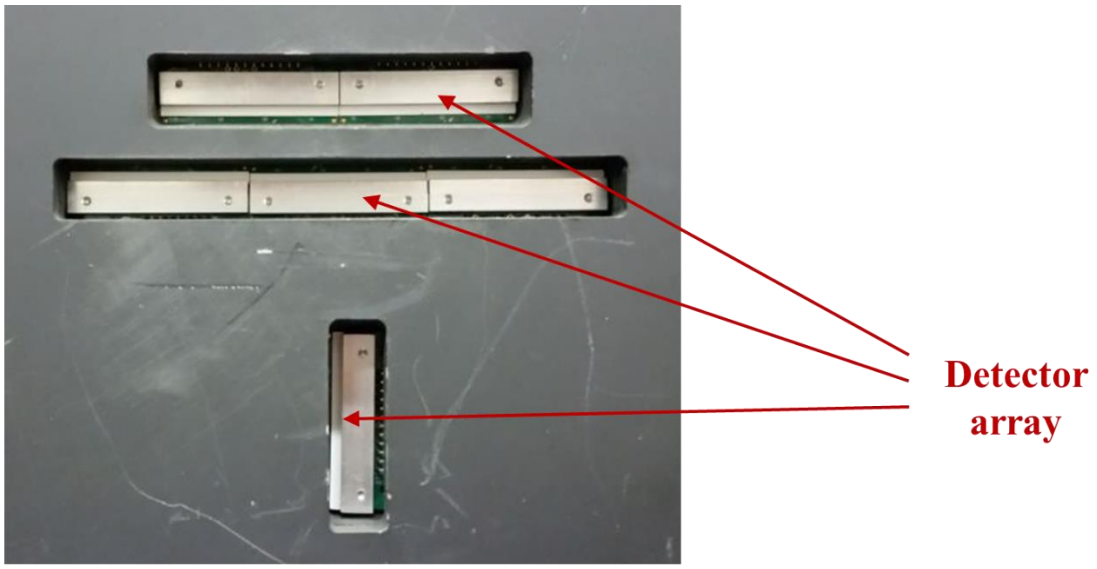

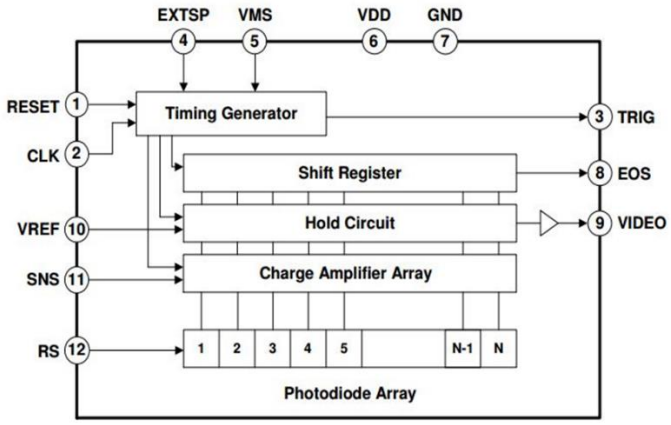

1	RESET	Reset Pulse
2	CLK	Clock Pulse
3	TRIG	Trigger Pulse
4	EXTSP	External Start Pulse
5	VMS	Master/Slave Selectio Voltage
6	VDD	Supply Voltage
7	GNS	Ground
8	EOS	End of Scan
9	VIDEO	Video Ouptut
10	VRE8	Reference Voltage
11	SNS	Sensitivity Selection
12	RS	Resolution Selection

Figure 3-12: Photograph and block diagram showing the main components of a photodiode detector XB8801R and the XB8804R linear detector array. The diagram is revision version 1.0 on X-Scan Imaging Inc.'s web page (https://xscanimaging.files.wordpress.com/2015/01/xb8801r-data-sheet-rev1_0.pdf).

4. RESULTS AND DISCUSSION

In this chapter, two-phase flow (bubbly and slug flow) experiment is conducted to obtain time-averaged void fraction data via a spectral model that measures the voltage responses of each individual pixel location. The void fraction uncertainty in each flow test is also analyzed and discussed. The cross-correlation between two detector signal is used for the gas velocity measurements. Lastly, the conversion algorithm is constructed to configure the pixel distribution to the radial distribution profile. The radial profiles are compared to the double-sensor probe experiment data. Superficial gas velocity from the both flow tests is compared to the gas flow meter recording. For an addition reference, the drift-flux model (drift velocity correlation) is introduced for describing the two-phase flow in the small pipe.

4.1 Water Calibration Experiment Results

Voltage responses in each detector pixels are recorded in accordance with the following procedures. First, the acrylic container is placed between the X-ray source and the detector array. Next, a filtered water is injected through a syringe to achieve desired thickness. Then the X-ray system is turned on and the voltage level of the detector pixels are recorded. The procedure is repeated with different water thickness that ranges from 8 mm to 50 mm with 1 mm increment. Lastly, the prediction voltage is simulated using the spectral model.

Recall, the voltage output displayed by each detector pixels are given by:

$$V_{pixel} = \frac{A_{pixel} \cdot \Delta t \cdot mA}{6.242 \times 10^{18} C_f} \int_0^{e_{\max}} I(e) \cdot f_{conv}(e)\ de \tag{4.1}$$

The optimized detector conversion factor that is approximated by a second order polynomial from the optimized process:

$$f_{conv}(e) = 1.7e^2 + 2e + 50 \tag{4.2}$$

The experimental data and prediction voltage are shown in Figure 4-1. Note, the prediction result demonstrates high precision and consistency with the measured voltage distribution.

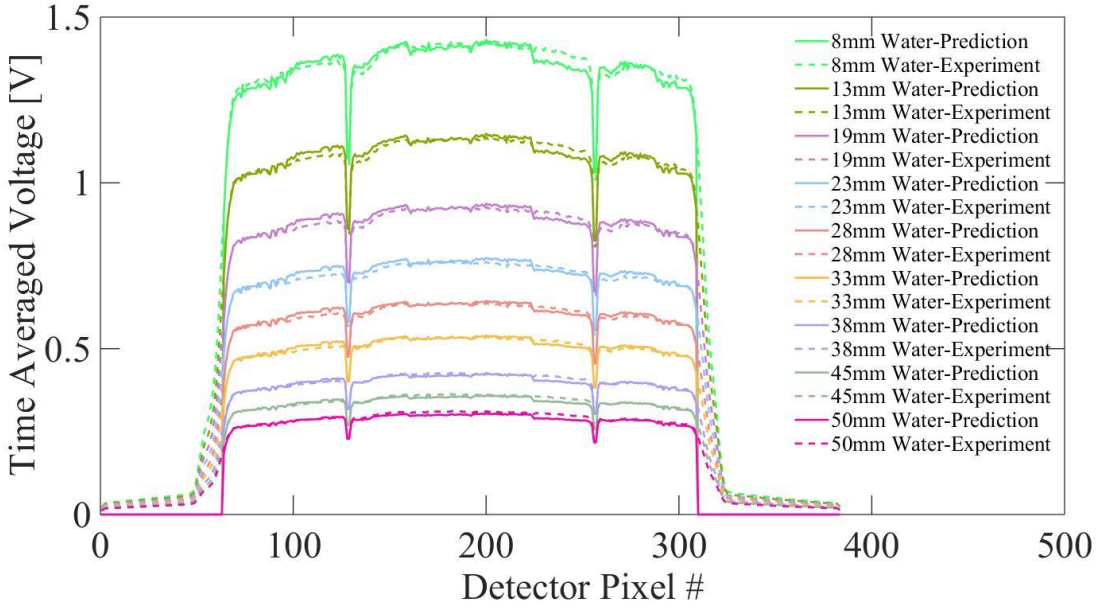

Figure 4-1: Comparison between the measured voltage and the predicted voltage output at each detector pixels. The time-averaged voltage responses are measured for water thickness that ranges from 8mm to 50mm. The solid lines represent the predicted voltage distribution and the dash lines are measured voltage value recorded by each detector pixels.

4.1.2 Acrylic Plate Results

Acrylic plate voltage responses in the detector pixels are recorded in accordance with the following procedures. First, the acrylic plate is placed directly on top of the detector array.

Then the X-ray system is turned on and the voltage level of the detector pixels are recorded. The procedure is repeated with different acrylic plate thickness ranging from 8.33 mm to 46.33 mm with approximately 4.5 mm increment in each sample test. Prediction voltage is simulated using the spectral model as described in Eq. (4.1) and Eq. (4.2). Comparisons between the prediction model and the experiment data are shown in Figure 4-2.

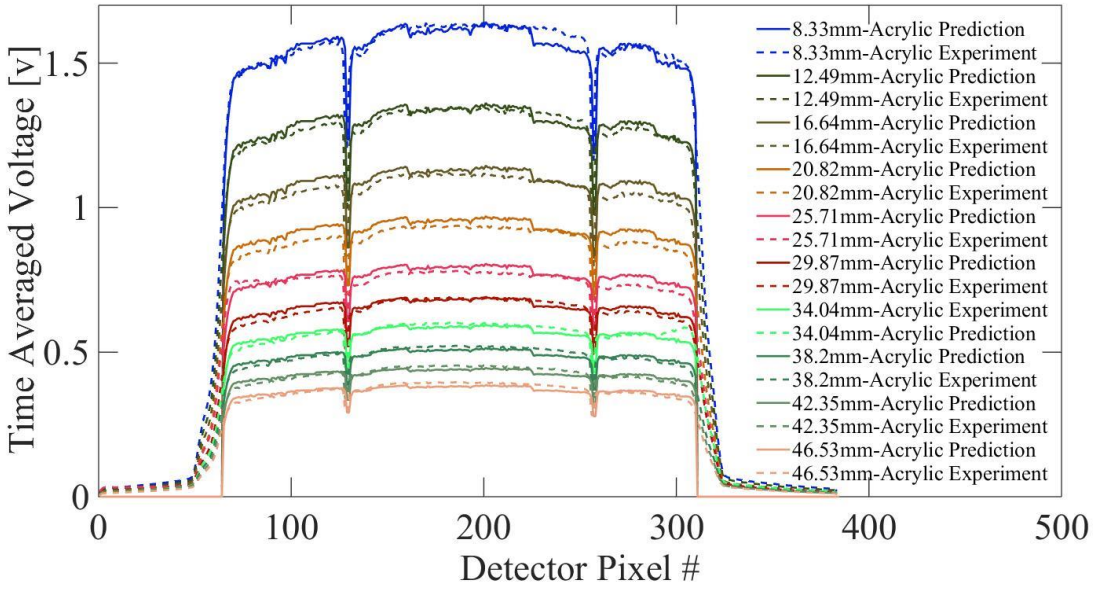

Figure 4-2: Comparison between the measured voltage versus the predicted voltage at each detector pixels. Acrylic plate thickness range from 8.33mm to 46.53mm; the solid lines are predicted voltage; and dash lines are measured voltage value recorded by each detector pixels.

4.1.3 Circular Test Section Results

Voltage responses in the detector pixels for the circular test section are recorded using following procedures. First, circular test section is placed between the X-ray source and the detector array. Then the X-ray system is turned on and the voltage level of the detector pixels are recorded. The procedure is repeated for the test section fill with single-phase water (void at 0) and single-phase air (void at 1) only. The prediction voltage is simulated using the spectral

model using the Eq. (4.1) and Eq. (4.2). Time-averaged voltage response of a circular test section that is filled with single-phase water and the single-phase air are illustrated in Figure 4-3. The prediction voltage distribution for the circular test section in the detector pixel shows outstanding agreement to the measured voltage with a percent error of 5% and the absolute voltage differences in the detector pixels to be within ±0.02 volt.

(a)

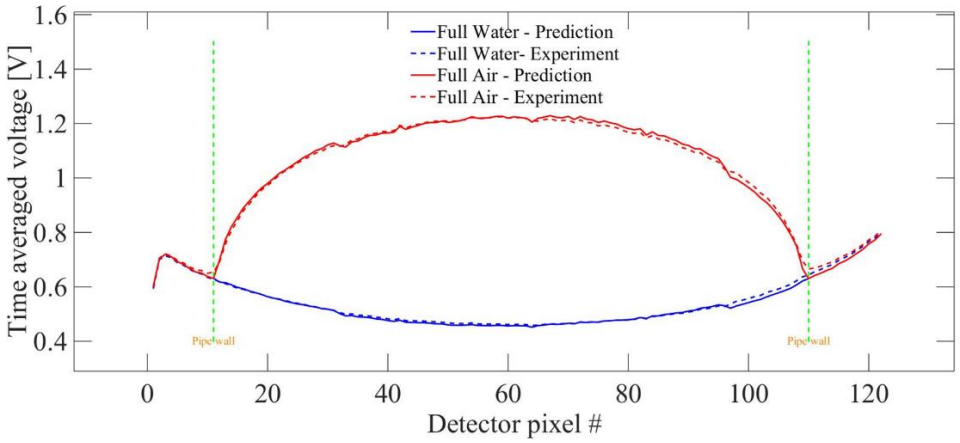

(b)

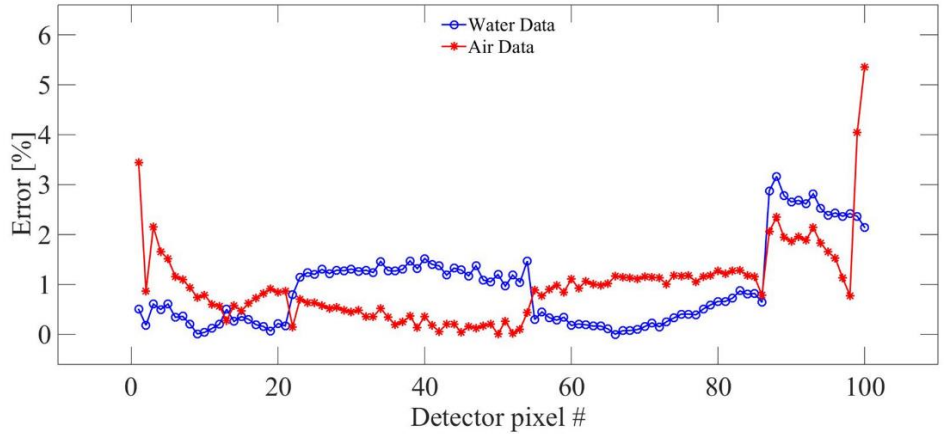

(c)

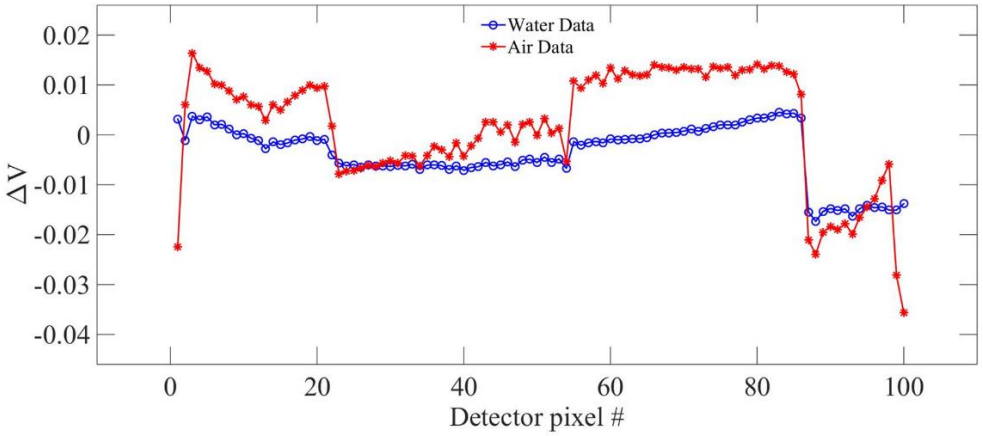

Figure 4-3: (a) Comparison between the prediction voltage versus measured voltage in the detector pixel: solid lines are prediction voltage and dash lines are measured voltage distribution in the pixel. (b) Percent error between prediction and measured voltage. (c) The absolute voltage difference between prediction and measured voltage distribution in the detector pixel.

.

The result from the water, acrylic, and combination of two media in the circular test section shows that the detector conversion factor yields a great prediction for all three experiments. However, the beam hardening effect is substantial and significant for different water and the acrylic plate thickness that is as small as few millimeters thick.

4.2 Void Fraction Result

Two-phase flow experiment is performed under two different flow regimes: bubbly and slug flow in the vertical flow setting. The detailed experimental conditions are listed in Table 3. Note, two-phase flow experiment in different flow regimes are repeated twice to ensure validity and verifiability of the experimental condition.

Table 3: Flow Condition for bubbly and slug flow regime

	Bubble 1	Bubble 2	Slug1	Slug2
j_g *(m/s)*	0.14	0.1401	0.2626	0.2636
j_f *(m/s)*	0.6931	0.6891	0.5232	0.5252

The time-resolved measurement for each flow regime is recorded in the order of 1000 frames per second with a total sampling time of 60 seconds. Note that line-averaged void fraction information is measured by each pixel and then individual readings of each detector pixel are combined to provide void fraction profile in the circular pipe. Void fraction information in each pixel is expressed in grayscale between 0 (full water) and 1 (full air). This combined time series void fraction profile is then used to generate 2-D flow image. Figure 4-4 shows 2D reconstructed flow image of the bubbly and slug flow with experimental conditions listed in Table 3.

Figure 4-4: 2D reconstructed flow image from the bubbly flow (a) , (b) and the slug flow (c), (d).

4.2.1 Void Fraction Uncertainty

The main purpose of uncertainty calculation is to provide more accurate void fraction distribution of the circular pipe. Stated in more detailed terms, the reliability of the void fraction accuracy depends on identifying the uncertainty of each pixel measurements. For example, if

uncertainty is underestimated in each pixel measurement, pixel to the radial conversion process will yield void fraction estimation with compounded error. For this reason, it is essential to construct well-designed procedures to identify all sources of uncertainties for all pixel measurement, which includes uncertainties arising from any relevant voltage sampling by each pixel location. In addition, the analytical contribution of the uncertainty can be identified with uncertainty originating in the following procedure:

First, time-averaged voltage distribution is measured for the circular pipe filled with single phase water (void fraction at 0) and the single-phase air (void fraction at 1).

Second, calculate the absolute voltage difference between the circular pipe filled with the single-phase water and the single-phase air. Hence, one can obtain a voltage difference between circular test section fill with water and air in the detector pixel.

Third, calculate the standard deviation of time-series data in the single-phase water and the single-phase air.

Lastly, uncertainty in void fraction calculation in the flow effective pixels can be determined and estimated by the standard deviation of time series sample divided by absolute voltage difference in the detector pixel. Hence, the uncertainty in the void fraction measurement is expressed as:

$$Error = \frac{Std}{\Delta V} \tag{4.3}$$

where,

ΔV is the absolute voltage difference between circular test section fill with a single-phase water and single-phase air,

Std. is the standard deviation of water and air voltage samples in each pixel.

The void fraction uncertainty in the detector pixel is shown in Figure 4-5(c). Note, the pixels that are near the either ends of the pipe wall contribute up to 40% error in the void fraction measurement. Hence, to correct for the void fraction uncertainty, the voltage readings of approximately five pixels are removed from either end of the pipe wall and hence from the void

fraction curve. Now, assuming that the void fraction near the pipe wall is zero, interpolate the void fraction profile and distribution of the deleted region to reconstruct the void fraction curve.

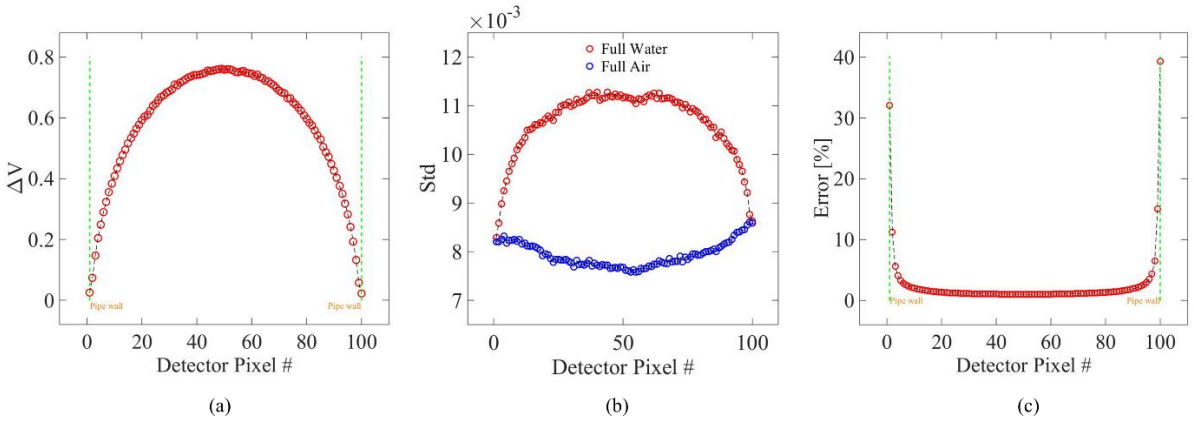

Figure 4-5: (a) absolute voltage difference between circular test section fill with single phase water and single phase air in each pixel locations in the flow domain. (b) the standard deviation of water (red) and air (blue) voltage data samples in each pixel location in the flow domain. (c) uncertainty contribution in void fraction calculation of each pixel location in the flow domain.

4.2.2 Void Fraction Profile

Time-averaged void fraction is calculated over the total sampling time. First, the instantaneous void fraction is calculated in each pixel then all void fraction measurements are averaged over the total sampling time in each pixel location. Void fraction distribution for each flow conditions are shown in Figure 4-6. Reconstructed void fraction profiles are provided in Figure 4-6(b) and Figure 4-7(d) for bubbly and slug flow, respectively.

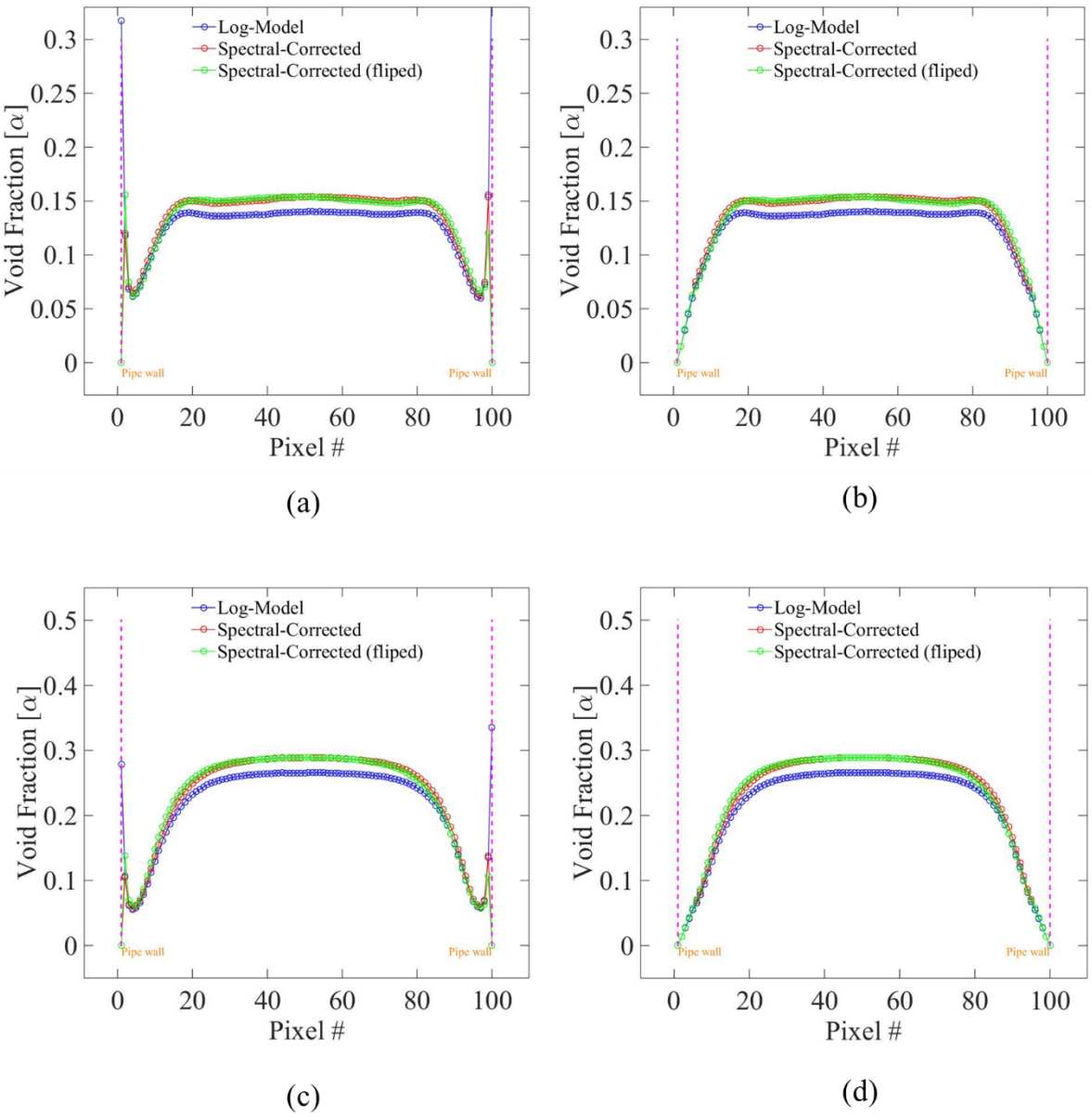

Figure 4-6: (a) and (c) are a direct result of the detector pixel measurement before the void fraction correction for bubbly and slug flow, respectively. (b) and (d) are corrected void fraction profile in the detector pixel for the bubbly flow and slug flow, respectively.

Void fraction distribution in the pixels does not represent the radial void fraction distribution. Because the flow in a circular pipe is axisymmetric, the conversion algorithm is used to reconstruct the void fraction distribution in the detector pixels to the radial profile in the

circular pipe. Recall, the conversion algorithm that converts the pixel distribution to the radial profile is given by:

$$\begin{bmatrix} \frac{A_{ring\#1}}{A_{pixel\#1}} & \frac{A_{ring\#2}}{A_{pixel\#1}} & \frac{A_{ring\#3}}{A_{pixel\#1}} & \cdots & \frac{A_{ring\#n\text{-}1}}{A_{pixel\#1}} & \frac{A_{sector(R_{\#n})}}{A_{pixel\#1}} \\ 0 & \frac{A_{ring\#2}}{A_{pixel\#2}} & \frac{A_{ring\#3}}{A_{pixel\#2}} & \cdots & \frac{A_{ring\#n\text{-}1}}{A_{pixel\#2}} & \frac{A_{sector(R_{\#n})}}{A_{pixel\#2}} \\ 0 & 0 & \frac{A_{ring\#3}}{A_{pixel\#3}} & \cdots & \frac{A_{ring\#n\text{-}1}}{A_{pixel\#3}} & \frac{A_{sector(R_{\#n})}}{A_{pixel\#3}} \\ \vdots & \vdots & \ddots & \cdots & \vdots & \vdots \\ 0 & 0 & 0 & \cdots & \frac{A_{ring\#n\text{-}1}}{A_{pixel\#n\text{-}1}} & \frac{A_{sector(R_{\#n})}}{A_{pixel\#n\text{-}1}} \\ 0 & 0 & 0 & \cdots & 0 & \frac{A_{sector(R_{\#n})}}{A_{pixel\#n}} \end{bmatrix} \times \begin{bmatrix} \alpha_{R(R_{\#1})} \\ \alpha_{R(R_{\#2})} \\ \alpha_{R(R_{\#3})} \\ \vdots \\ \alpha_{R(R_{\#n-1})} \\ \alpha_{R(R_{\#n})} \end{bmatrix} = \begin{bmatrix} \alpha_{pixel\#1} \\ \alpha_{pixel\#2} \\ \alpha_{pixel\#3} \\ \vdots \\ \alpha_{pixel\#n-1} \\ \alpha_{pixel\#n} \end{bmatrix} \quad (4.4)$$

Reduce the Eq. (4.4) matrix format, into:

$$A \cdot \alpha_R = \alpha_{pixel} \quad (4.5)$$

Multiply both sides with inverse area matrix A^{-1}:

$$\alpha_{Radial} = A^{-1} \cdot \alpha_{pixel} \quad (4.6)$$

With the results of Eq. (4.6), the radial void fraction in the circular pipe is provided.

In Figure 4-7, the radial profiles for the bubbly and slug flows are provided. The vertical axis is the time-averaged void fraction and the horizontal axis is the radius of the circular pipe measured from the center pipe to the inner pipe wall. Probe data is also provided in the Figure 4-7 along with X-ray measured data for the comparison between two measurement result.

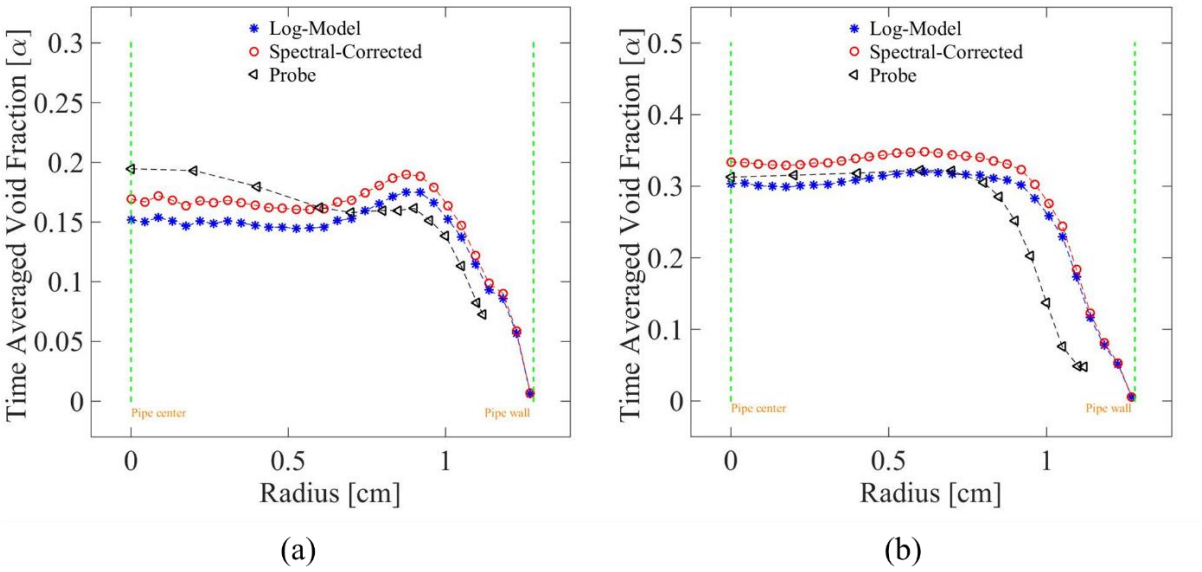

Figure 4-7: Radial void fraction profile for the bubbly flow (a) and slug flow (b). Radial distribution of spectral analysis based on void fraction estimation (red), quantitative measurement of void fraction estimation (blue), and X-ray probe data (black).

In the bubbly flow, X-ray measured data shows the distinct void fraction distribution pattern when compared with the probe. Probe data shows the void fraction peak at the center of the pipe where X-ray shows the void fraction peak near the wall. In the slug flow, both results showing similar void fraction trend but probe measurement indicates lower void fraction near the pipe wall.

4.3 Gas Velocity Result

Current study acquired the cross-correlation signal from the pair of upstream and the downstream X-ray detector arrangement. As shown in Figure 4-8, the voltage fluctuating signals from the upstream and downstream X-ray detectors shows great similarity for the air and the water signal patterns. The cross-correlation function can be described as:

$$R_{xy}(t) = \int_{-T}^{T} x(\tau) y(t-\tau)\, d\tau \tag{4.7}$$

The maximum value of $R_{xy}(t)$ occurs at $\tau=\tau^*$ when the correlation delay time τ is equal to the transit time τ^* of the measured parameter of two-phase flow between upstream and downstream. Therefore, a gas velocity of the two-phase flow is given by:

$$V_g = \frac{\Delta z}{n \cdot \tau^*} = \frac{\Delta z}{n \cdot \Delta t} = \frac{\Delta z}{n \cdot (N_s / f)} \tag{4.8}$$

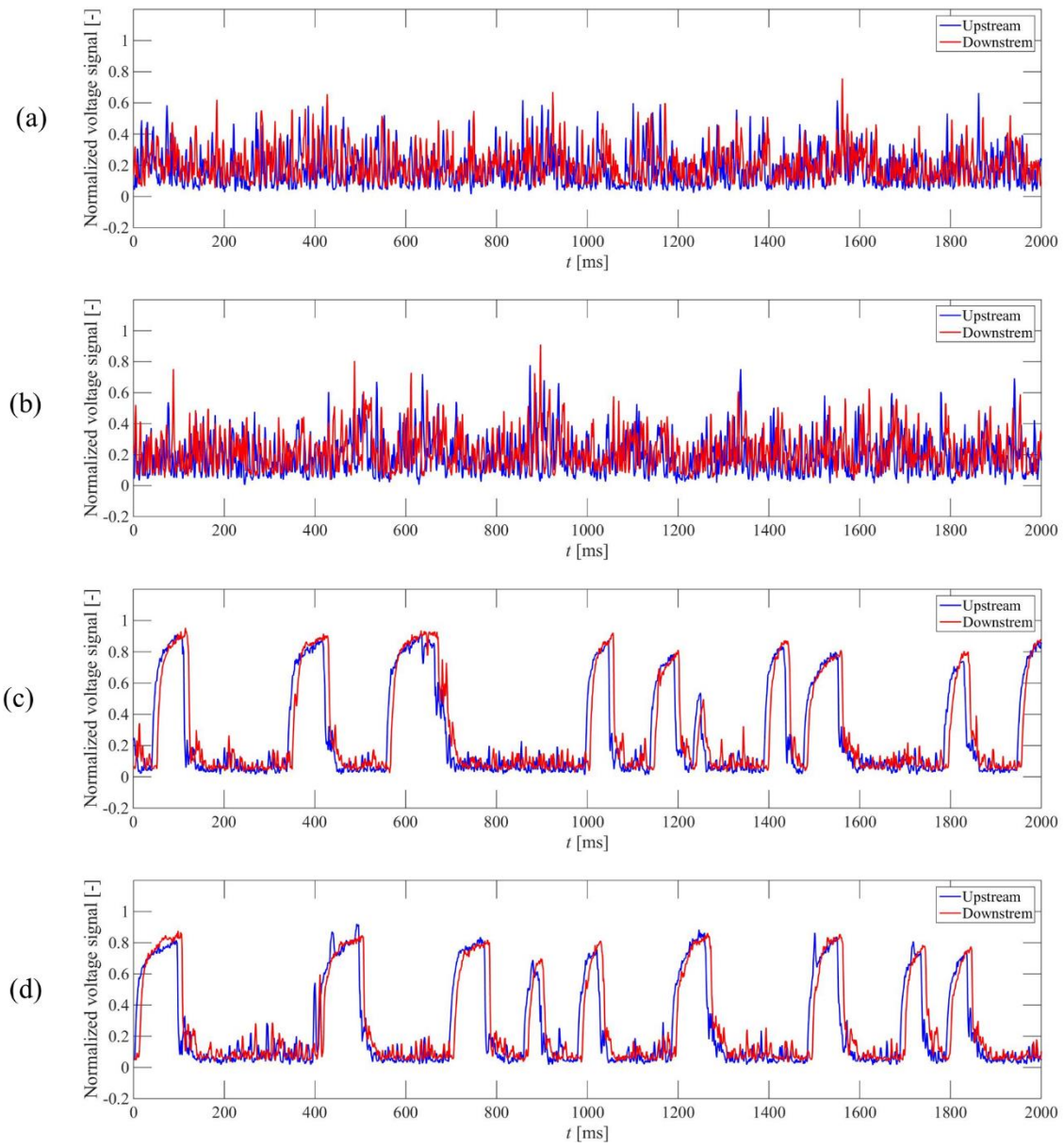

Figure 4-8: The X-ray voltage fluctuating signals from the two detector arrangement. (a) and (b) are bubbly flow voltage signal patterns, respectively, (c) and (d) are slug flow voltage signal patterns from the upstream and downstream X-ray detector arrangement.

4.3.1 Signal to Noise Ratio (SNR)

A variety of noises sources can contaminate the X-ray voltage signal in the gas velocity measurement. The signal-to-noise-ratio (SNR) strength governs the resulting X-ray signal cross-

correlation and ultimately the accuracy and uncertainty of the resulting gas velocity measurements. Hence, correlation SNR metrics calculated from the X-ray correlation measurement plane is used as a benchmark metrics to measure the relative magnitude and strength of correlation of the resulting uncertainty of an individual pixel flow data.

Figure 4-9 shows a one-dimensional graphical representation of SNR metric of sample X-ray correlation signals. In the current study, uncertainty quantification method based on the primary peak ratio (PPR) is utilized. PPR quantification is proposed by Charonko and Vlachos to calculate the uncertainty based on the PPR value of the correlation measurement [55]. The PPR is defined as the "ratio between the height of the primary peak and the height of the second tallest peak" and is given by [55]:

$$PPR = \frac{C_{\max}}{C_2} \tag{4.9}$$

where,

C_{max} is the primary peak height,

C_2 is the height of the secondary peak

PPR of each flow results are listed in Table 4

Table 4: Primary peak ratio for each flow correlation signal

	Bubble 1	Bubble 2	Slug1	Slug2
PPR	1.2675	1.2618	1.9722	2.0687

It is shown that PPR effectively measures the detectability of the primary peak. In Table 4, SNR using PPR for all four flow results are provided, primary peak signals appears to be strong in both flows, especially in the slog flows where PPR is around 2.

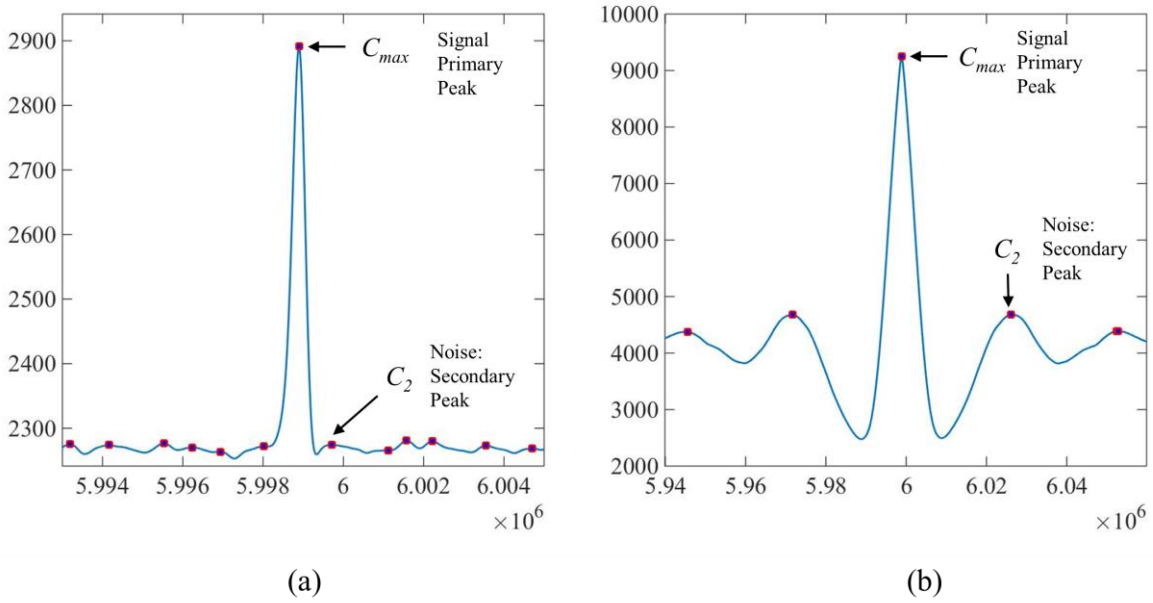

Figure 4-9: 1D graphical illustration of correlation SNR for PPR: bubbly flow correlation (a) and slug flow correlation signal (b).

4.3.2 Pixel to Radial Distribution

The measured gas velocity profiles are shown in Figure 4-10 for the bubbly and the slug flow measurements. The vertical- and horizontal-axis are the velocity and detector pixel location that measures the velocity for a specific location in the flow domain, respectively.

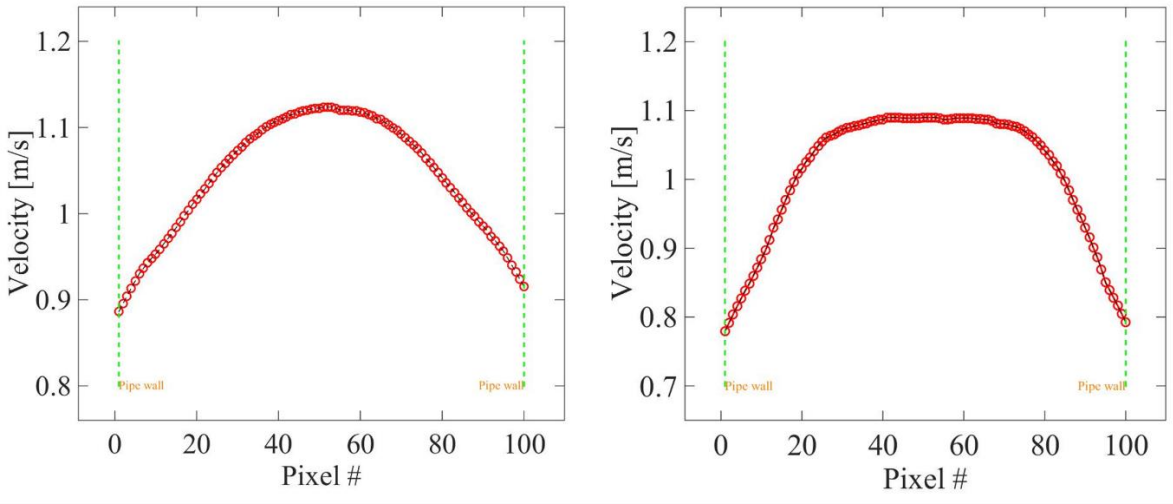

Figure 4-10: Gas velocity measured by each detector pixel: bubbly flow (a) and slug flow(b).

Note, the gas velocity distribution in the detector pixels does not represent the radial profile. Given that the gas flow in a circular pipe is axisymmetric, the conversion algorithm is used to restructure the gas velocity distribution in the detector pixels to the radial void profile. Recall, the conversion algorithm for the radial velocity profile yields:

$$\begin{bmatrix} \frac{A_{ring\#1}}{A_{pixel\#1}} & \frac{A_{ring\#2}}{A_{pixel\#1}} & \frac{A_{ring\#3}}{A_{pixel\#1}} & \cdots & \frac{A_{ring\#n-1}}{A_{pixel\#1}} & \frac{A_{sector(R_{\#n})}}{A_{pixel\#1}} \\ 0 & \frac{A_{ring\#2}}{A_{pixel\#2}} & \frac{A_{ring\#3}}{A_{pixel\#2}} & \cdots & \frac{A_{ring\#n-1}}{A_{pixel\#2}} & \frac{A_{sector(R_{\#n})}}{A_{pixel\#2}} \\ 0 & 0 & \frac{A_{ring\#3}}{A_{pixel\#3}} & \cdots & \frac{A_{ring\#n-1}}{A_{pixel\#3}} & \frac{A_{sector(R_{\#n})}}{A_{pixel\#3}} \\ \vdots & \vdots & \ddots & \cdots & \vdots & \vdots \\ 0 & 0 & 0 & \cdots & \frac{A_{ring\#n-1}}{A_{pixel\#n-1}} & \frac{A_{sector(R_{\#n})}}{A_{pixel\#n-1}} \\ 0 & 0 & 0 & \cdots & 0 & \frac{A_{sector(R_{\#n})}}{A_{pixel\#n}} \end{bmatrix} \times \begin{bmatrix} V_{R(R_{\#1})} \\ V_{R(R_{\#2})} \\ V_{R(R_{\#3})} \\ \vdots \\ V_{R(R_{\#n-1})} \\ V_{R(R_{\#n})} \end{bmatrix} = \begin{bmatrix} V_{pixel\#1} \\ V_{pixel\#2} \\ V_{pixel\#3} \\ \vdots \\ V_{pixel\#n-1} \\ V_{pixel\#n} \end{bmatrix} \quad (4.10)$$

Reduce the Eq. (4.10) matrix format, into:

$$A \cdot V_R = V_{pixel} \tag{4.11}$$

Multiply both sides with inverse area matrix A^{-1}:

$$V_{Radial} = A^{-1} \cdot V_{pixel} \tag{4.12}$$

With the results of Eq. (4.12), the radial velocity profile in the circular pipe is obtained. The radial profiles for the bubbly and the slug flows are illustrated in Figure 4-11. The vertical and the horizontal axis represent the velocity and the radius of the circular test section from the center of the pipe the inner pipe wall, respectively.

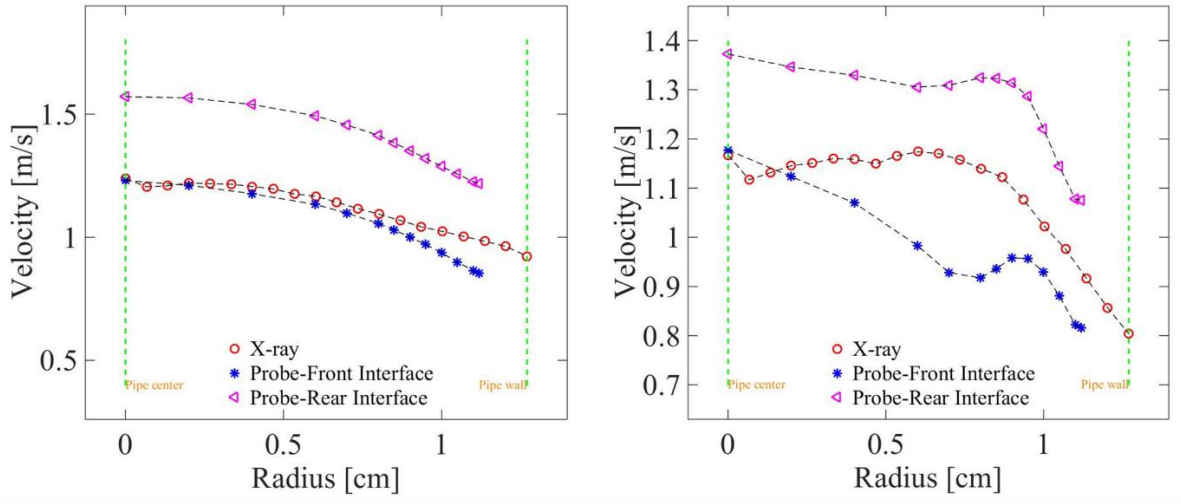

.

Figure 4-11: Radial velocity profile for bubbly flow (a) and slug flow (b) are shown in the graph. Radial distribution with X-ray measurement (red), front-interface probe measurement (blue) and rear interface measurement (purple) are illustrated.

4.4 Area-Averaged Quantities

4.4.1 Flow Meter vs. X-ray

Local superficial gas velocity is calculated for the X-ray measurement location. The superficial gas velocity at the X-ray measurement location is expressed as:

$$j_{g,loc} = \frac{Q_o}{A}\sqrt{\frac{P_{inlet}\cdot T_{\text{standard}}}{T_{inlet}\cdot P_{\text{standard}}}}\cdot\left(\frac{P_{loc}+P_{\text{standard}}}{P_{\text{standard}}}\right) \tag{4.13}$$

where,

$j_{g,loc}$ is the local superficial gas velocity,

Q_o is the volumetric flux

A is the cross-section of the pipe

P_{inlet} is the inlet pressure

$P_{standard}$ is the standard pressure

P_{loc} is the local pressure

T_{inlet} is the inlet temperature

$T_{standard}$ is the standard pressure.

The area-averaged void fraction from the X-ray measurement yields:

$$\langle\alpha\rangle = \frac{\sum\langle\alpha\rangle_{nth\ pixel}A_{nth\ pixel}}{A} \tag{4.14}$$

where,

$\langle a\rangle_{nth\ pixel}$ is the averaged void fraction at nth pixel location,

$A_{nth\ pixel}$ is the area measured by the nth pixel,

A is the cross-section area of the circular pipe.

The area averaged gas velocity from the detector pixel measurement yields:

$$\left\langle\left\langle v_g \right\rangle\right\rangle = \frac{\left\langle j_g \right\rangle}{\left\langle \alpha \right\rangle} = \frac{\frac{1}{A}\sum \left\langle \alpha \right\rangle_{nth\ pixel} \left\langle\left\langle v_g \right\rangle\right\rangle_{nth\ pixel} A_{ith\ pixel}}{\frac{1}{A}\sum \left\langle \alpha \right\rangle_{nth\ pixel} A_{nth\ pixel}} = \frac{\sum \left\langle \alpha \right\rangle_{nth\ pixel} \left\langle\left\langle v_g \right\rangle\right\rangle_{nth\ pixel} A_{nth\ pixel}}{\sum \left\langle \alpha \right\rangle_{nth\ pixel} A_{nth\ pixel}} \quad (4.15)$$

where,

j_g is the superficial gas velocity,

$<<v_g>>_{nth\ pixel}$ is the averaged gas velocity at the nth pixel location.

In this equation, double brackets represent void-weighted area-averaged quantities.

Estimated superficial gas velocity at x-ray location is given by:

$$\left\langle j_g \right\rangle = \left\langle \alpha \right\rangle \cdot \left\langle\left\langle v_g \right\rangle\right\rangle \quad (4.16)$$

The volumetric influx of air flow was measured by two different precision gas flow meter (Cole-Parmer: M Series) with an accuracy of ±1.0% of the full scale reading to cover bubbly and slug flow. Area-averaged quantities from X-ray measurement and flow meter are listed in Table 5. Bubbly and slug flow yield within 13.9% and 7% respectively (averaged of two repeated experiments).

Table 5: Void fraction and gas velocity comparison between flow meter and X-ray measurement.

	Area Averaged Void Fraction	Area Averaged Velocity [m/s]	Superfiial Gas Velocity -X-ray Measured [m/s]	Superfiial Gas Velocity -Flow Meter [m/s]	Difference
	$<\alpha>$	$<<v_g>>$	$<j_g>$	$<j_g>$	**[%]**
Bubble 1	0.1418	1.0697	0.1517	0.1285	15.2694
Bubble 2	0.1306	1.0632	0.1468	0.1286	12.4469
Slug1	0.2504	1.056	0.2644	0.2464	6.8025
Slug2	0.2528	1.0559	0.2669	0.2474	7.33125

4.4.2 X-ray vs. Probe

Area-averaged quantities are calculated from the radial distribution data and listed in Table 6. In Figure 4-7(a) the bubbly flow void fraction distribution, radial profile curves from two measurements show different peak location. However, area-averaged void fraction yielded within 5% difference (averaged over two repeated experiments). For the slug flow, radial void fraction profile shares similar trend but probe measurement tends to estimate less near the pipe wall. For an area-averaged void fraction, the result shows reasonable agreement within acceptable difference within 7.4%.

Front bubble interface profiles are used from the probe for averaged velocity comparison. For averaged velocity, bubbly and slug flow yielded within 3.6% and 15.3% respectively.

Area average void fraction-radial distribution is given by:

$$\langle \alpha \rangle = \frac{\int_0^R \alpha(r) \cdot 2\pi r \, dr}{\pi R^2} \tag{4.17}$$

Area averaged gas velocity-radial distribution is given by:

$$\langle\langle v_g \rangle\rangle = \frac{\int_0^R v(r) \cdot \alpha(r) \cdot r \, dr}{\int_0^R \alpha(r) \cdot r \, dr} \tag{4.18}$$

Table 6: Void fraction and gas velocity comparison between the double-sensor probe and X-ray measurement.

	X-ray	Probe	X-ray [m/s]	Probe [m/s]	Difference [%]	Difference [%]
	<α>	<α>	$<<v_g>>$	$<<v_g>>$	<α>	$<<v_g>>$
Bubble 1	0.1418	0.1474	1.0928	1.0517	3.7992	3.9080
Bubble 2	0.1382	0.1474	1.0859	1.0517	6.2415	3.2519
Slug1	0.2546	0.2359	1.0995	1.3009	7.9271	15.4816
Slug2	0.2521	0.2359	1.1052	1.3009	6.8673	15.0434

4.4.3 Drift-Flux Model

Drift-flux model (Drift Velocity correlation) is provided for an additional reference in Table 7. Drift-flux model is commonly used to describe a two-phase flow in the pipe [2]. Zuber and Findlay proposed the one-dimensional drift-flux model and some of the first drift-flux correlations factors [2]. Later followed by Ishii (2003,2010) [56,57], who developed a comprehensive set of drift-flux models for small pipe and rectangular channels.

Distribution parameter C_o:

$$C_o = 1.2 - 0.2\sqrt{\rho_g / \rho_f} \tag{4.19}$$

where,

ρ_g is the gas density,

ρ_f is the liquid density.

Drift-flux term for a distorted bubble:

$$\overline{V}_{gi} = (C_0 - 1)\langle j \rangle + \sqrt{2}\left(\frac{\sigma g \Delta\rho}{\rho_f^{\,2}}\right)^{1/4}(1-\alpha)^{1.75} \tag{4.20}$$

where,

j is the total volumetric flux.

Drift velocity in bubbly flow:

$$\left\langle\left\langle V_{gi} \right\rangle\right\rangle = \sqrt{2}\left(\frac{\sigma g \Delta\rho}{\rho_f^{\,2}}\right)^{1/4}(1-\alpha)^{1.75} \tag{4.21}$$

Drift-flux term for slug flow:

$$\overline{V}_{gi} = (C_0 - 1)\langle j \rangle + 0.35\left(\frac{g\Delta\rho D}{\rho_f}\right)^{1/2} \tag{4.22}$$

Drift velocity in slug flow:

$$\langle\langle V_{gi} \rangle\rangle = 0.37\left(\frac{g\Delta\rho D}{\rho_f}\right)^{1/2} \tag{4.23}$$

To determine void fraction:

$$\langle \alpha \rangle = \frac{\langle j_g \rangle}{C_o \langle j \rangle + \langle\langle V_{gi} \rangle\rangle} \tag{4.24}$$

Area-averaging allows one to derive the one-dimensional drift-flux equation. Estimated area averaged gas velocity yields:

$$\langle\langle V_g \rangle\rangle = \frac{\langle j_g \rangle}{\langle \alpha \rangle} = C_o \langle j \rangle + \langle\langle V_{gi} \rangle\rangle \tag{4.25}$$

In this equation, the brackets represent area-averaged quantities, and the double brackets represent void-weighted area averaged quantities.

Table 7: Area-averaged void fraction and gas velocity comparison between X-ray and drift-flux model.

	X-ray Measured	Drift Flux Model	X-ray Measured	Drift flux model	difference (%)	difference (%)
	$\langle\langle v_g \rangle\rangle$	$\langle\langle v_g \rangle\rangle$	$\langle\alpha\rangle$	$\langle\alpha\rangle$	$\langle\langle v_g \rangle\rangle$	$\langle\alpha\rangle$
Bubble 1	1.0697	1.1766	0.1418	0.1092	9.0862	29.8166
Bubble 2	1.0632	1.1732	0.1381	0.1096	9.3797	26.0384
Slug1	1.0560	1.1277	0.2504	0.2185	6.3604	14.5872
Slug2	1.0559	1.1313	0.2528	0.2187	6.6634	15.6154

5. CONCLUSION AND FUTURE WORK

5.1 Summary

In the present study, attenuation properties of a non-invasive X-ray beam characteristics was extensively investigated to propose a novel method for obtaining a sequence of line-averaged void fraction data via X-ray attenuation measurements. The results of the X-ray attenuation measurement demonstrated that time, and line-averaged resolved measurements can be effectively used to measure the void fraction and velocity of the two-phase flow. Furthermore, line-averaged void fraction data also revealed local attenuation properties of the two-phase flow structure with high temporal and spatial resolution of the two-phase flow dynamics.

X-ray spectral analysis was performed to measure the void fraction of bubbly and slug flow regimes via a novel quantitative simulation model that attunes the mitigating effects of energy-dependent attenuation coefficient and detector efficiency. The simulation model reveals that significant beam hardening effect of a water medium that is as small as few millimeters thick. Note, in this study, a non-energy-resolving detector was used with unknown energy-dependent efficiency data for the scintillator material. To account for this unknown energy-dependent efficiency of the non-energy-resolving detector system, a calibration experiment was performed to quantify and model detector conversion factor of each detector pixels. The optimized detector conversion factor was approximated to be a second-order polynomial and showed outstanding predictability and accuracy with the calibration experiment. Also, further analysis of void fraction measurements via a polychromatic photon-energy model of X-ray detector system may enhance the spectral analysis of the two-phase flow regime as it presents a profound opportunity to further understand the two-phase flow dynamics.

The SETXvue X-Ray Mass Flowmeter (X-ray Measurement System) was used for void fraction and velocity measurements. In particular, the X-ray signal cross-correlation between upstream and downstream X-ray signals are used to measure the gas velocity and X-ray attenuation

gradient indicated gas velocity that may originate from different phases of the two-phase flow mixture. The superficial gas velocity as measured by Flowmeter was compared with X-ray measurement data and yielded a reasonable agreement within acceptable uncertainty level of 13.9% and 7% for the bubbly and slug flow respectively. Also, radial distribution between void fraction and velocity profile as measured by double-sensor probe was compared to the X-ray data, and yielded satisfactory agreement with a reasonable level of difference: averaged void fraction difference yielded within 5% and 7.4% for bubbly and slug flow respectively, and averaged velocity difference yielded within 3.6% and 15.3% for bubbly and slug flow respectively. Note, the double-senor probe method was a time-consuming process to obtain a void fraction profile as compared to the X-ray technique; the double-sensor approach required two hours whereas X-ray only required 60 seconds per given conditionality criteria. Moreover, the X-ray approach also yielded enhanced spatial resolution as double-sensor probe required more continuous operating time constraints to acquire same spatial resolution distribution. The similar drawback was also encountered when the line averaged void fraction was derived using pixel information as opposed to using the reconstructed algorithm. However, one must be cautious as X-ray measurements and /or signals are extremely sensitive even with few millimeters shift in the X-ray measurement plane as it relates to the reconstruction difficulties. Nevertheless, high temporal and spatial resolution of X-ray measurement approach can deliver an effective and efficient measurement method to investigate various dynamical characteristics of two-phase flow regime.

5.2 Future Work

The X-ray line detector system introduced in this study still remains to be much researched and investigated but not limited to additional tests, experiments, and various adaptations in different settings. One noteworthy distinction would be to evaluate whether the X-ray measurement technique is applicable in non-axisymmetric geometric setting (i.e., rectangular test section) to deliver a robust reconstruction profile. Such as simple distortion from current axisymmetric model assumptions warrants entirely different algorithm development with additional work to be validated with other available measurement techniques.

Additional future work is also warranted for an in-depth analysis of X-ray attenuation measurement techniques that may be benchmarked against various conventional measurement methods. In particular, future work should consider adopting a computed tomographic technique which has become a well-established method of choice in a non-intrusive measurement technique to precise visualize the two-phase flow dynamics. While the current X-ray attenuation measurement provides a solid ground for further research, X-ray CT approach may suggest much more specific open questions and directions.

Lastly, supplementary work must be followed in order to validate the current research results against a conventional local void fraction measurement technique, gas velocity, and local superficial gas velocity profiles to evaluate the applicability of current system for intricate workings of the two-phase flow dynamics. Such supplementary works include but not limited to multi-sensor conductivity tests, high-speed imaging techniques, differential pressure transmitter (DP), and etc.

6. REFERENCE

[1] Zohuri, B., and Fathi, N., 2015, Thermal-Hydraulic Analysis of Nuclear Reactors.

[2] Ishii, M., and Hibiki, T., 2011, Thermo-Fluid Dynamics of Two-Phase Flow (2nd ed.) 2011.

[3] Barthel, F., Bieberle, M., Hoppe, D., Banowski, M., and Hampel, U., 2015, "Velocity measurement for two-phase flows based on ultrafast X-ray tomography," Flow Meas. Instrum., **46**, pp. 196–203.

[4] Manera, A., Ozar, B., Paranjape, S., Ishii, M., and Prasser, H. M., 2009, "Comparison between wire-mesh sensors and conductive needle-probes for measurements of two-phase flow parameters," Nucl. Eng. Des., **239**(9), pp. 1718–1724.

[5] Prasser, H. M., Misawa, M., and Tiseanu, I., 2005, "Comparison between wire-mesh sensor and ultra-fast X-ray tomograph for an air-water flow in a vertical pipe," Flow Meas. Instrum., **16**(2–3), pp. 73–83.

[6] Kendoush, A. A., and Sarkis, Z. A., 1996, "A nonintrusive auto-transformer technique for the measurement of void fraction," Exp. Therm. Fluid Sci., **13**(2), pp. 92–97.

[7] Mäkiharju, S. A., Gabillet, C., Paik, B. G., Chang, N. A., Perlin, M., and Ceccio, S. L., 2013, "Time-resolved two-dimensional X-ray densitometry of a two-phase flow downstream of a ventilated cavity," Exp. Fluids, **54**(7).

[8] Kendoush, A. A., 1992, "A comparative study of the various nuclear radiations used for void fraction measurements," Nucl. Eng. Des., **137**(2), pp. 249–257.

[9] Heindel, T. J., 2011, "A Review of X-Ray Flow Visualization With Applications to Multiphase Flows," J. Fluids Eng., **133**(7), p. 74001.

[10] Ross, S., Haji-Sheikh, M., Huntington, A., Kline, D., Lee, A., Li, Y., Rhee, J., Tarpley, M., Walko, D. A., Westberg, G., Williams, G., Zou, H., and Landahl, E., 2016, "X-ray characterization of a multichannel smart-pixel array detector," J. Synchrotron Radiat., **23**, pp. 196–205.

[11] Hubers, J. L., Striegel, A. C., Heindel, T. J., Gray, J. N., and Jensen, T. C., 2005, "X-ray computed tomography in large bubble columns," Chem. Eng. Sci., **60**(22), pp. 6124–6133.

[12] Stutz, B., and Legoupil, S., 2003, "X-ray measurements within unsteady cavitation," Exp. Fluids, **35**(2), pp. 130–138.

[13] Calton, R. R., and Adler, A. M., 2006, Principles of Radiographic Imaging: An Art and a Science (4th edition).

[14] Uehara, Y., 2016, "L-series X-ray emission spectra of 3d-metal compounds with various excitation conditions," X-Ray Spectrom., **45**(6), pp. 357–362.

[15] Boone, J. M., and Seibert, J. a, 1997, "An accurate method for computer-generating tungsten anode x-ray spectra from 30 to 140 kV," Med Phys, **24**(11), pp. 1661–1670.

[16] Alles, J., and Mudde, R. F., 2007, "Beam hardening: analytical considerations of the effective attenuation coefficient of X-ray tomography.," Med. Phys., **34**(7), pp. 2882–2889.

[17] Deng, J., and Yan, S., 2012, "Beam hardening correction using an attenuation coefficient decomposition approach," IEEE Nucl. Sci. Symp. Conf. Rec., (2), pp. 3602–3604.

[18] Krumrey, M., Gerlach, M., Scholze, F., and Ulm, G., 2006, "Calibration and characterization of semiconductor X-ray detectors with synchrotron radiation," Nucl. Instruments Methods Phys. Res. Sect. A Accel. Spectrometers, Detect. Assoc. Equip., **568**(1), pp. 364–368.

[19] Ludwig, G. W., 1971, "X-Ray Efficiency of Powder Phosphors," J. Electrochem. Soc., **118**(7), p. 1152.

[20] Creagh, D. C., and Hubbell, J. H., 1987, "Problems Associated with the Measurement of X-ray Attenuation Coeccicients. I. Silicon Report on the International Union of Crystallography X-ray Attenuation Project," Acta Crystallogr. Sect. A, **A43**(4), pp. 102–112.

[21] Lempicki, A., Wojtowicz, A. J., and Berman, E., 1993, "Fundamental limits of scintillator performance," Nucl. Inst. Methods Phys. Res. A, **333**(2–3), pp. 304–311.

[22] Robbins, D. J., 1980, "On Predicting the Maximum Efficiency of Phosphor Systems Excited by Ionizing Radiation," J. Electrochem. Soc., **127**(12), p. 2694.

[23] Aichinger, H., Dierker, J., Joite-Barfus, S., and Säbel, M., 2012, Radiation exposure and Image quality in X-ray diagnostic radiology: Physical principles and clinical applications.

[24] Cha, B. K., Jeon, S., and Seo, C. W., 2015, "X-ray performance of a wafer-scale CMOS flat panel imager for applications in medical imaging and nondestructive testing," Nucl. Instruments Methods Phys. Res. Sect. A Accel. Spectrometers, Detect. Assoc. Equip., **831**, pp. 404–409.

[25] Bashore, T., 2001, "Fundamentals of X-ray imaging and radiation safety," Catheter. Cardiovasc. Interv., **54**(1), pp. 126–135.

[26] Hubbell, J. H., "Review of photon interaction cross section data in the medical and biological context," **1**, pp. 0–22.

[27] Bote, D., Llovet, X., and Salvat, F., 2008, "Monte Carlo simulation of characteristic x-ray emission from thick samples bombarded by kiloelectronvolt electrons," J. Phys. D. Appl. Phys., **41**(10), p. 105304.

[28] Poškus, A., 2016, "Evaluation of computational models and cross sections used by MCNP6 for simulation of electron backscattering," Nucl. Instruments Methods Phys. Res. Sect. B Beam Interact. with Mater. Atoms, **368**, pp. 15–27.

[29] Poludniowski, G., Landry, G., DeBlois, F., Evans, P. M., and Verhaegen, F., 2009, "SpekCalc: a program to calculate photon spectra from tungsten anode x-ray tubes.," Phys. Med. Biol., **54**(19), pp. N433–N438.

[30] Poludniowski, and Evans, P. M., 2007, "Calculation of x-ray spectra emerging from an x-ray tube. Part II. X-ray production and filtration in x-ray targets," Med. Phys., **34**(6), pp. 2175–2186.

[31] Poludniowski, G. G., 2007, "Calculation of x-ray spectra emerging from an x-ray tube. Part II. X-ray production and filtration in x-ray targets," Med. Phys., **34**(6), p. 2175.

[32] Oskolok, K. V., and Monogarova, O. V., 2008, "Determination of the emission spectrum of an X-ray tube of a wavelength-dispersive series X-ray fluorescence spectrometer," J. Anal. Chem., **63**(12), pp. 1176–1181.

[33] Wen, Z., Fahrig, R., and Pelc, N. J., 2005, "Robust x-ray tubes for use within magnetic fields of MR scanners," Med. Phys., **32**(7), p. 2327.

[34] Mainegra-Hing, E., and Kawrakow, I., 2006, “Efficient x-ray tube simulations.,” Med. Phys., **33**(8), pp. 2683–2690.

[35] Kirrander, A., Saita, K., and Shalashilin, D. V., 2016, “Ultrafast X-ray Scattering from Molecules,” J. Chem. Theory Comput., **12**(3), pp. 957–967.

[36] Fink, J., Schierle, E., Weschke, E., and Geck, J., 2012, “Resonant Elastic Soft {X}-Ray Scattering,” arXiv:1210.5387 (unpublished).

[37] Donsimoni, M., 1970, US Department of Health, Education, and Welfare. Radiological health handbook. Rev. ed. Washington, DC: US Government Printing Office, 1970.

[38] Saloman, E. B., Hubbell, J. H., and Scofield, J. H., 1988, “X-ray attenuation cross sections for energies 100 eV to 100 keV and elements Z = 1 to Z = 92,” At. Data Nucl. Data Tables, **38**(1), pp. 1–196.

[39] Bearden, J. A., and Burr, A. F., 1967, “Reevaluation of X-ray atomic energy levels,” Rev. Mod. Phys., **39**(1), pp. 125–142.

[40] Hubbell, J. H., and Seltzer, S. M., 1996, “Tables of X-Ray Mass Attenuation Coefficients and Mass Energy-Absorption Coefficients from 1 keV to 20 MeV for Elements Z = 1 to 92 and 48 Additional Substances of Dosimetric Interest Title” [Online]. Available: https://www.nist.gov/pml/x-ray-mass-attenuation-coefficients.

[41] Creagh, D. C., and Hubbell, J. H., 1990, “Problems Associated with the Measurement of X-ray Attenuation Coefficients. II. Carbon. Report on the International Union of Crystallography X-ray Attenuation Project,” Acta Crystallogr. Sect. A, **A46**(5), pp. 402–408.

[42] Petrushanskii, M. G., and Kornev, E. A., 2006, “On Determination of the Effective Energy of a Mixed X Ray Beam,” **40**(2), pp. 102–105.

[43] Ramakrishna, K., Muralidhar, K., and Munshi, P., 2006, “Beam-hardening in simulated X-ray tomography,” NDT E Int., **39**(6), pp. 449–457.

[44] Wong, M. D., Wu, X., and Liu, H., 2011, “The effects of x-ray beam hardening on detective quantum efficiency and radiation dose,” J. Xray. Sci. Technol., **19**(4), pp. 509–519.

[45] Maltz, J. S., Gangadharan, B., Bose, S., Hristov, D. H., Faddegon, B. A., Paidi, A., and Bani-Hashemi, A. R., 2008, “Algorithm for X-ray scatter, beam-hardening, and beam

profile correction in diagnostic (kilovoltage) and treatment (megavoltage) cone beam CT," IEEE Trans. Med. Imaging, **27**(12), pp. 1791–1810.

[46] Aeschlimann, V., Barre, S., and Legoupil, S., 2011, "X-ray attenuation measurements in a cavitating mixing layer for instantaneous two-dimensional void ratio determination," Phys. Fluids, **23**(5).

[47] Coutier-Delgosha, O., Stutz, B., Vabre, A., and Legoupil, S., 2007, "Analysis of cavitating flow structure by experimental and numerical investigations," J. Fluid Mech., **578**, p. 171.

[48] Kishimoto, S., Mitsui, T., Haruki, R., Yoda, Y., Shimazaki, S., Saito, M., Ikeno, M., and Tanaka, M., 2016, "Si-APD linear-array x-ray detector with 10-100 ??m spatial and sub-nanosecond time resolution," AIP Conf. Proc., **1741**.

[49] Gajewski, J. B., 2013, "Accuracy of cross correlation velocity measurements in two-phase gas-solid flows," Flow Meas. Instrum., **30**, pp. 133–137.

[50] Zhang, L., and Wu, X., 2006, "On the application of cross correlation function to subsample discrete time delay estimation," Digit. Signal Process., **16**, pp. 682–694.

[51] Lai, X., and Torp, H., 1999, "Interpolation methods for time-delay estimation using cross-correlation method for blood velocity measurement," IEEE Trans. Ultrason. Ferroelectr. Freq. Control, **46**(2), pp. 277–290.

[52] Munir, M. W., and Khalil, B. A., 2015, "Cross Correlation Velocity Measurement of Multiphase Flow," **4**(2), pp. 802–807.

[53] Kandarakis, I., Cavouras, D., Panayiotakis, G. S., and Nomicos, C. D., 1997, "Evaluating x-ray detectors for radiographic applications: a comparison of ZnSCdSÄg with Gd2O2S:Tb and Y2O2S:Tb screens," Phys. Med. Biol., **42**(7), pp. 1351–1373.

[54] Shepherd, J. A., Gruner, S. M., Tate, M. W., and Tecotzky, M., 1997, "Study of afterglow in x-ray phosphors for use on fast-framing charge-coupled device detectors," Opt. Eng., **36**(11), pp. 3212–3222.

[55] Xue, Z., Charonko, J. J., and Vlachos, P. P., 2014, "Particle image velocimetry correlation signal-to-noise ratio metrics and measurement uncertainty quantification," Meas. Sci. Technol., **25**(11), p. 115301.

[56] Schlegel, J., Hibiki, T., and Ishii, M., 2010, “Development of a comprehensive set of drift-flux constitutive models for pipes of various hydraulic diameters,” Prog. Nucl. Energy, **52**(7), pp. 666–677.

[57] Hibiki, T., and Ishii, M., 2003, “One-dimensional drift-flux model and constitutive equations for relative motion between phases in various two-phase flow regimes,” Int. J. Heat Mass Transf., **46**(25), pp. 4935–4948.